Utilizing Simpler Models to Understand Atmospheric River Responses to Sea-Surface Temperature Increases

By

Elizabeth Elliott McClenny

Dissertation

Submitted in partial satisfaction of the requirements for the degree of

Doctor of Philosophy

in

Atmospheric Science

in the

Office of Graduate Studies

of the

University of California

Davis

Approved:

Dr. Paul A. Ullrich, Chair

Dr. Shu-Hua Chen

Dr. Richard Grotjahn

Committee in Charge

2021

Copyright © 2021 by
Elizabeth Elliott McClenny
All rights reserved.

This dissertation is dedicated to my husband, whose support never wavered.

Contents

List of Figures

List of Tables

Abstract

Utilizing Simpler Models to Understand Atmospheric River Responses to Sea-Surface Temperature Increases

Atmospheric rivers (ARs) are filamentary systems which perform nearly all of the poleward moisture transport through the midlatitudes. When these systems are lifted—for instance when impinging on local topography—they can produce substantial precipitation which ranges from beneficial to destructive, sometimes providing essential water resources and sometimes leading to devastating floods. With this in mind, it is critical for planning and preparedness purposes to project the response of ARs to climate change. Open questions remain however, highlighting the need for a better understanding of the physical processes behind the AR response to climate change. To address these gaps in understanding, ARs are simulated in an aquaplanet, an idealized global climate model without land, sea ice, topography, or seasonality. A time-invariant "Baseline" sea-surface temperature (SST) distribution is prescribed for a reference run, while each test run applies a uniform increase (plus two, four, and six Kelvin) over the Baseline distribution to isolate the response of ARs to warming SSTs and assess sensitivities.

Under SST increases, zonal mean AR occurrence frequency increases everywhere, mostly due to enhancements in AR size. These AR occurrence frequency increases are greatest at higher latitudes as storm tracks shift poleward with SST warming. Zonal and areal means of AR integrated water vapor (IWV) show that AR moisture is enhanced at rates greater than predicted for surface moisture by the Clausius-Clapeyron relation with respect to SST warming. Vertical profiles of relative humidity (RH) and temperature show that this "super-Clausius-Clapeyron" IWV increase masks RH decreases at upper levels which are related to upper-tropospheric warming that far outpaces the prescribed SST increases. Meanwhile, zonal and areal means of AR IWV transport (IVT) show lower increases with SST warming than for IWV; a simple linear decomposition of AR IVT into moisture and wind components shows that a slowing of mean AR wind speeds attenuates the IVT response. Meanwhile, zonal mean AR precipitation rates exhibit a

complicated response characterized by increases in some latitude bands and decreases in others. A linear decomposition of AR precipitation rates like that performed for AR IVT once again shows a compensatory relationship between AR moistening and weakening dynamics, in this case mid-tropospheric vertical velocities.

Increases in AR size as SSTs warm are examined separately. Cross-sections of AR IVT are approximated with Gaussian functions with three fit parameters: AR background IVT, AR IVT exceedance above the background, and the breadth of the AR IVT profile, defined as the distance through which 95% of the IVT exceedance occurs. From both the AR IVT cross-sections and their Gaussian approximations are derived four measures of AR width in total. All widths are enhanced with SST warming, mostly as a result of enhanced background IVT statistics and increased AR IVT profile breadth. IVT profile breadth changes are driven mostly by Clausius-Clapeyron moderated moisture increases, though changes to AR wind profiles also play a role.

Chapter 1

Introduction to Atmospheric Rivers

In 1998, Yong Zhu and Reginald Newell performed the first global study which objectively isolated narrow, transient corridors of enhanced lower-tropospheric vapor fluxes from background "broad fluxes" (Zhu and Newell, 1998, hereafter ZN98). They concluded that three to five of these "atmospheric rivers" (ARs) in each hemisphere performed virtually all of the meridional moisture flux while together occupying a scant ten percent of the zonal circumference through the midlatitudes. It would be several years until the magnitudes of both AR zonal fraction and water vapor transport were confirmed independently in satellite retrievals of water vapor by Ralph et al. (2004a); it would be more than a decade after this that a formal definition for "atmospheric river" first appeared in the American Meteorological Society (AMS) *Glossary of Meteorology* (AMS, 2017), a feat facilitated by substantial international effort and coordination (see Ralph et al., 2018, for a summary of this effort). This definition involved many considerations, including whether or not to relate it specifically to midlatitude dynamics, or whether to incorporate quantitative guidance on thresholds for detecting AR lateral boundaries (Ralph et al., 2018). In the end, a largely qualitative definition was adopted, characterizing an AR as a "long, narrow, and transient corridor of strong horizontal water vapor transport that is typically associated with a low-level jet stream ahead of the cold front of an extratropical cyclone." It further notes that AR moisture can have multiple sources, and that ARs can provide abundant precipitation when forced upward (AMS, 2017). Indeed, just as ARs perform an outsized portion of meridional vapor flux relative to the zonal fraction they

occupy, they likewise can lead to precipitation fractions which appear at odds with their sometimes fine appearance. On a global level, ARs produce more than one-fifth of runoff totals (Paltan et al., 2017), while regional precipitation fractions from ARs can dominate even that figure: as an example, regions along the southern west coast of South America can receive up to 60% of their total annual precipitation from ARs (Viale et al., 2018).

While some information on ARs has been provided here, the following sections will provide further context for the later chapters of this dissertation. Section 1.1 provides a brief summary of ARs with a focus on bulk characteristics. Following this, Section 1.2 describes two models of AR development to contextualize some of the uncertainty surrounding these newly defined systems. We conclude this chapter with an outline of the rest of this dissertation.

1.1 Overview of Atmospheric Rivers

We have already emphasized the relative novelty of AR research, which began in earnest at the turn of the 21st century. While ZN98 coined the term *atmospheric river* in reference to midlatitude filaments of enhanced poleward vapor transport, there exists a pilot study undertaken in Newell et al. (1992, hereafter N92) which dubbed river-like filaments of midlatitude lower-tropospheric water vapor flux as "tropospheric rivers". N92 went on to note that these rivers were thousands of kilometers long but under 1000 kilometers wide and appeared to account for the largest moisture flux between the tropics and southern hemisphere midlatitudes, but did not partition river and non-river fluxes specifically as in ZN98. Nevertheless it was the first paper to recognize ARs as drivers of poleward vapor transport.

One might wonder how three to five of these filaments can accomplish nearly all of the midlatitude meridional vapor transport. Observational work on the structure of ARs provides insight to this disproportionate contribution: Ralph et al. (2017) used dropsondes to investigate the structure of landfalling ARs along the United States West Coast, and found that they were characterized by concentrated water vapor ($\geq$ 2 cm) and high wind speeds ($\geq$ 15 m/s) contained mostly in the bottom three kilometers of the atmosphere

and through a horizontal swath of approximately 850 kilometers (Figure 1.1; Ralph et al., 2017). When the resultant vapor transport is integrated across the width of the AR, we are presented with a compelling statistic: an average AR transports $\sim 5 \times 10^8$ kilograms of water vapor per second, more than double the flow at the mouth of the Amazon River, making ARs the largest "rivers" on Earth (Ralph et al., 2017, 2018). Notably, conclusions drawn from the relatively small observational sample size in (Ralph et al., 2017, $N = 21$ ARs) regarding AR vapor transport and width show good agreement with a later study using reanalysis data which featured a much larger sample size ($N \sim 6000$ ARs).

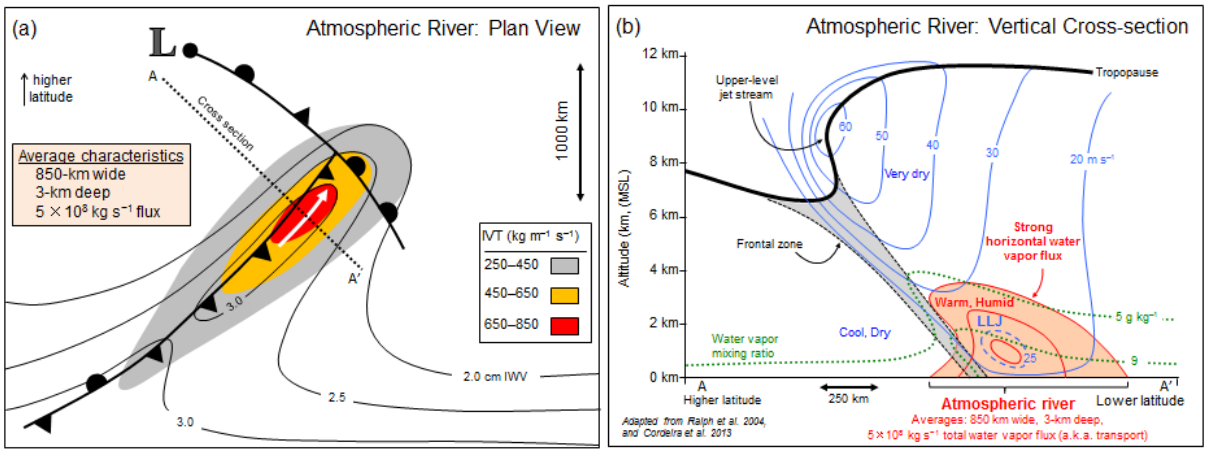

Figure 1.1: (a) Plan view perspective of AR and accompanying surface fronts. Color scale is integrated vapor transport (IVT, kg m^{-1} s^{-1}; Eq. 2.0.2); contours are vertically-integrated water vapor (IWV, shown here in cm; Eq. 2.0.1). (b) Vertical cross-section of AR. Orange color fill is IVT core; blue isotachs (m s^{-1}) are normal to cross-section; green dotted contours are water vapor mixing ratio (g kg^{-1}). Figure is from Ralph et al. (2017), ©American Meteorological Society. Used with permission.

The impacts of landfalling ARs are commensurate with their impressive vapor transport. Worldwide, ARs provide water resources to more than 300 million people (Paltan et al., 2017). This dependence on ARs represents a sensitive balance: for many communities, a wet season with fewer than average ARs means drought, while a season with a higher count of ARs or stronger than average ARs can bring devastating floods (Dettinger et al., 2011). Some of this comes down to ARs' concentrated horizontal vapor transport: it has been found that AR integrated vapor transport [IVT; Equation 2.0.2] is directly related to AR precipitation (Neiman et al., 2002; Moore et al., 2012; Rutz

et al., 2014). Since this precipitation is frequently enhanced by topography, there is a particularly strong relationship between AR upslope moisture transport and precipitation (correlation coefficient = 0.7), such that the angle of AR moisture transport with respect to topography provides an additional control (Neiman et al., 2002). This last point is important, and it reflects the importance of ARs' vertical moisture and thermal structure on their ultimate precipitation. Since ARs contain most of their moisture in the bottom 2.5 kilometers of the atmosphere and are statically moist-neutral through this layer (Ralph et al., 2005, 2017), there is both ample vapor for condensation and little to no resistance to vertical ascent when AR moisture encounters topography. With this in mind, it is clear why direct upslope moisture flux maximize precipitation. In any case, the general relationship between AR IVT and overland impacts has spawned an AR Category system not unlike that developed for hurricanes (Elsner and Kara, 1999) and tornadoes (Fujita, 1981). The AR Category scale uses timeseries of AR IVT at a geographic location to assign a Category ranging from 1 to 5, where a "Category 1" represents a weak, mostly beneficial AR, and a "Category 5" represents a strong, mostly hazardous event (Ralph et al., 2019). The use of an event's IVT timeseries rather than (say) its average or maximum IVT for the scale is an important factor since the length of AR conditions at a point can have a marked effect on ultimate overland impacts (e.g., Ralph et al., 2013).

Along with direct impacts overland, ARs can contribute less directly via their close relationship with extratropical cyclones (ETCs). Specifically, ARs appear to help fuel explosive or bomb cyclogensis, which occurs when the surface pressure in an ETC deepens by at least 24 hPa in 24 hours (Sanders and Gyakum, 1980). A study of ETC climatology in reanalysis output found that approximately 80% of bomb cyclones were associated with a nearby AR within six hours of the ETC's maximum deepening rate (Eiras-Barca et al., 2018). By contrast, ARs were detected nearby in only about 40% of the non-explosive cyclone cases. The authors concluded that LH release when a developing ETC encounters an AR provides an important energy source for further deepening and explosive cyclogenesis. Since bomb cyclones represent particularly destructive midlatitude weather events—like ARs, they can lead to strong winds, intense precipitation, and impressive

storm surges (e.g., Saruwatari et al., 2019)—the interplay here in turn represents an indirect but still significant impact of ARs. With that being said, the relationship between ARs and ETCs is still uncertain; we go over some of these uncertainties in the following section.

1.2 Uncertainties in Atmospheric Rivers

Despite international collaboration to coalesce on a definition of "atmospheric river"—or perhaps because of the grassroots nature of the movement—some uncertainty on ARs persists. Much of this uncertainty can be framed in terms of the relationships between ARs and related phenomena, namely ETCs and tropical moisture exports.

1.2.1 Atmospheric Rivers and Extratropical Cyclones

Much of the uncertainty in ARs is related to the relationship between them and ETCs. ZN98 noted that AR tracks were coincident with midlatitude storm tracks; they framed AR development in terms of ETC dynamics, tying it to an accumulation of warm, moist air along convergence lines on the eastern edges of troughs. As these baroclinic waves destabilize and cyclogenesis initiates, this band of moisture along the convergence lines intensifies and narrows, forming the AR. A later study by Dacre et al. (2015) (hereafter D15) would use findings from a Lagrangian study in reanalysis data to argue that AR development is inextricably tied to moisture convergence along ETC cold fronts such that AR formation is almost entirely dependent on local moisture sources. According to D15, AR formation occurs via the following steps, which are referenced with respect to the ETC's movement in keeping with the ETC-following Lagrangian nature employed in the study:

1. As an ETC propagates across the ocean, evaporation of sea water behind the cold front and moisture flux convergence (MFC) in front of the cold front fuel AR vapor content.

2. As the cold front approaches the warm front, this MFC forms a cohesive, narrow band of enhanced vapor transport at the base of the ETC's warm conveyor belt

(WCB): This band is the AR.

3. As the ETC matures, the movement of the cold front towards the warm front maintains the AR by continuously sweeping up water vapor.

4. As the ETC warm sector narrows, this band of enhanced vapor transport gets cut off from the cyclone center, eventually detaching and propagating on its own even after the "parent" ETC decays.

In short, by the D15 model of AR development, ARs represent "moisture footprints" left behind by ETCs as they move poleward. Importantly, the D15 model is consistent with the frequent co-occurrence of ETCs and ARs and captures the structure of ARs as narrow bands of enhanced poleward moisture flux in front of the cold front. It also allows for the close relationship between ARs and warm conveyor belts (WCBs), which are regions of poleward vapor transport and vertical ascent of heat and moisture on the leading edge of cold fronts (Carlson, 1998). Whereas the poleward transport accomplished by ARs was once ascribed to WCBs (e.g., Carlson, 1998), it has since been clarified that ARs are the thin filaments of low-level (under 850 hPa) poleward vapor transport at the base of WCBs, while WCBs are regions of ascending moisture flux and precipitation (Dettinger et al., 2015). Incidentally this forced ascent and precipitation of AR moisture means the WCB can be thought of as a sink for AR moisture. While the D15 model can appropriately capture this relationship, it does not provide a physical mechanism to accommodate findings from Lagrangian studies which find that ARs can advect vapor from the tropics into the midlatitudes; we discuss this point in the next section.

1.2.2 Atmospheric Rivers and Tropical Moisture Exports

Tropical moisture exports (TMEs) are intrusions of warm and moist tropical air into the extratropics (Knippertz et al., 2010). While we have detailed an argument that AR vapor is fueled entirely by local sources (D15), evidence suggests that ARs can act as TMEs. For instance, a Lagrangian moisture tracker showed that sources of precipitation in Norway (latitude $> 60^\circ$ N) from an AR extended as far as the tropics, which the authors attributed to two hurricanes that underwent extratropical transition (Stohl et al.,

2008). Additionally, a trajectory analysis on Atlantic ARs found significant contributions to AR precipitation along the Iberian Peninsula from vapor originating at latitudes lower than 23.5° N (Ramos et al., 2016). Finally, a model fitted with vapor tracers found that a single AR can persist through multiple ETCs, feeding these ETCs directly with tropical or subtropical (hereafter we say (sub)tropical for brevity) moisture and taking advantage of MFC along their frontal zones in turn (Sodemann et al., 2013), further complicating the relationship between ETCs, TMEs, and ARs. To reconcile and clarify these relationships, we start by describing a second model of AR development which presents a more holistic view of AR vapor sources. The following model of AR development was presented by Jason Cordeira at the International Atmospheric Rivers Conference in 2016 (Cordeira, 2016, hereafter C16) and uses Polar Front Theory (Bjerknes and Solberg, 1922) as the framework:

1. A trough embedded in a Rossby wave propagates over a kink in the Polar Front, equatorward of which exists the (sub)tropical moisture reservoir. Cyclogenesis is initiated and poleward flow within the ETC warm sector advects this (sub)tropical vapor.

2. As vapor ascends in the ETC's WCB, precipitation and the resultant latent heat release aloft deepen the surface and upper-level disturbances, favoring further cyclogenesis and additional poleward vapor transport.

3. Finally, frontogenesis favors low-level MFC, aggregating surface vapor into the filamentary structures known as ARs.

The C16 model can be thought of as a hybrid model which reconciles dynamical links between ETCs and ARs with the concept of ARs as long-distance transporters of water vapor, sometimes from tropical sources. Certainly the very name "atmospheric river" is somewhat misleading because it can be interpreted as ARs being direct conduits between (sub)tropical moisture sources and the midlatitudes, when the relationship is more nuanced than that: while ARs can indeed advect vapor from remote source regions (e.g. Sodemann et al., 2013), they are maintained along their tracks by continuous local

MFC and evaporation (Bao et al., 2006; Payne et al., 2020). Thus the C16 model can describe the case of ARs which also act as TMEs (in other words, TMEs represent a subset of ARs). Meanwhile perhaps the D15 model better describes ARs fueled entirely or mostly by local processes. It is notable that both of these views are consistent with the AMS definition for AR (AMS, 2017), because it intentionally left out dynamical details such as AR genesis (Ralph et al., 2018). For reference, when it comes to this manuscript, we take our guidance on ARs from this definition.

1.3 Scope and Outline of Dissertation

This dissertation takes a novel approach to AR research by leveraging a series of simplified models to answer questions about AR responses to climate change. Since vapor transport by ARs is a key feature of them, and since sea-surface temperatures (SSTs) ultimately drive the availability of water vapor for ARs to entrain, we focus our experiments on SST increases. In order to simplify calculations and ensure proper attribution of AR responses to individual climate forcings, these experiments specifically feature uniform SST increases in an aquaplanet model. An aquaplanet is a global climate model featuring a complete atmosphere component but without land, sea ice, or topography; we additionally run the aquaplanet without ocean-atmosphere feedbacks enabled in order to focus on responses to uniform SST increases alone. In this way, we can ensure that any changes in ARs are properly attributed to an isolated forcing, something which is difficult to do in the context of more complete yet complex climate models (Held, 2005). In all, the results presented here have implications for the past and future of AR climate change studies, since they resolve some issues of attribution normally present in model and observational data.

First, Chapter 2 summarizes the variety of AR detection tools (ARDTs) in the literature, and details the ARDT used for this dissertation to properly contextualize what the ARs studied here represent.

Next, in Chapter 3 we examine the responses of AR moisture transport and precipitation to a series of uniform SST increases (plus two, four, and six Kelvin over a baseline distribution). We separate both AR IVT and precipitation rates into their thermody-

namic and dynamical contributions in a linear decomposition, in keeping with the theme of simpler models used here. While AR IVT responses to climate change have been separated into moisture and wind components before (Gao et al., 2015), this has never before been done in the context of an aquaplanet model, where direct physical effects can be isolated and evaluated. With this series of simpler models—both in terms of the simulation framework itself and in terms of the quantitative analysis—we answer the following questions:

- What are the thermodynamic responses of AR moisture transport and precipitation rates to a collection of uniform SST increases?
- How do dynamic quantities (e.g., midlatitude circulation, wind) respond to increasing SSTs?
- How do these dynamic quantities serve to enhance or damp changes in AR vapor transport and precipitation?

This work is published in *Journal of Geophysical Research: Atmospheres* as:

> **McClenny, E. E.**, Ullrich, P. A., & Grotjahn, R. (2020). "Sensitivity of atmospheric river vapor transport and precipitation to uniform sea surface temperature increases". *Journal of Geophysical Research: Atmospheres*, 125, e2020JD033421. `https://doi.org/10.1029/2020JD033421`

In Chapter 4, we investigate an apparent AR widening seen in the Chapter 3 results. AR widening under climate change conditions has been noted before (Espinoza et al., 2018), but the mechanisms behind it have never been thoroughly investigated. Again along the theme of simpler models, we investigate AR width by modeling AR IVT cross sections as Gaussian functions with three free parameters: local background IVT, AR peak IVT above the background, and overall IVT profile breadth; from this we derive two widths, including an impacts-relevant width which is conditioned on the critical threshold of IVT often employed for detecting AR boundaries ($IVT \geq 250$ kg m^{-1} s^{-1}). We compare this impacts-relevant Gaussian width against AR boundaries determined with

the same critical threshold but with respect to the AR IVT profiles themselves (i.e., not the Gaussian fits), as well as the AR width detected automatically by our ARDT. In all, we use this experimental framework to answer the following questions:

- Are AR IVT cross-sections well-represented as simplified Gaussian functions?
- How do AR local background IVT and peak IVT intensity change as a result of uniform SST increases?
- How do different measures of AR width change under uniform SST increases?
- Finally, how much of the change in the impacts-relevant AR width can be attributed to changes in AR background IVT, AR IVT intensity above the local background IVT, and the overall broadening of AR IVT profiles?

This work is under review in *Journal of Geophysical Research: Atmospheres* as:

> **McClenny, E. E.** & Ullrich, P. A., (2020). "Response of Atmospheric River Width and Intensity to Sea-Surface Temperatures in an Aquaplanet Model". *Journal of Geophysical Research: Atmospheres*

Last, Chapter 5 includes a summary of the conclusions from this work as well as recommendations for future research.

Chapter 2

Detecting Atmospheric Rivers

The first descriptions of ARs discuss these features largely in terms of vapor flux (Newell et al., 1992; Zhu and Newell, 1998), and further studies continue to underscore the role that ARs play in global moisture transport (e.g., Guan et al., 2018; Ralph et al., 2017). As such, we define two relevant quantities here: integrated water vapor (IWV) and integrated vapor transport (IVT).

$$IWV = -\frac{1}{\rho g}\int_{p_B}^{p_T} q dp \qquad (2.0.1) \qquad\qquad IVT = -\frac{1}{g}\int_{p_B}^{p_T} q \cdot \overrightarrow{u} dp \qquad (2.0.2)$$

where p_B is the bottom pressure layer of integration (usually 1000 hPa), p_T is the top pressure layer of integration (anywhere from 100 hPa to 500 hPa is used here; e.g., Rutz et al., 2014; Warner et al., 2014, respectively), ρ is the density of water, g is the gravitational constant, q is water vapor mixing ratio, and $\overrightarrow{u}$ is horizontal wind velocity.

Using the above quantities provides useful metrics for describing AR intensity. AR horizontal vapor transport or its fraction with respect to total global fluxes is generally described in terms of IVT; meanwhile, IWV quantifies AR vapor mass through a grid-box column. IVT and IWV thresholds are also frequently used to identify ARs against background fields, with common thresholds of IVT $\geq$ 250 kg m^{-1} s^{-1} (e.g., Rutz et al., 2013) and IWV $\geq$ 20 kg m^2 (e.g., Ralph et al., 2004b; Wick et al., 2013a); that said, substantial variations in AR detection tools (ARDTs) exist. The following section gives an

overview of some of these variations, as well as the impact those variations can have on final conclusions about ARs. Next, we describe the ARDT used for the studies presented in this manuscript, including results from a collection of detection parameter tuning experiments.

2.1 Overview of Atmospheric River Detection Techniques

ARs are narrow bands featuring high IWV and IVT which are prominent against the much weaker background fields (Figure 2.1 shows an AR against an IVT field for reference). As a consequence of the strong IWV/IVT which characterizes ARs, it is generally trivial to identify their lateral boundaries by visual inspection of these fields alone; for instance N92 inspected maps of IWV to perform their pilot study. While this might suffice for examining a handful of ARs, manual detection is tedious and prohibitively slow when one wishes to study ARs over multiple seasons to decades. As a consequence, researchers have independently developed automated ARDTs which can identify AR spatiotemporal boundaries. However, the uncertainty associated with ARs carries over to the automated methods used to detect them. One source of uncertainty lies in the very field used for identifying ARs; that is, some ARDTs rely on IWV while others rely on IVT. IWV-based ARDTs are exceptionally useful for observational studies, since satellite imagery of water vapor channels is readily available (e.g., Ralph et al., 2004a). Since IWV thresholds alone do not capture the moisture transport associated with ARs, these methods often rely additionally on low-level wind speed thresholds when wind data are available (e.g., Hagos et al., 2015; Shields and Kiehl, 2016). Furthermore, the temperature dependence of saturated vapor pressure induces a strong background meridional IWV gradient which can make it difficult to distinguish ARs at subtropical latitudes, where background IWV can near or exceed the common AR threshold of 20 kg mm^2 (for reference, Figure 3.6 shows zonal mean IWV results for an aquaplanet study used in this dissertation).

To address some of these issues, IVT thresholds are frequently used to detect ARs in model output data. IVT has the advantage of capturing ARs as systems of enhanced vapor transport, and leads to more consistent AR statistics across latitudes: lower-latitude

ARs tend to feature higher IWV, while ARs at higher latitudes tend to feature stronger wind speeds but less moisture (Ralph et al., 2017). Since IVT takes both moisture and wind into consideration, there exists much lower variability associated with background fields—in other words, AR IVT statistics do not vary as a result of latitude like AR IWV statistics do. Still, IVT-based ARDTs introduce their own variability, mostly in terms of the thresholds employed. While many rely on the absolute threshold already mentioned (IVT $\geq$ 250 kg m^{-1} s^{-1}; Rutz et al., 2013; Gershunov et al., 2017), others employ a relative threshold (usually 85th percentile of IVT, e.g., Guan and Waliser, 2015; Ramos et al., 2016; Viale et al., 2018) with the physical basis being that ARs are features not just of high IVT, but of exceptional IVT with respect to climatological background values. Incidentally, it is due to this last point that some ARDTs employ no threshold at all, but instead use image processing and/or machine learning based methods to identify transient plumes of enhanced IVT against the comparatively weak background (Muszynski et al., 2019; Xu et al., 2020).

Beyond IVT (or IWV) threshold considerations, ARDTs also vary in other ways, with some enforcing overall object size requirements (e.g., Rutz et al., 2014; McClenny et al., 2020) and/or object length-to-width ratios (usually two-to-one; e.g., Goldenson et al., 2018; Viale et al., 2018), and some requiring tuning for specific regions (e.g., Payne and Magnusdottir, 2015; Shields and Kiehl, 2016) while others feature global coverage (e.g., Guan and Waliser, 2015; Mundhenk et al., 2016). With such a variety of ARDTs, it is challenging to compare results from one study to another. In an effort to quantify the uncertainty associated with ARDTs, the Atmospheric River Tracking Method Intercomparison Project (ARTMIP; Shields et al., 2018) was initiated in a grassroots fashion, much like the effort to define ARs. ARTMIP has revealed substantial disparities across ARDTs: for instance, Shields et al. (2018) noted marked variations across ARDTs in distributions of AR frequency and duration along coastal transects for a one-month period. The paper found that most disagreement occurred for weaker events, while ARDTs more consistently identified stronger ARs. A followup study by Rutz et al. (2019) also found a wide range of results across ARDTs, though some of this was resolved when ARDTs were

clustered into groups featuring similar criteria. In the end it was shown that ARDTs with less restrictive criteria have the advantage of finding more ARs and AR-related impacts, while more restrictive ARDTs tend to detect the strongest or most extreme ARs (Rutz et al., 2019). Clearly, discretion is necessary when evaluating AR statistics derived from ARDTs; to address some of this, the following section describes the ARDT employed in this dissertation, as well as some of the work undertaken while including this ARDT in the ARTMIP effort.

2.2 Detecting Atmospheric Rivers with Tempest

All AR statistics shown in this thesis are derived from an original ARDT available under the TempestExtremes feature detection software suite (Ullrich and Zarzycki, 2017; Zarzycki and Ullrich, 2017; Ullrich et al., 2021, *in preprint*). Since AR statistics are a product of the ARDT used to identify AR lateral boundaries, an understanding of the ARDT employed is necessary to understand the resulting statistics. Whereas most ARDTs identify ARs with explicit relative or absolute IVT thresholds, TempestExtremes (TE) instead computes an eight-point stencil Laplacian (at each of the cardinal and intercardinal directions) of IVT (L^2IVT) at each grid point and accepts a threshold value for L^2IVT. By the second derivative test, $L^2\text{IVT} < 0$ represents a concave down position; more qualitatively, any grid point featuring $L^2\text{IVT} < 0$ corresponds to a ridge in the IVT field. Since ARs are features of enhanced IVT (i.e., ridges in the IVT field), we propose that a negative threshold for L^2IVT can therefore be used to identify ARs. That said, the use of this metric benefits from manual tuning in order to reliably capture ARs; we go over some of these tuning efforts for the remainder of this chapter.

2.2.1 Tuning Tempest for Atmospheric Rivers

TE's use of L^2IVT is challenging because it requires both a magnitude and a radius (i.e., a distance in each of the eight directions) over which to compute L^2IVT. The magnitude is somewhat difficult to determine because there is no known climatology of L^2IVT for ARs, as opposed to the more common ARDT absolute or relative IVT thresholds, which are justified by substantial background research. Furthermore, any attempts to establish

L^2IVT statistics for ARs would necessarily be sensitive to the stencil radius employed in the calculations. Last, the underlying grid size of the data impacts L^2IVT statistics (a point we expand on in the next section). For now, we will focus on the Laplacian stencil radius parameter (hereafter, we say "radius" for brevity), which impacts L^2IVT computations by acting as a smoothing parameter over the L^2IVT field. The radius has to be tuned such that TE simultaneously accomplishes two goals: (1) ridges in the IVT field are sufficiently smoothed to remove features which are too weak to be considered ARs, and (2) ridges in the IVT field which do represent ARs are not overly smoothed out, and therefore no longer detected by TE.

To illustrate the effect of radius on the final AR lateral boundaries, Figure 2.1 shows a snapshot of an AR impacting the United States (US) West Coast on an IVT field. The figure also shows the effect of a series of different area requirements, where area corresponds to the minimum number of connected grid points which meet the L^2IVT criterion—we show this as a comparison for the radius. The figure shows us that as radius increases, smaller objects tend to get smoothed out and no longer recognized as ARs by TE; this latter effect occurs as the area requirement increases as well. A notable difference between the radius and area increases is that the radius increases result in an AR with a smoother boundary, while area increases simply remove smaller standalone objects. The smoothing and ultimate removal with increasing radius happens because using more distance in the L^2IVT computation can smear out ARs, or parts of them, from the L^2IVT field. As a result, some of this smoothing can be mitigated by applying a less negative L^2IVT threshold. In any case, the smoothing with enlarged radius introduces us to an important trade-off: while a larger radius might successfully remove small, non-AR objects, it can do so at the expense of identifying an AR's full extent, which is of particular importance when one wishes to attribute impacts to ARs.

Now that we have shown some radius and area considerations for TE, we move on to briefly discuss the effects of changing the L^2IVT parameter. Figure 2.2 is the same as Figure 2.1, but for $L^2\text{IVT} < -40000$ kg m^{-1} s^{-1} rad^{-2} (hereafter we omit units for readability). Comparing the two figures yields some interesting observations: first, it is

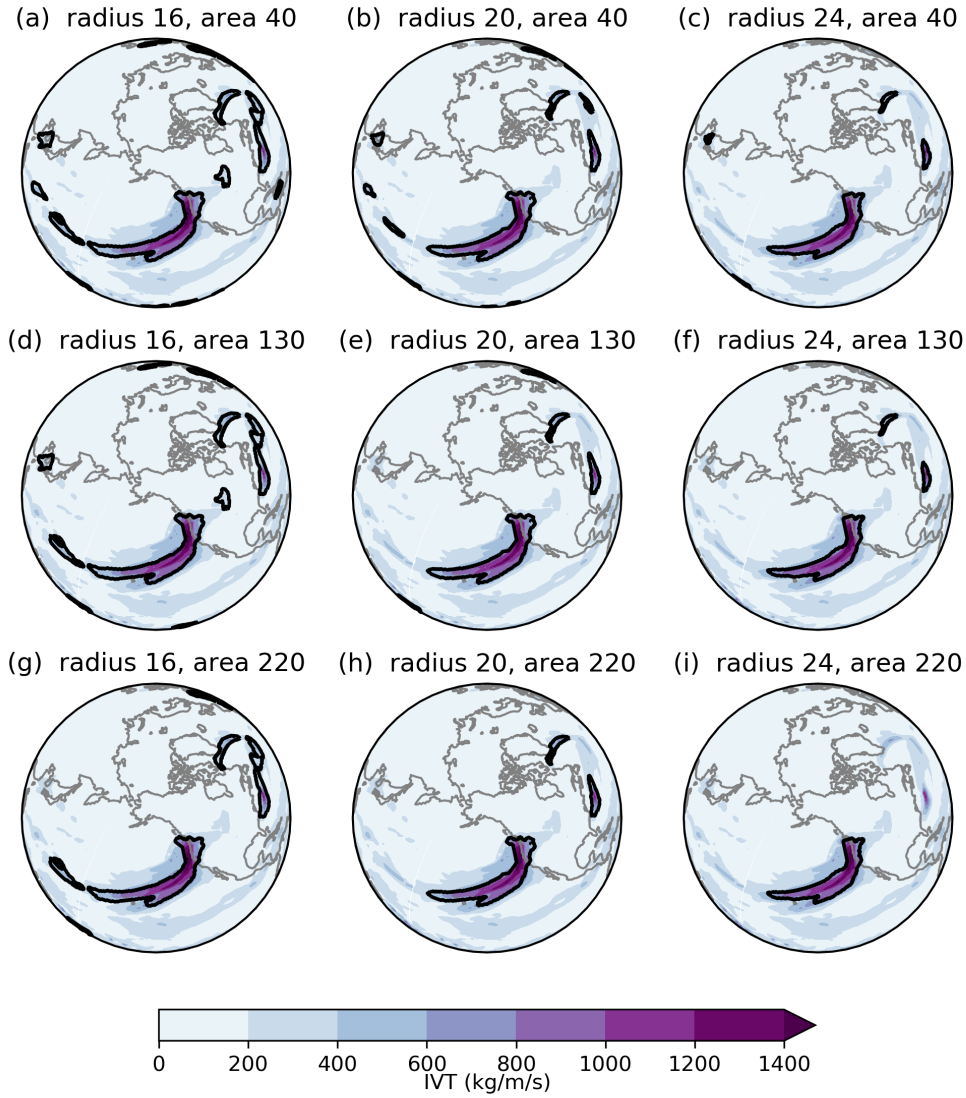

Figure 2.1: Snapshot of example objects detected by TE for $L^2\text{IVT} < -20000$ kg m^{-1} s^{-1} rad^{-2} and labeled radius/area requirements (grid points). Colored contours show IVT while black outlines show AR boundaries as determined by TE. IVT data were derived from the Modern Era Retrospective Analysis for Research and Applications, Version 2 (MERRA2; Gelaro et al., 2017), which has a $0.625° \times 0.5°$ longitude-latitude grid.

consistent with our earlier assertion that a less negative Laplacian threshold can offset some of the AR boundary contraction which occurs with a larger radius, a finding which is especially apparent when comparing the right-hand columns of Figures 2.2 and 2.1.

Second, it shows us that enforcing a stricter (more negative) L^2IVT consistently results in identifying the same strong AR impacting the US West Coast, but with the caveat that it instead identifies a narrower region about the AR's high-IVT "core". This contraction of the AR lateral boundaries makes it more difficult to attribute overland impacts to the AR (similar to the smoothing of the objects which occurs as the radius increases), but it has the advantage of picking out AR cores which may be of interest to researchers. The physical reasoning for this contraction is that a more negative L^2IVT requirement will naturally correspond to regions of IVT featuring greater curvature than a less negative one; this region of enhanced curvature corresponds to the AR core.

Individual-AR differences realized by tuning parameter variations carry over into overall AR climatologies. Figures 2.3 and 2.4 show the all-season AR occurrence frequency (OF) for 20 years (1980-1999) of Modern Era Retrospective Analysis for Research and Applications, Version 2 (MERRA2; Gelaro et al., 2017) output for the same set of tuning experiments as Figures 2.1 and 2.2. In a qualitative sense, the maps are consistent both with each other and with another AR global OF climatology found using a different ARDT in Espinoza et al. (2018); specifically, we tend to see local AR OF maxima along the western sides of ocean basins which steadily shift poleward towards the east, in keeping with the typical propagation of ARs.

Despite some qualitative consistency, we find that clear differences exist, each in keeping with expectations set up by the earlier TE snapshots (Figures 2.1 and 2.2). Just as we showed that an increase in the radius for a given area or L^2IVT threshold resulted in capturing fewer grid points as belonging to an AR, we also see a systematic decrease in overall AR OF as radius increases. This could come down to capturing fewer objects overall, capturing fewer grid points per object, or some mix of the two, any of which can occur as the enlarging radius smooths the L^2IVT field. Notably, this effect works in tandem with increasing area to minimize the number of smaller tropical objects (e.g., tropical cyclones, easterly waves) which are captured by TE as ARs (Figure 2.3; note the swaths of shading between approximately 15°N and 20°N), revealing the utility of using a larger radius to smooth out these smaller objects from the L^2IVT field. Meanwhile, com-

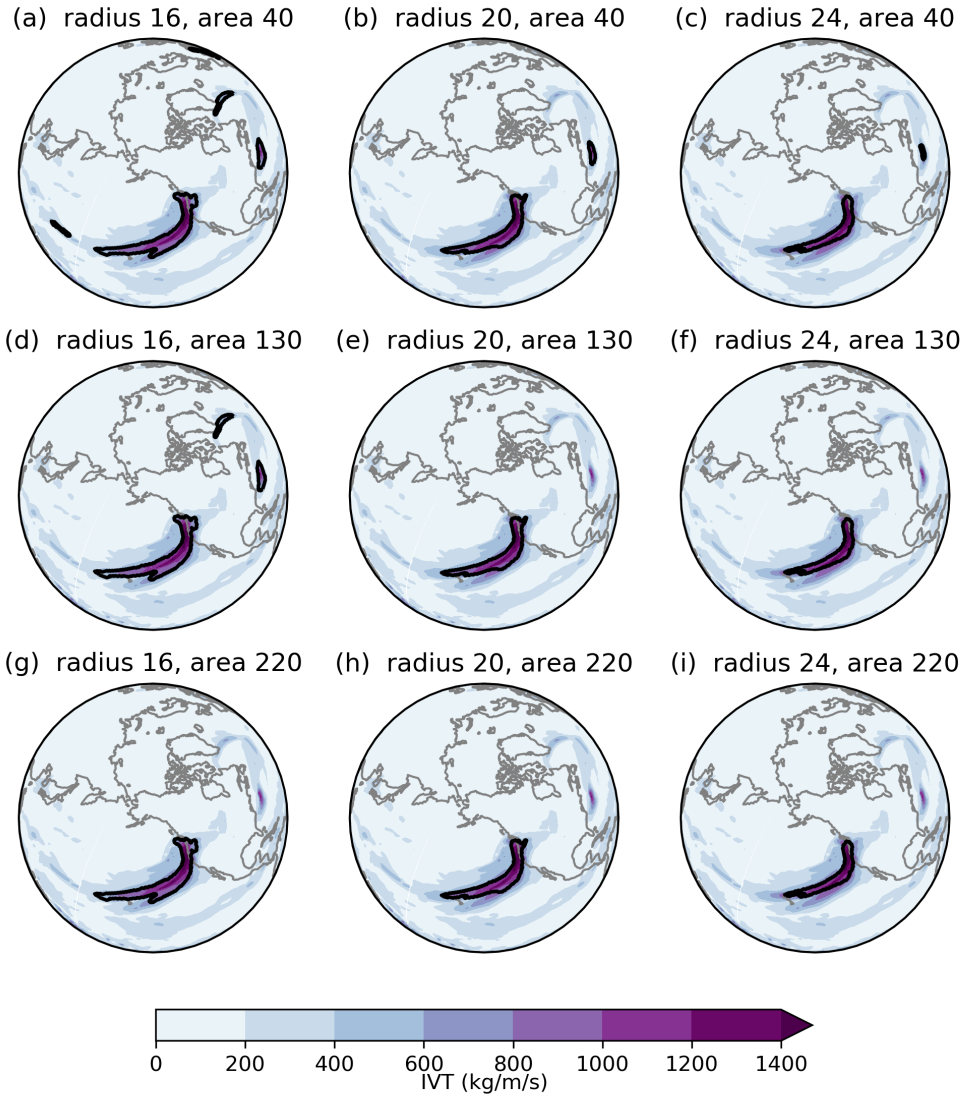

Figure 2.2: As Figure 2.1, but for L^2IVT< -40000 kg m^{-1} s^{-1} rad^{-2}.

paring Figures 2.3 and 2.4 against one another shows how L^2IVT magnitude impacts AR OF statistics. Consistent with findings from Figures 2.1 and 2.2, AR OF systematically decreases as the critical threshold of L^2IVT is lowered from -20000 to -40000. Since Figures 2.1 and 2.2 show that -40000 represents a stricter threshold which tends to pick out only the strongest objects, it follows that the OF would essentially be a sub-sample of that for the -20000 case. Notably, the OF shown in 2.4g appears the most quantitatively

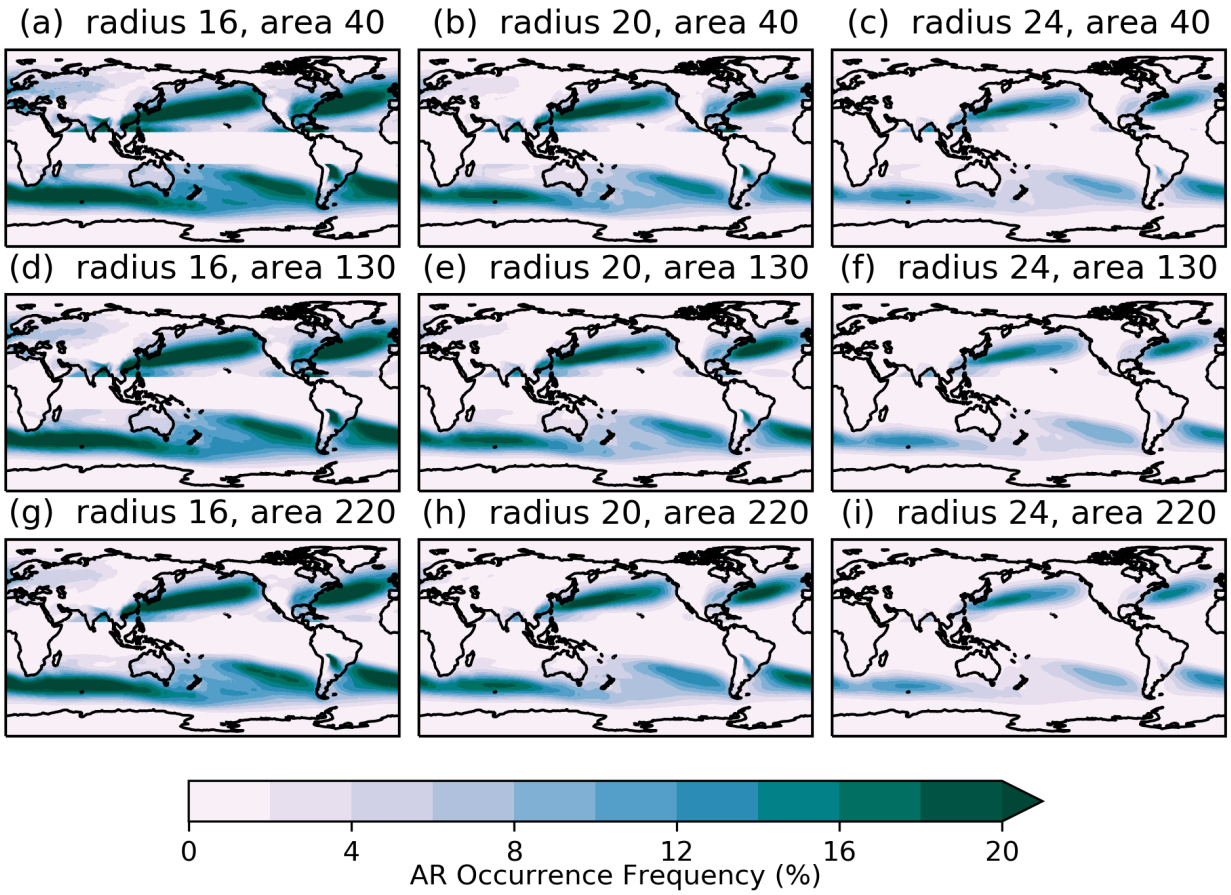

Figure 2.3: MERRA2 all-season AR occurrence frequency (%) from 1980-1999, shown here across multiple radius and area criteria for $L^2\text{IVT} < -20000$ kg m^{-1} s^{-1} rad^{-2}. The harsh delineation present at $\pm 15°$N is due to latitude masking to remove the bulk of tropical features captured by TE.

similar to the AR OF for a different reanalysis product in Espinoza et al. (2018), suggesting that the corresponding tuning was the most consistent with their ARDT criteria, though the different models used makes this difficult to assess.

2.2.2 Tuning Tempest for Different Grid Sizes

We already mentioned that the underlying grid size of our data impacts L^2IVT statistics. This was made apparent when using TE to detect ARs in a collection of models which participated in the Climate Model Intercomparison Project 5 (CMIP5; Taylor et al., 2012).

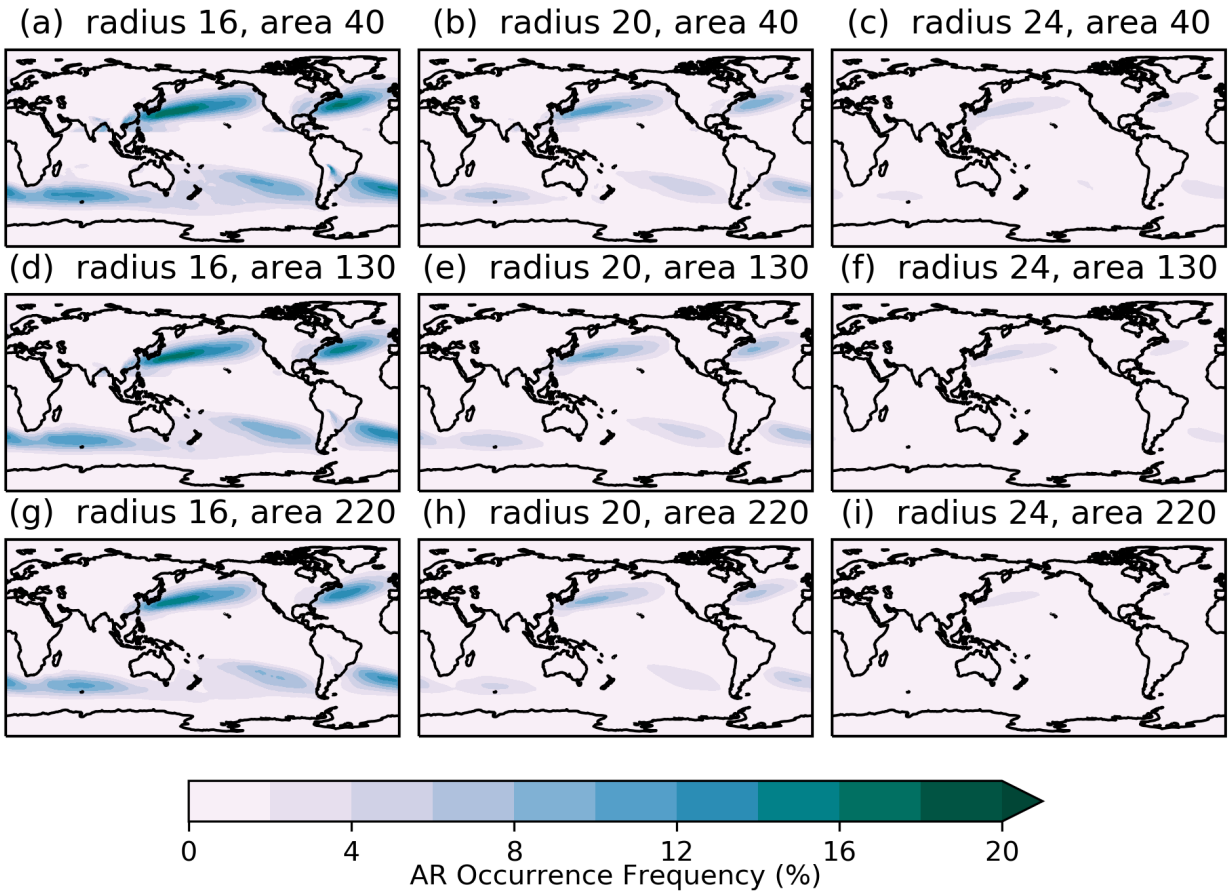

Figure 2.4: MERRA2 winter (DJF) AR occurrence frequency (%) from 1980-1999, shown here across multiple radius and area criteria for $L^2\text{IVT} < -40000$ kg m^{-1} s^{-1} rad^{-2}.

Since this analysis of TE ARs was a part of the ARTMIP effort, it was essential to have consistent tuning between each model in order to minimize intra-ARDT criteria differences as a source of uncertainty. As such, we changed the radius and area requirements to accommodate the disparate grid sizes (Table 2.1) in order to maintain as much consistency as possible in terms of geographic distances. Yet despite what we considered sufficient compensatory criteria changes, we found the unexpected result that TE tended to detect ARs sometimes much more rarely in the CMIP5 models than in MERRA2, which we used as our reference model (Figure 2.5).

To investigate this discrepancy, we assume that in its exact form, the AR IVT cross-

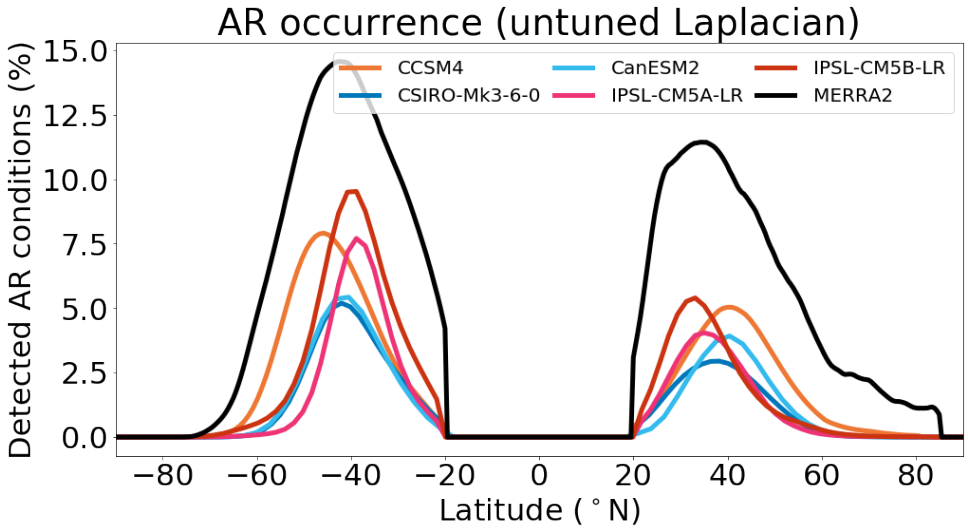

Figure 2.5: Zonal-mean all-season AR occurrence frequency (%) when using the same critical threshold (L^2IVT< -30000 kg m^{-1} s^{-1} rad^{-2}) across models, compensating only for area and radius as shown in Table 2.1. CMIP5 data are from 1950-2005; MERRA2 data are from 1980-2005.

section takes the form

$$IVT(s) = IVT0 + dIVT \exp\left(-\frac{8s^2}{wd^2}\right) \tag{2.2.1}$$

where $IVT(s)$ is the pointwise IVT at distance s kilometers along the cross section, $IVT0$ is the constant background IVT, $dIVT$ is the anomalous IVT enhancement from the AR, and wd is the dynamic width of the AR (as defined in Chapter 4).

If a typical finite volume method is employed for modeling the atmosphere (a common approach in global climate model dynamical cores), the discrete degrees of freedom stored in the model correspond to volume averages rather than pointwise samples. In practice, such a numerical method is generally only able to "resolve" features whose width exceeds $3\Delta x$ (or wavelength $6\Delta x$) (Ullrich, 2014). For simplicity we will assume here that the atmospheric river object is simulated perfectly, but is nonetheless subject to smoothing because of its representation on the discrete grid. Discretization of the AR profile (A.1.1) on a grid cell of width Δs centered on a point s then corresponds to the operation

$$\frac{1}{\Delta s}\int_{s-\Delta s/2}^{s+\Delta s/2} IVT(s')ds'. \tag{2.2.2}$$

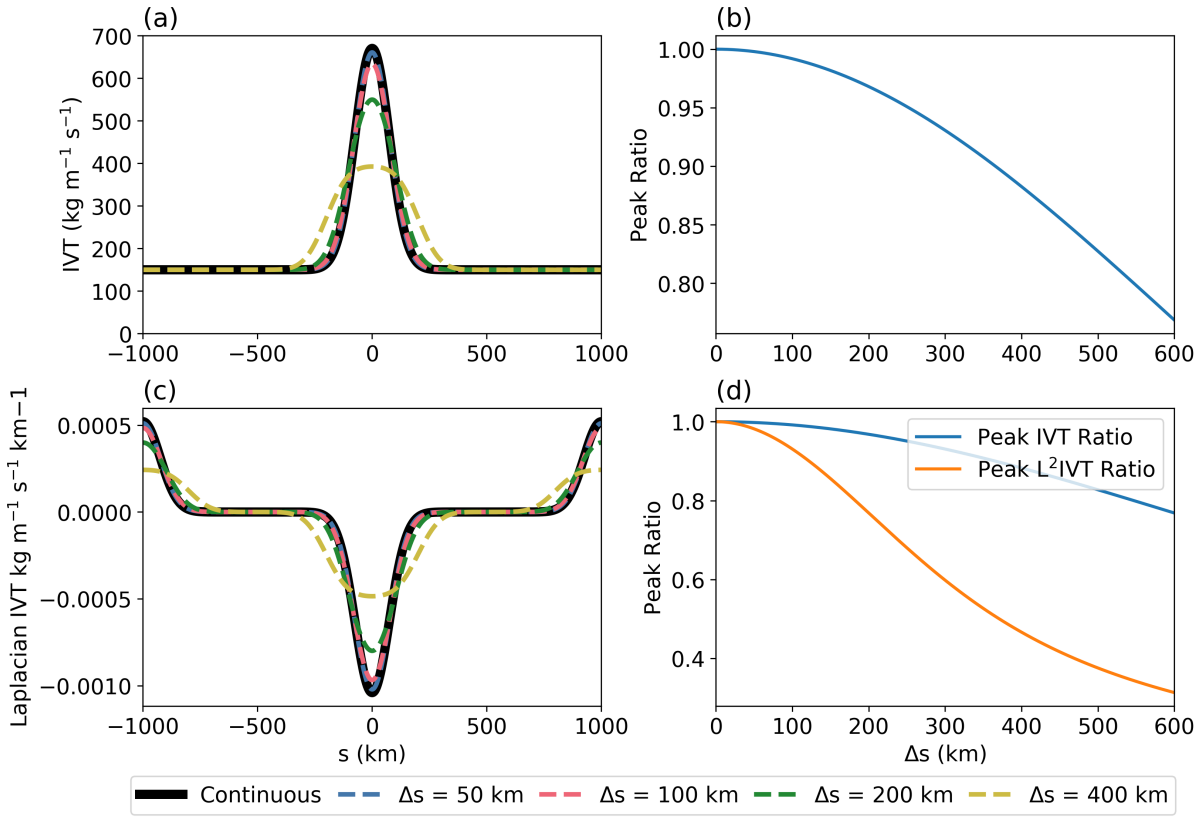

Figure 2.6: Theory based scaling for AR IVT and L^2IVT. (a) Continuous and discrete (smoothed) IVT profiles for given grid spacings. (b) Peak IVT ratio as a function of grid spacing. (c) L^2IVT for corresponding IVT profiles in (a). (d) Peak IVT and L^2IVT ratios as a function of grid spacing. See text for details.

Treating this as a moving filter produces the smoothed profile

$$\overline{IVT}(s) = IVT0 + \frac{dIVTw\sqrt{2\pi}}{8\Delta s}\left[\text{erf}\left(\frac{\sqrt{2}(2s+\Delta s)}{wd}\right) - \text{erf}\left(\frac{\sqrt{2}(2s-\Delta s)}{wd}\right)\right]. \quad (2.2.3)$$

The original profile and its discrete (smoothed) analogue for $\Delta s = \{50 \text{ km}, 100 \text{ km}, 200 \text{ km}, 400 \text{ km}\}$ is plotted in Figure 2.6a for a dynamical width of $wd = 300$ km (smaller than the average ∼900 km AR width; we do this in order to capture narrower storms), a typical AR intensity of $dIVT = 520$ kg m^{-1} s^{-1}, and a background IVT of $IVT0 = 150$ kg m^{-1} s^{-1} (based on results from Chapter 4). For comparison, atmospheric models participating in CMIP5 generally use grid spacing of 110 km or greater, with some reaching resolutions of 250 km or more (Table 2.1).

The ratio of the peak IVT in the discrete profile (over $IVT0$) to its exact analogue

can be written as

$$\frac{IVT(0)}{\overline{IVT}(0)} = \frac{\sqrt{2\pi}}{4\Delta s}\text{erf}\left(\frac{\sqrt{2}\Delta s}{wd}\right), \tag{2.2.4}$$

which is plotted in Figure 2.6b. As we can see, the intensity of the average AR can drop off fairly rapidly on coarser grids, a typical effect when such features are underrepresented. Thus, to capture the same ARs on a coarser grid, the threshold for maximum dIVT over the background IVT0 should scale in accordance with Equation 2.2.4—e.g., if an IVT threshold of 250 kg m^{-1} s^{-1} is employed for detecting atmospheric rivers at fine resolutions, then an IVT threshold of 225 kg m^{-1} s^{-1} should be used at a 400 km grid spacing.

However, the analysis above only applies for ARDTs that use the IVT criteria, whereas TE uses the discrete Laplacian with radius Δr of the IVT for detection of ARs, here defined as

$$L^2IVT(s) = \frac{\overline{IVT}(s-\Delta r) - 2\overline{IVT}(s) + \overline{IVT}(s+\Delta r)}{\Delta r^2}, \tag{2.2.5}$$

which is again plotted in Figure 2.6c with the parameters given above, with a typical Laplacian stencil radius of $\Delta r = 1000$ km. Here the ratio of peak L^2IVT in the discrete profile is plotted in Figure 2.6d. This suggests a reduction in the peak L^2IVT threshold employed in TE that is substantially more than that for IVT, reaching around 60% of its reference value when the grid spacing is around 300 km.

In summary, this analysis tells us that TE should require a less negative L^2IVT as grid size increases in order to achieve better consistency in AR statistics across model grids. Mathematically, this L^2IVT scaling formula takes the form:

$$L^2IVT(s) = L^2IVT_{ref}\left(\frac{\exp\left(\frac{-s^2}{4w^2}\right)}{\exp\left(\frac{-s_{ref}^2}{4w^2}\right)}\right) \tag{2.2.6}$$

where $L^2\text{IVT}_{ref}$ is the L^2IVT requirement used for the reference model, s_{ref} is the grid spacing of the reference model (we use latitude spacing in degrees), w is a constant distance (we use an empirically derived value of $w = 2°$), and s is the grid spacing of the model to which we are scaling.

Table 2.1 shows the TE tuning criteria as scaled via Equation 2.2.2, using MERRA2 tuning parameters as reference values for each model, while Figure 2.7 shows the resulting zonal mean AR OF across models. In all, we see more consistency in AR OF across models in terms of overall magnitudes, though discrepancies in the location of maximum AR OF still exist. Regardless, it is reassuring that the additional tuning overall improved the intermodel spread in AR OF. In keeping with expectations that coarser grids result in smoother IVT fields, we find that the model featuring the largest latitude spacing (canESM2) experiences the most improvement with respect to MERRA2 after applying the L^2IVT scaling (Figure 2.7). Still, TE systematically produces lower AR OF in all CMIP5 models relative to MERRA2, suggesting that these results can be improved with additional tuning. Certainly, additional L^2IVT values can be computed for the models, as the scaling obtained from Equation 2.2.2 is sensitive to the width of the storms being captured. In any case, these results show the sensitivity of TE to the L^2IVT parameter across different models.

Model	L^2IVT	Grid spacing	Radius	Area
MERRA2	-30000	0.625×0.5	20 (1110)	220 (847, 069)
CCSM4	-28827	1.125×0.9424	10 (1046)	65 (849, 077)
CSIRO	-24516	1.875×1.8653	6 (1035)	20 (861, 838)
CanESM2	-18729	2.8125×2.7906	4 (1239)	9 (870, 319)
IPSL-CM5A	-24348	3.75×1.8947	5 (1051)	10 (875, 422)
IPSL-CM5B	-24348	3.75×1.8947	5 (1051)	10 (875, 422)

Table 2.1: Criteria used for TE CMIP5 experiments (the criteria used to generate Figure 2.7. L^2IVT is given in kg m^{-1} s^{-1} rad^{-2}, grid spacing is given in longitude $\times$ latitude coordinates, radius is given in grid points (approximate km with respect to latitude spacing), and area is given in grid points (approximate km^2). Note that Figure 2.5 was derived using the same criteria as listed here, but with $L^2\text{IVT} < -30000$ remaining constant for all models.

After describing the effort required to tune Tempest's L^2IVT parameter for AR detection to individual models, one might wonder what this effort yields. To answer this, we must describe what L^2IVT and the radius physically represent: while negative L^2IVT

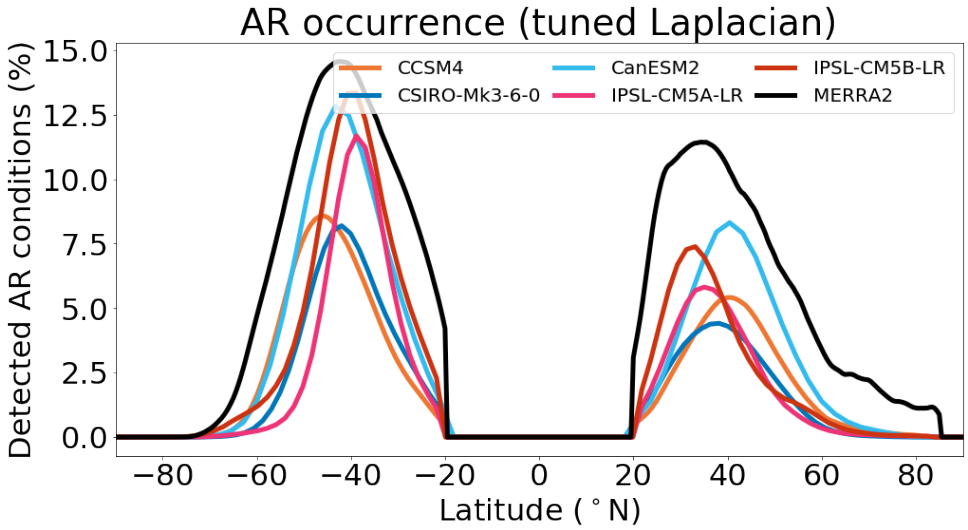

Figure 2.7: Same as Figure 2.5, but for results after tuning the L^2IVT for each model's latitude-longitude grid size.

corresponds to a ridge in the IVT field, the radius represents the (relatively short) distance over which this ridge occurs. This is to say that the radius is equivalent to how much of the local background about a grid point is included in the calculation of L^2IVT. In other words, the radius allows us to account for the local climatology about a grid point; from a physical standpoint this suggests that the radius should at least be equal to the typical AR width ($\sim$ 900 km; Ralph et al., 2017). Thus, our finding that an approximate radius of 1000 kilometers suffices is physically consistent with the width scale of ARs. Overall, the benefit of using a L^2IVT threshold rather than an IVT threshold is that TE always instantaneously accounts for the local background IVT field, allowing it to act similarly to ARDTs which employ relative IVT thresholds but in a more flexible manner.

Chapter 3

Sensitivity of Atmospheric River Vapor Transport and Precipitation to Uniform Sea-Surface Temperature Increases

This is a slightly modified version of a manuscript published in *Journal of Geophysical Research: Atmospheres* as:

> **McClenny, E. E.**, Ullrich, P. A., & Grotjahn, R. (2020). Sensitivity of atmospheric river vapor transport and precipitation to uniform sea surface temperature increases. *Journal of Geophysical Research: Atmospheres*, 125, e2020JD033421. https://doi.org/10.1029/2020JD033421

Abstract

Filaments of intense vapor transport called atmospheric rivers (ARs) are responsible for the majority of poleward vapor transport in the midlatitudes. Despite their importance to the hydrologic cycle, there remain many unanswered questions about changes to ARs in a warming climate. In this study we perform a series of escalating uniform SST increases (+2, +4, and +6K, respectively) in the Community Atmosphere Model version 5 in an aquaplanet configuration to evaluate the thermodynamic and dynamical response of AR vapor content, transport, and precipitation to warming SSTs. We find that AR column

integrated water vapor (IWV) is especially sensitive to SST and increases by $6.3 - 9.7$ percent per degree warming despite decreasing relative humidity through much of the column. Further analysis provides a more nuanced view of AR IWV changes: since SST warming is modest compared to that in the mid-troposphere, computing fractional changes in IWV with respect to SST results in finding spuriously large increases. Meanwhile, results here show that AR IWV transport increases relatively uniformly with temperature and at consistently lower rates than IWV, as modulated by systematically decreasing low-level wind speeds. Similarly, changes in AR precipitation are related to a compensatory relationship between enhanced near-surface moisture and damped vertical motions.

3.1 Introduction

Atmospheric rivers (ARs) are shallow (up to 4 km deep), filamentary ($<$ 1000 km wide, $\sim$ 2000 km long) streams of concentrated vapor typically found in the extratropics and midlatitudes (Ralph et al., 2004a; Cordeira et al., 2013; Ralph et al., 2018). While ARs occupy only $\sim$ 10% of the Earth's zonal circumference in the midlatitudes, they perform virtually all of the meridional vapor transport outside of the tropics (Zhu and Newell, 1998; Ralph et al., 2004a). When AR vapor is lifted—for instance, by mountain barriers or the warm conveyor belt of an extratropical cyclone (ETC)—they can produce substantial precipitation. According to a study performed by Paltan et al. (2017), ARs alone are responsible for 22% of annual total global runoff. As prominent features of the global hydrological cycle, the variability of ARs has important consequences for global energy balance and regional water resources. In particular, understanding the response of AR precipitation to increasing surface temperatures is a significant open topic today.

The Clausius-Clapeyron (CC) relation predicts a $\sim$ 6-7 percent increase in saturation vapor pressure (e^*) near the surface for each Kelvin increase in surface temperature (Trenberth et al., 2003). While this figure only applies to local changes, global-mean column-integrated water vapor (IWV) nevertheless increases at approximately CC rates (Held and Soden, 2006; O'Gorman and Muller, 2010), though significant regional variations exist (O'Gorman and Schneider, 2009a). Although mean state changes may not

hold for individual weather events, AR IWV has increased at rates comparable to that predicted by CC, in turn resulting in greater integrated vapor transport (IVT) in studies comparing present-day (PD) and Representative Concentration Pathway (RCP) 8.5 end-of-century (EOC) conditions (Warner et al., 2014; Payne and Magnusdottir, 2015; Shields and Kiehl, 2016). Gao et al. (2015) explicitly tested the enhancement of AR IWV with respect to near-surface temperatures by isolating the thermodynamic and dynamical contributions to AR IVT under PD and RCP8.5 conditions, and found that AR IWV followed a "super-CC" increase. In other words, the CC relation appeared to under-predict the change in AR IWV compared to that actually measured, which Gao et al. (2015) attributed to AR vapor originating from a warmer ocean basin that was not included in their calculations. However, it has since been argued that such "super-CC" increases in AR IWV are consistent with the approximately saturated, moist-neutral conditions characteristic of strong ARs (Ralph et al., 2017). Specifically, latent heat release aloft enhances upper-tropospheric warming with respect to surface warming, thereby driving AR IWV increases beyond CC predictions conditioned on surface temperatures (Payne et al., 2020). Such a result has been noted previously in zonal mean IWV studies (O'Gorman and Schneider, 2009a,b), as well as orographic precipitation studies (Siler and Roe, 2014), but not strictly tested with respect to ARs.

Global-mean precipitation rates will increase at lower fractional rates than global-mean IWV due to energetic constraints (2-3% per K surface warming; Held and Soden, 2006; O'Gorman and Muller, 2010; O'Gorman et al., 2012); likewise, theoretical considerations for AR precipitation rates also predict lower fractional enhancement than for AR IWV. Since strong ARs are approximately moist-neutral (Ralph et al., 2017), it is expected that their internal vertical velocities will not change appreciably as the climate warms (O'Gorman, 2015); given this, it can be shown that extreme, non-orographic AR precipitation rates will increase fractionally at the rate of near-surface e^*, which is lower than that for AR IWV (Payne et al., 2020). Since orographic enhancement is a frequent driver of extreme AR precipitation (e.g., Ralph et al., 2006), the previously described changes in the vertical structure of atmospheric moisture have additional consequences.

Specifically, the amplified warming aloft also drives the largest fractional increases in condensation higher in the column, in turn limiting moisture availability for precipitation on the windward side: Siler and Roe (2014) found that orographically enhanced precipitation increased at larger rates on the leeward side of a mountain range than upsteam of the crest (12.2% versus 8.8%). Another study comparing historical and RCP8.5 ARs in a 29-member ensemble found a 35% increase in the number of AR days, but only a 28% in AR days associated with extreme precipitation (Hagos et al., 2016). Last, Warner et al. (2014) examined US west coast ARs in a 10-member model ensemble under historical and RCP8.5 conditions, and found that AR IVT increased by 25-30% while offshore AR precipitation rates increased by 15-39%, though they noted that uneven surface warming may have contributed to the ranges of the calculations.

Theory-based predictions for AR moisture transport and precipitation provide excellent physical context, but can be difficult to test in "comprehensive climate models" (here defined as those which contain sea ice, land, and an interactive ocean) due to the sheer complexity of their many interacting components (Held, 2005). Therefore, we suggest that a simplified experiment design will help elucidate the thermodynamic and dynamical drivers of AR moisture transport and precipitation. Specifically, we suggest that the use of an aquaplanet (AQP) model—a water-covered world without land, sea ice, interactive ocean, or topography (Neale and Hoskins, 2000)—is ideally suited for such a study. Previous studies have leveraged the simplified AQP framework to isolate the physical drivers of AR activity (Hagos et al., 2015; Swenson et al., 2018). Likewise, we use an AQP here to isolate SST forcing from other climate change effects (e.g., differential land-sea warming) inherently present in comprehensive climate models, while the use of uniform SST increases can help us further rule out impacts from changing meridional SST gradients. Hence, we set out here to study the thermodynamically and dynamically driven changes of AR moisture transport and precipitation to a series of progressively larger uniform SST increases in an AQP model. Specifically, this research investigates the following questions:

- What are the thermodynamic responses of AR moisture transport and precipitation rates to a collection of uniform SST increases?

- How do dynamic quantities (e.g., midlatitude circulation, wind) respond to increasing SSTs?
- How do these dynamic quantities serve to enhance or damp changes in AR vapor transport and precipitation?

In all, this study seeks to contextualize AR climate change statistics—whether those established from observations or from studies in comprehensive climate models—by isolating the impacts of warming SSTs. We will not only test physical linkages between SST increases and AR statistics, but will break down more complex AR processes (e.g., precipitation) into simple constituents (e.g., near-surface specific humidity and vertical velocity) to further our understanding.

A secondary goal of this manuscript is the introduction of a simple and novel AR detection tool (ARDT) developed as part of the TempestExtremes framework (Ullrich and Zarzycki, 2017). Unlike other ARDTs in the literature (e.g., see Shields et al., 2018) the proposed scheme relies on a threshold on the Laplacian of the IVT (rather than the IVT itself). This has the advantage of detecting AR structures as ridges in the IVT field regardless of changes to the background that occur in response to surface warming. An optional algorithm for filtering tropical cyclone objects is also described.

This paper is organized as follows: Section 3.2 outlines methods, including model parameters and detection tools; Section 3.3 presents relevant AR, non-AR, and total (AR + non-AR) statistics, including column-integrated quantities as well as vertical profiles for all runs; finally, Section 3.4 provides a brief summary of our findings, as well as concluding thoughts.

3.2 Methods

3.2.1 Model setup

We use the Community Earth System Model (CESM) Version 2 with Community Atmosphere Model version 5 (CAM5) physics (Neale et al., 2010). The spectral element dynamical core is employed with NE60 horizontal resolution (0.5° average spacing between degrees of freedom along the equatorial band). Output is remapped to a uniform

0.5° finite volume grid using the TempestRemap software suite (Ullrich and Taylor, 2015; Ullrich et al., 2016) before calculating derived variables, detecting ARs, or performing analyses.

To isolate the influence of SST on AR precipitation, we run CAM in its AQP configuration, meaning it has no land, sea ice, or topography; it is a water-covered world. We prescribe a data ocean in which SST thermally forces the atmosphere while remaining fixed. As a "Baseline" SST scenario, we use the "QOBS" profile from Neale and Hoskins (2000), while the warming scenarios feature +2K, +4K, and +6K uniform SST increases over QOBS, respectively. This uniform increase includes polar regions: where the original QOBS formulation sets SST poleward of 60° at 0°C, we set these points equal to the uniform SST increase to prevent effects associated with a changing meridional SST gradient.

All SST scenarios are symmetric about the equator and zonally uniform; solar radiation is fixed at perpetual-equinox conditions, and there is no axial tilt. Carbon dioxide concentrations for all runs are set at a uniform 348 ppm (the default value for CAM5 AQP), aerosol cloud interactions are turned off, and the only aerosol emissions come from sea salt, which the model diagnoses from surface wind. The zonal and hemispheric homogeneity of the boundary conditions, along with the lack of seasonality, allows for many more ARs under the same boundary conditions and forcing, so the sample size reduces confidence bounds. Medeiros et al. (2016) found that two-year, zonal mean statistics for water vapor, horizontal and vertical winds, and precipitation were statistically robust with respect to a 16-year total AQP run. Similarly, Yang et al. (2013) found that a single year provided stable statistics for zonal mean precipitation extremes in a five-year AQP experiment. Testing of our own determined that zonal mean AR statistics converged within 18 months (Figure A.1), so we maintain that the 30 months of statistics shown here sufficiently capture bulk AR properties. Last, insofar as the northern and southern hemispheres of an aquaplanet can be considered independent from one another, we average both hemispheres together and consider it as virtually doubling the sample size, leaving us with effectively $2N$ months of data for each SST scenario, where $N = 30$.

3.2.2 AR detection

The American Meteorological Society (AMS) definition for AR contains little quantitative guidance (AMS, 2017), allowing for flexibility in ARDT development but also contributing to differences across ARDTs. These differences, which include variations in terms of detection variable (e.g., IWV, IVT, etc.), thresholds on the intensity of detection variables, geometry, event persistence, and/or other detection considerations, can ultimately affect conclusions about AR characteristics and impacts (Shields et al., 2018; Rutz et al., 2019; O'Brien et al., 2020; Payne et al., 2020). While some ARDTs rely on relative moisture thresholds derived from climatology (e.g., Lavers et al., 2012; Guan and Waliser, 2015), others use absolute thresholds for either IWV (Ralph et al., 2004a; Wick et al., 2013a) or IVT (Equation 3.2.1) (Leung and Qian, 2009; Rutz et al., 2013). In general, ARDT authors tend to condition AR detection on IVT rather than IWV, in part because a pure IWV threshold does not capture the nature of ARs as midlatitude processes that transport moisture, as well as because IWV thresholds capture too much of the tropical moisture belt. We compute IVT as:

$$IVT = \sqrt{\left(-\frac{1}{g}\int_{p_0}^{p_T} qudp \right)^2 + \left(-\frac{1}{g}\int_{p_0}^{p_T} qvdp \right)^2} \tag{3.2.1}$$

where $p_0 = 1000$ hPa, $p_T = 300$ hPa, g is gravitational acceleration, q is specific humidity, and u and v are the zonal and meridional wind velocities, respectively.

We use an original, objective ARDT which is available as part of the TempestExtremes (TE) software suite (Ullrich and Zarzycki, 2017; Zarzycki and Ullrich, 2017). TE uses the following criteria to detect AR conditions (i.e., the presence of an AR at an individual time step) at a latitude-longitude grid point:

1. The grid point is poleward of 20°N/S

2. The Laplacian of IVT at the grid point is < -40000 kg m^{-1} s^{-1} rad^{-2}. We compute this using an 8-point discrete Laplacian with a stencil radius of approximately 800 km, about the mean AR width found both in an observational study by Ralph et al. (2017) as well as a reanalysis study by Guan et al. (2018).

3. The grid point is part of $\geq$ 50 connected grid points (an area of approximately 125,000 km^2) which meet the above criteria, as determined via a simple floodfill algorithm. This area requirement removes pointwise enhancements in the IVT field which would otherwise be counted as ARs, and we found that no explicit length or width requirements beyond this were necessary to achieve a sampling of ARs with a characteristic filamentary shape.

4. The grid point does not belong to a tropical cyclone (see Section 3.2.3 for details)

We emphasize here two important points about our ARDT. First, our use of an absolute threshold for the Laplacian of IVT, rather than for IVT itself, allows TE to act similarly to a "relative" ARDT (e.g., an ARDT conditioned on climatological IVT percentiles; see Shields et al., 2018; Rutz et al., 2019) and precludes any necessity to enforce different detection thresholds despite the different background climatology of each SST run. This is because the Laplacian identifies regions where IVT has increased to a ridge over a short distance ($\sim$ 800 km) relative to the local background IVT. Offline sensitivity tests determined that the Laplacian threshold was sufficiently strong that it never captures points that do not satisfy the threshold of IVT $>$ 250 kg m^{-1} s^{-1} typically used for ARs (Shields et al., 2018; Ralph et al., 2019). Therefore, whenever this manuscript references ARs in the context of those detected by TE, it refers to any object whose IVT represents a local ridge in the field. We recognize that our detection criteria often results in the inclusion of tropical cyclones (TCs), so we filter them out with a separate detection criteria (see Section 3.2.3 for details). Second, the Laplacian threshold, its radius, and the grid point number (area) requirement were all determined via manual inspection of detected objects. These thus represent tuning parameters in the ARDT and should not be taken as absolute. For reference, we included TE in the Atmospheric River Tracking Method Intercomparison Project (ARTMIP; see Shields et al., 2018; Rutz et al., 2019), which seeks to quantify how differing ARDTs result in differing AR statistics. Within these studies, TE tends to exhibit behavior close to the median for relevant AR statistics, relative to the entire ensemble of ARTMIP ARDTs (Shields et al., 2018; Rutz et al., 2019).

Figure 3.1 shows a snapshot of TE-identified ARs against fields of (a) IVT and (b)

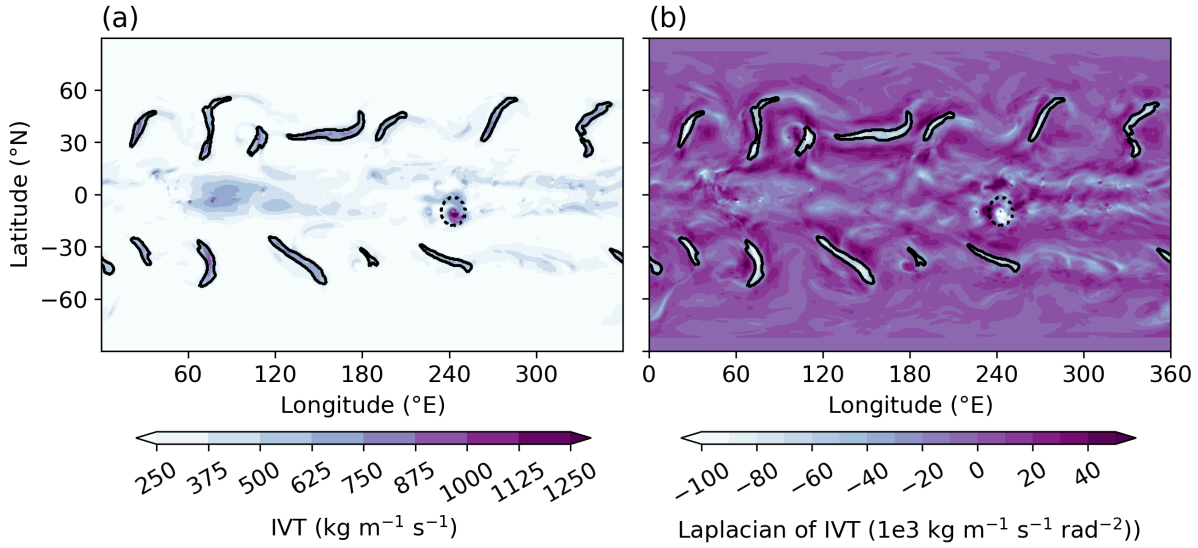

Figure 3.1: Snapshot of ARs (solid black outlines) as well as a TC (dotted black outlines) as identified by TE. We show them here on a field of (a) IVT and (b) the Laplacian of IVT from the Baseline SST run.

the Laplacian of IVT for reference. Note that IVT values within AR contours always meet or exceed the typical AR criteria of 250 kg m^{-1} s^{-1}, even without this threshold being explicitly enforced (Figure 3.1a). To capture the bulk AR climatology for each run, we also compute an AR occurrence frequency (OF), defined here as the percent of time steps in which TE has identified AR conditions at any given latitude-longitude grid point. Since these results are independent of zonal coordinate, we show the zonal mean AR OF in Figure 3.2a. With each +2K increase in SST, AR OF both increases overall and experiences a robust poleward shift in its maximum. This shift is likely driven by a similar poleward shift in the location of the eddy-driven jet, which we discuss in Section 3.3.1. Meanwhile, the overall enhancement in AR OF under warming SST conditions can be due to changes in the number of ARs, the zonal extent of AR objects, and/or an increase in the average duration of ARs. We find that the largest contribution comes from the average zonal extent of individual AR objects (that is, the average number of grid points in the zonal direction occupied by an individual AR object; nominally a measure of AR width without taking AR axis into account), which expands systematically as SSTs warm, especially in the lowest and highest latitudes of the test domain (Figure 3.2b).

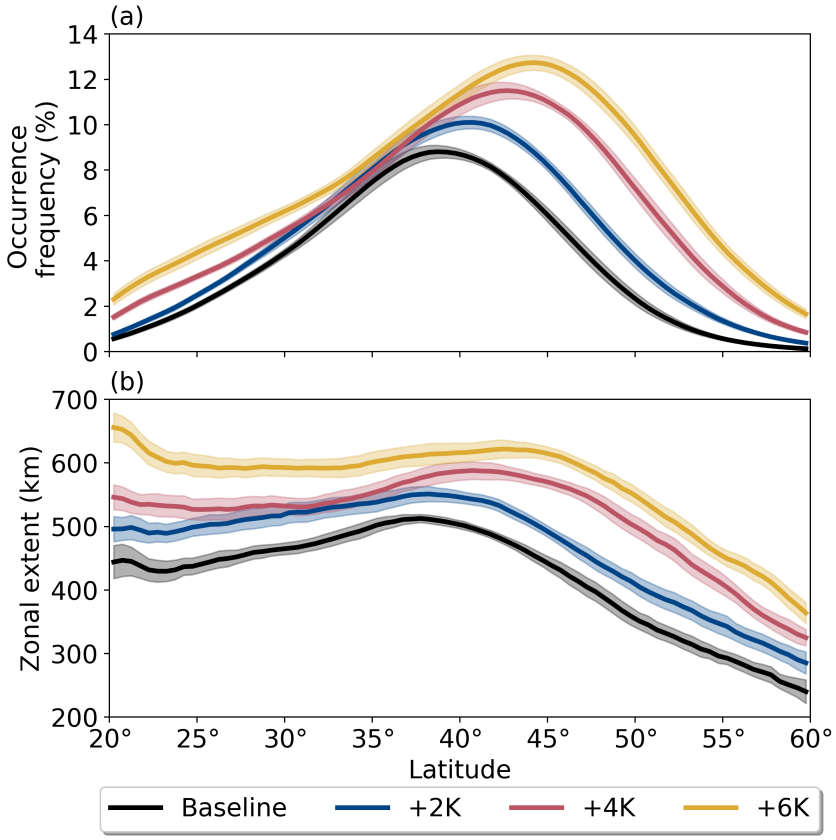

Figure 3.2: Zonal mean AR (a) occurrence frequency and (b) zonal extent for each SST run. Shading shows the 95% confidence intervals, computed with respect to $N = 20$ three-month ensembles.

Espinoza et al. (2018) similarly reported enhanced AR OF due to expanding AR length and width under climate change conditions using an independently developed ARDT.

The extent of the AR "widening" produced by TE can be explained in part by multiplicative IVT increases since the multiplicative factor carries over into the Laplacian, but it is unlikely to be the only driver: assuming that AR IVT exhibits a Gaussian profile, it can be shown that a uniform 50% increase in IVT only results in a $\sim 1\%$ wider AR (Text A.1). In any case, the increased width of AR objects does imply some care needs to be taken when assessing zonal mean AR statistics—namely, the added points at the periphery of the AR objects are likely to be different in character than the AR core, which is characterized by the most extreme values of IVT. Subsequently, our analysis examines both the zonal mean statistics and histograms of relevant fields.

3.2.3 Filtering out tropical cyclones

One pitfall associated with the TE AR detection criteria used here is the identification as ARs of bands of high IVT associated with TCs. While ARs can occur in association with TCs and extratropical transition (e.g., Sodemann et al., 2013), our analysis focuses on AR conditions alone and not on related phenomena. Restricting AR detection poleward of 20° removes a substantial proportion of TCs and TC-like objects, but in order to ensure these objects are not incorporated in our analysis we additionally use a separate detection algorithm to filter them (Ullrich and Zarzycki, 2017; Zarzycki and Ullrich, 2017). TE's TC detection is used to mask out all variables within an eight-degree radius of grid points which meet the following criteria:

1. They are the most intense local minimum of sea-level pressure (SLP) within a 2.0° great-circle distance.

2. Their SLP increases by at least 375 Pa over a 3.6° radius.

3. Their 300 minus 500 hPa geopotential height thickness decreases by six meters over 7.5° (to detect warm-core storms). This criterion acts so as to only detect warm core storms and not eliminate extratropical cyclones.

Figure 3.1 shows an example TC detected by TE against fields of (a) IVT and (b) the Laplacian of IVT for reference. For further details on how TE detects TCs, we refer readers to Ullrich and Zarzycki (2017) and Zarzycki and Ullrich (2017). We note here that while removing TCs did not change our overall results substantially, it did remove spuriously high values of IVT, low-level wind speeds, and precipitation from AR zonal mean statistics between 20° and 25°.

3.2.4 Data and statistical tests

Due to zonal uniformity and symmetry of SSTs across the equator, AQPs lend themselves nicely to meridional distributions of zonal mean statistics. Hence, many statistics are presented in this form, and, due to the aforementioned hemispheric symmetry, are shown only for the northern hemisphere (although southern hemisphere statistics are incorporated in these plots as well). Furthermore, since we do not track ARs in time,

all analysis on AR variables (e.g., AR precipitation) is performed on a grid point basis, rather than over the entire AR object throughout all or part of its lifecycle. Therefore, all meridional distributions of AR variables discussed here may be better characterized as distributions of variables under "AR conditions" (i.e., TE has identified that grid point as belonging to an AR) in which all non-AR grid points are excluded from analysis. We evaluate significance throughout this manuscript at the 95% confidence level with respect to 3-monthly ensemble members with the northern and southern hemispheres treated as independent samples ($N = 20$). This is analogous to a series of seasonal-length ensembles.

Since some variables exhibit strong meridional variations in terms of their relative response, we stratify our analysis into four distinct, approximately equal-area latitude bands: lower subtropics (LST; $20.25 - 26.75°$); upper subtropics (UST; $30.25 - 37.75°$); lower midlatitudes (LML; $38.25 - 46.75°$); and upper midlatitudes (UML; $47.25 - 57.25°$). The relatively large gap between LST and UST exists because of a complex precipitation response in the area between those bands, as seen in Figure 3.10; we reserve discussion of precipitation for Section 3.3.5.

3.3 Results and discussion

We begin our discussion in Section 3.3.1 with a brief summary on the midlatitude circulation for each SST run, as it is important for understanding the AR environment. Next, Section 3.3.2 describes findings on IVT, the variable on which AR detection is conditioned and one of the most prominent features of ARs. We follow this up by roughly considering IVT as the product of IWV and low-level wind, thus allowing us to separate IVT into its thermodynamical (IWV) and dynamical (wind) contributions. These contributions are then analyzed in detail in Sections 3.3.3 and 3.3.4, respectively. Finally, AR precipitation is analyzed in Section 3.3.5.

3.3.1 Circulation response

The midlatitude circulation provides the large-scale dynamical background for ARs. We characterize the midlatitude circulation in terms of three metrics: the Hadley cell (HC) edge, the subtropical jet (STJ), and the eddy-driven jet (EDJ). The purpose of this section

is to provide a broad overview of the major circulation responses to SST increases in order to provide context for the AR responses described in later sections.

The HC edge defines the poleward extent of the region of subsidence associated with the HC's descending branch, where strong static stability suppresses precipitation. To locate it, we follow the work of Davis and Birner (2016) who define it as the latitude at which the column-integrated, zonal mean meridional stream function (MMS) first disappears poleward of the deep tropical MMS extrema. We use bilinear interpolation to find the precise latitude of the HC edge when it is between grid points, as in Davis and Birner (2016). Figure 3.3a depicts a kernel density estimate (KDE) of the daily-mean HC edge. Despite a slight discontinuity between the +4K and +6K runs, the HC edge generally shifts poleward as SST warms, a result which has been observed and analyzed previously (Frierson et al., 2007; Lu et al., 2007; Vallis et al., 2015; Tandon et al., 2013; Shaw et al., 2016; Maher et al., 2020).

Whereas the HC edge broadly defines regions of convergence and divergence through the tropics and subtropics, the tropospheric jets act as dynamical guides against which cyclones, and the closely related ARs, form and propagate. Statistics related to AR occurrence, landfall location, and moisture transport are impacted by the prevailing jet regime for a given ocean basin (Payne and Magnusdottir, 2015; Shields and Kiehl, 2016; Kim et al., 2019). Thus, we provide a short summary of EDJ and STJ statistics here, beginning with the EDJ.

To locate the EDJ, we use the method described in Woollings et al. (2010): we (1) perform vertical averaging from 925 to 700 hPa of the daily mean zonal wind fields between 15° and 70°; and (2) smooth the zonal mean using a 10-day Lanczos filter with a 61-day window (Duchon, 1979). We then denote the latitude of the daily maximum of this field as the EDJ position. Accumulated over the complete simulation, the KDE of the EDJ position is given in Figure 3.3b. We find that the EDJ position shifts poleward as SST increases, an unsurprising result given the uniform SST increases and the strengthening upper-level temperature gradient shown in Figure 3.7 (e.g., Shaw and Voigt, 2015). As the EDJ shifts poleward, it enhances static stability through the subtropics, similarly

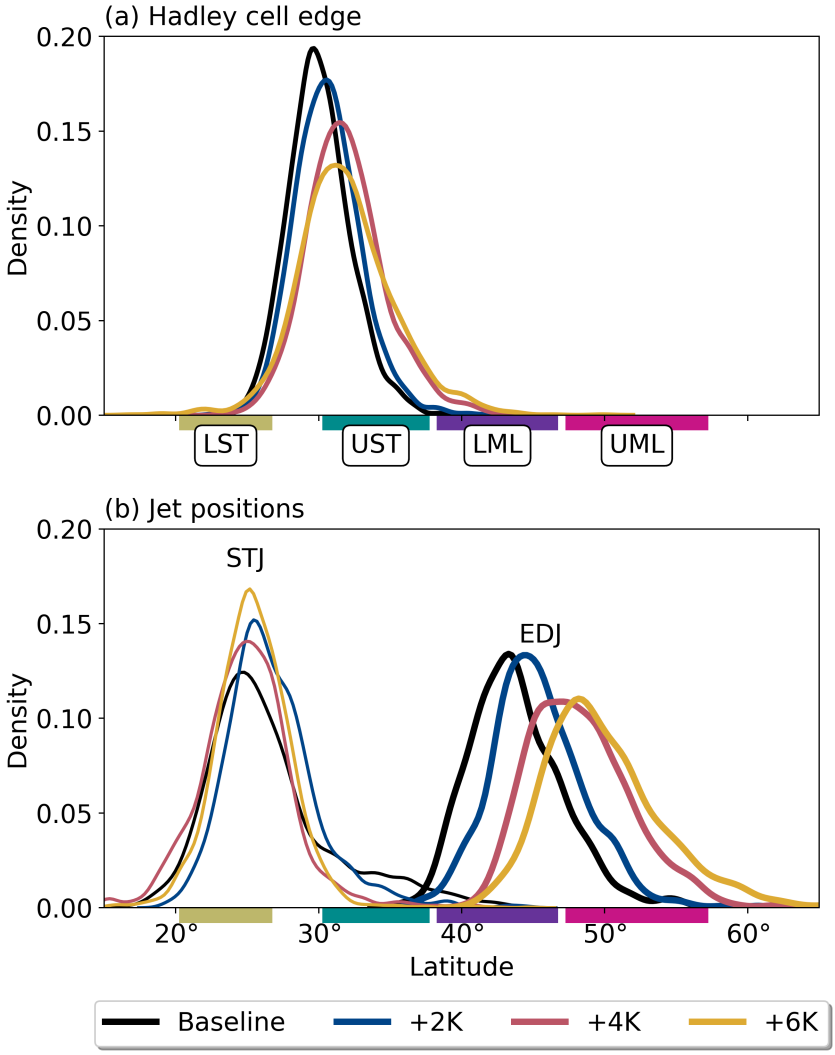

Figure 3.3: Kernel density estimates (KDEs) of (a) Hadley cell edge for each run and (b) subtropical jet (STJ; thin lines) and eddy-driven jet (EDJ; thick lines) positions. Colored boxes and accompanying labels on the x-axis denote the analysis subregions described in Section 3.2.4, and are shown here for reference.

pushing storm tracks and the HC edge poleward (Butler et al., 2010; Chang et al., 2012; Yin, 2017). Hence, the shift seen here in the EDJ is consistent with our results for the HC edge and AR occurrence frequency, both of which shift poleward with respect to the Baseline run (Figure 3.5).

Last, we find the STJ as in Davis and Birner (2016), who define it as the most equatorward zonal mean zonal wind maximum below 50 hPa after subtracting the surface zonal wind component to distinguish it from the EDJ. We remove the 850 hPa wind from the column instead as in Maher et al. (2020) and similarly find a distinct STJ core (Figure A.4). Figure 3.3b shows KDEs of daily STJ position for each SST run. Unlike the HC edge's systematic poleward shift as SST increases, the STJ location shows a discontinuous response characterized by a relatively large poleward movement in the +2K scenario but smaller poleward movements in the +4K and +6K scenarios, when measured with respect to the Baseline run. Even though the HC edge and STJ are frequently co-located, a "de-coupling" characterized by differing meridional shifts in the position of each has been described before (Davis and Birner, 2013; Maher et al., 2020). We also cannot rule out difficulties with separating the STJ from the EDJ (Medeiros et al., 2016), although this is less of an issue in the +4K and +6K experiments (Figure 3.3b). Another systematic response to uniformly warming SSTs is a strengthening of the STJ, as evidenced by higher zonal mean zonal winds in its core (Figure A.4). The STJ strengthening is likely related to the enhanced upper-level meridional temperature gradient in the subtropics as SSTs warm (Figure 3.7.)

3.3.2 Vapor transport

Figure 3.4 shows (a) meridional distributions of zonal mean IVT for all runs, as well as (b) the relative change between each warming run and the baseline (expressed as % per K). Solid lines show zonal averages over grid points in which AR conditions are present, whereas the dotted lines show zonal averages over non-AR grid points only. Finally, (c)-(f) show area-weighted fractional changes for each analysis subregion described in Section 3.2.4. We find that both AR and non-AR IVT increases with SST, though the response is not entirely uniform. While the change in AR IVT shown in Figure 3.4b appears virtually

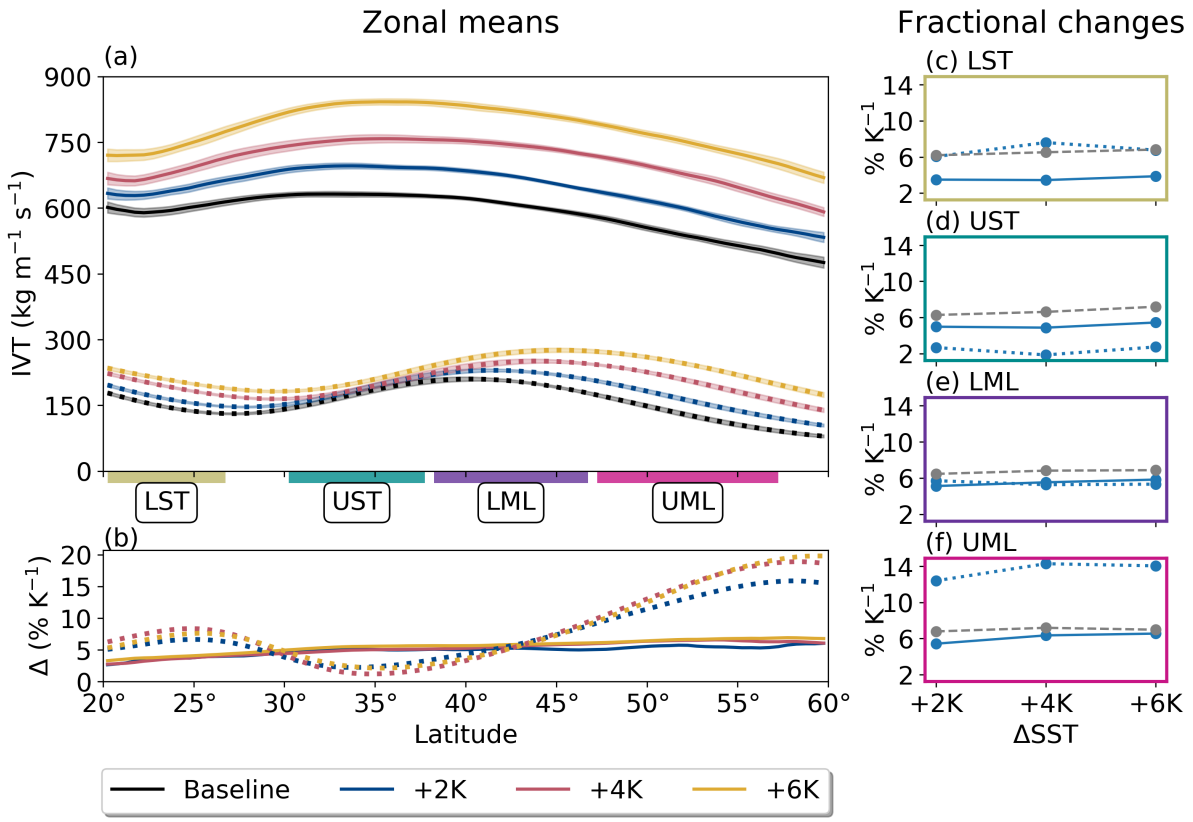

Figure 3.4: (a) Meridional distributions of zonal mean AR (solid) and non-AR (dotted) IVT. Shading shows 95% confidence intervals. (b) Relative differences with respect to the Baseline SST (% K^{-1}), using the same line color and style conventions. (c-f) Area-weighted mean relative change per K SST increase (blue; line style conventions as before). Grey dashed lines show changes in near-surface e^* as predicted by the CC relation computed with respect to the prescribed uniform SST increases, which we show here for reference.

flat and typically increases quite linearly at approximately 5% K^{-1}, the change through the LST is only about half as strong. The relatively uniform increase across latitudes in AR IVT contrasts the change in non-AR IVT, which is characterized by both an overall increase as well as poleward shifting maxima (moving from 40° to 46° under the +6K scenario) concordant with shifts in the EDJ position (Section 3.3.1). In terms of overall fractional changes, it is notable that non-AR IVT increases at higher rates than AR IVT in the LST and UML subdomains, at lower rates in the UST, and at similar rates in the LML.

We investigate changes in zonal mean IVT first by breaking it up into its zonal (uIVT)

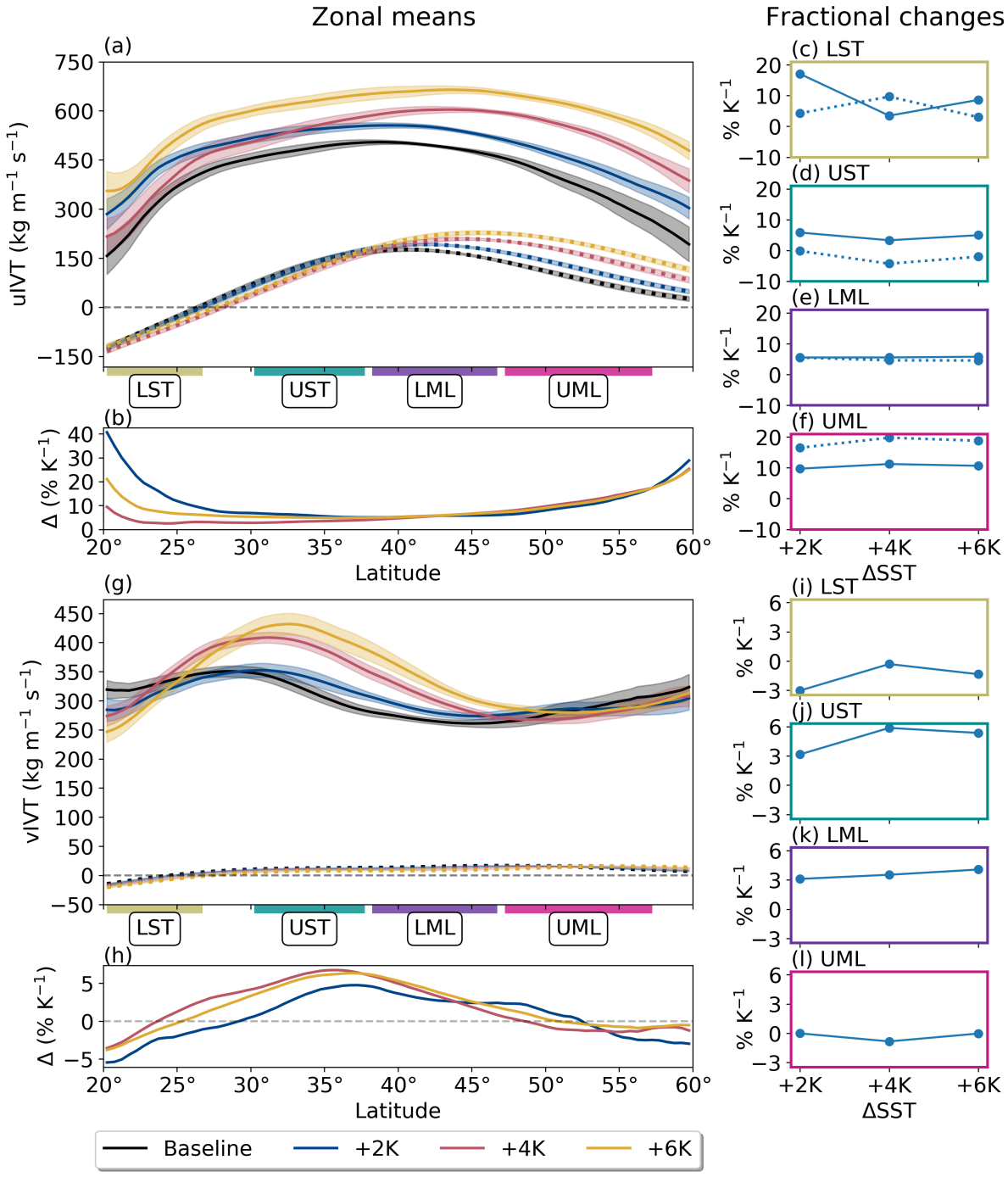

Figure 3.5: As in Figure 3.4, but for (a-f) zonal IVT (uIVT) and (g-l) meridional IVT (vIVT) components. Note the differences in ordinate scales. Also note numerical issues which prevented us from plotting some non-AR quantities: (1) non-AR uIVT is consistently near-zero between the LST and UST, resulting in an artificial inflation of relative changes in subplot (b), though the subregion means (c-f) were possible; (2) non-AR vIVT has a similar problem, though the values pass through the y-intercept in the LST; hence, we could plot neither the zonal (h) nor the regional (i-l) fractional changes.

and meridional (vIVT) components (Figure 3.5). Perhaps the most obvious feature emerging from this decomposition is the somewhat complementary relative changes between AR uIVT and vIVT: the largest relative increases in uIVT occur at the LST and UML, where vIVT decreases slightly; likewise, the largest increases in vIVT occur through the UST and LML subregions, where uIVT shows the smallest fractional change. Specifically, when it comes to changes in the direction of vapor transport, we show here that increasing SST leads to increasingly westerly AR IVT through the LST and UML, but does not substantially change transport direction through the UST and LML, where both uIVT and vIVT experience similar fractional increases. Nonetheless, the relatively localized increase in vIVT in the UST suggests an intensification in AR vapor advection from the subtropical moisture reservoir as SSTs increase. The changing pattern of AR vIVT out of the LST tracks with observed shifts in the STJ for each SST scenario (Figure 3.3b)—namely, AR vIVT is enhanced on the cyclonic side of the jet, and suppressed on the anticyclonic side—suggesting that the strengthening zonal flow of the STJ reduces AR-modulated interactions between the equatorward and poleward sides of the jet.

In non-AR regions, the poleward shift in IVT is exclusively due to an increase and poleward shift in westerly transport (uIVT), as meridional transport remains small (or even shows a small statistically insignificant decrease outside of the LST), a change likely facilitated by the poleward shift in the EDJ (Figure 3.3). Given that vIVT in non-AR regions is small, moisture transport into the midlatitudes appears increasingly dominated by ARs as SSTs increase. Since no corresponding increase in moisture flux occurs in the UML, we thus expect that precipitation increases in the LML will be largely due to increases in AR precipitation.

3.3.3 Thermodynamic response

Figure 3.6 shows zonal mean IWV and its fractional change under uniformly increased SST forcing. AR and non-AR IWV both increase systematically with warming SSTs, with non-AR IWV changing at higher fractional rates than AR IWV in all domains except the LML, in which AR and total IWV change approximately equivalently. As with the CC relation for near-surface e^* (grey lines on Figure 3.6c-f), IWV increases are enhanced

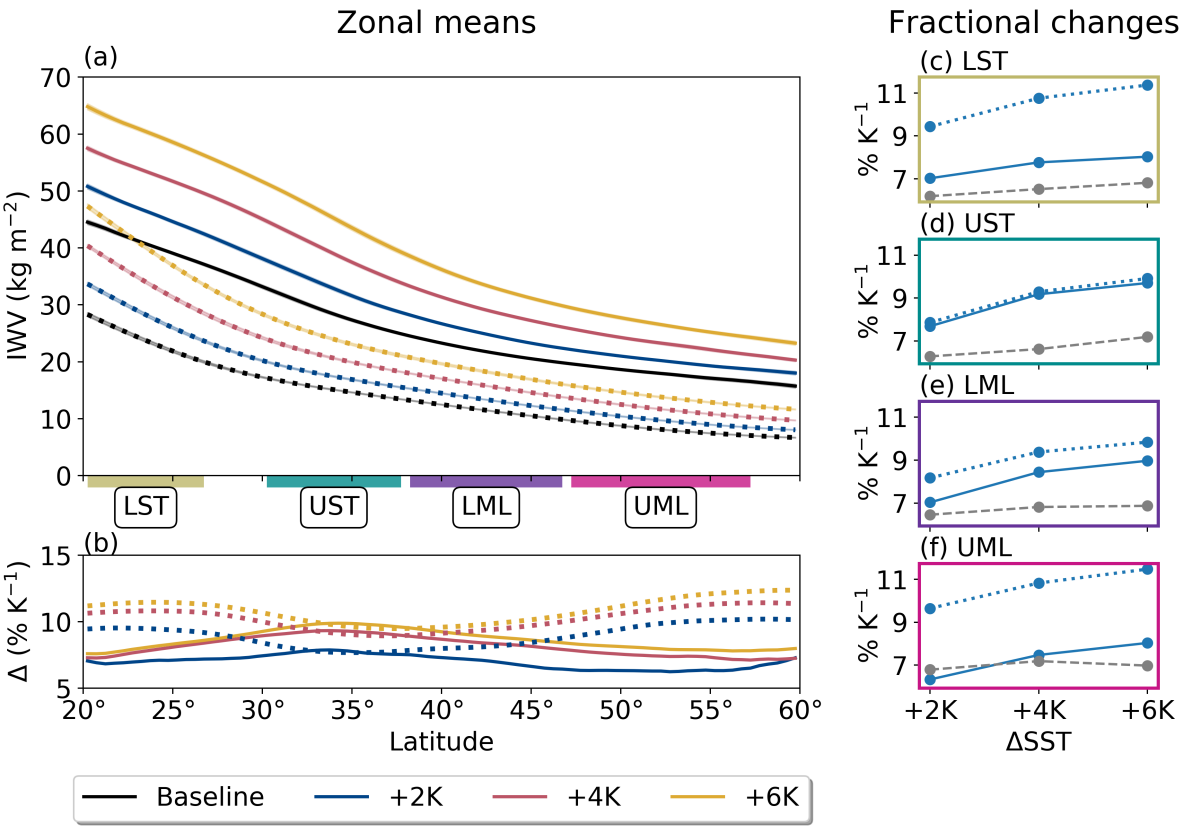

Figure 3.6: As in Figure 3.4, but for IWV.

slightly for larger SST increases. However, the magnitude of IWV enhancement exceeds CC predictions for near-surface e^* when conditioned on SSTs (except for in the +2K UML).

Similar "super-CC" moistening rates in ARs have been observed before (Gao et al., 2015). However, the idealized aquaplanet explored in this paper allows us to more easily elucidate the relevant physical linkages. We begin by examining column temperatures: Figure 3.7 shows vertical profiles of zonal mean absolute temperature changes in AR and non-AR grid points. Although these profiles incorporate not only the cores of ARs but also their peripheries, the vertical distributions here nonetheless allow us to unravel one of the physical drivers of the zonal mean IWV signals seen in Figure 3.6. We find that the temperature response for AR grid points in all subregions and non-AR grid points through the LST and UST is consistent with a damping of the moist-adiabatic lapse rate, which can be shown to occur under surface warming conditions as a result of

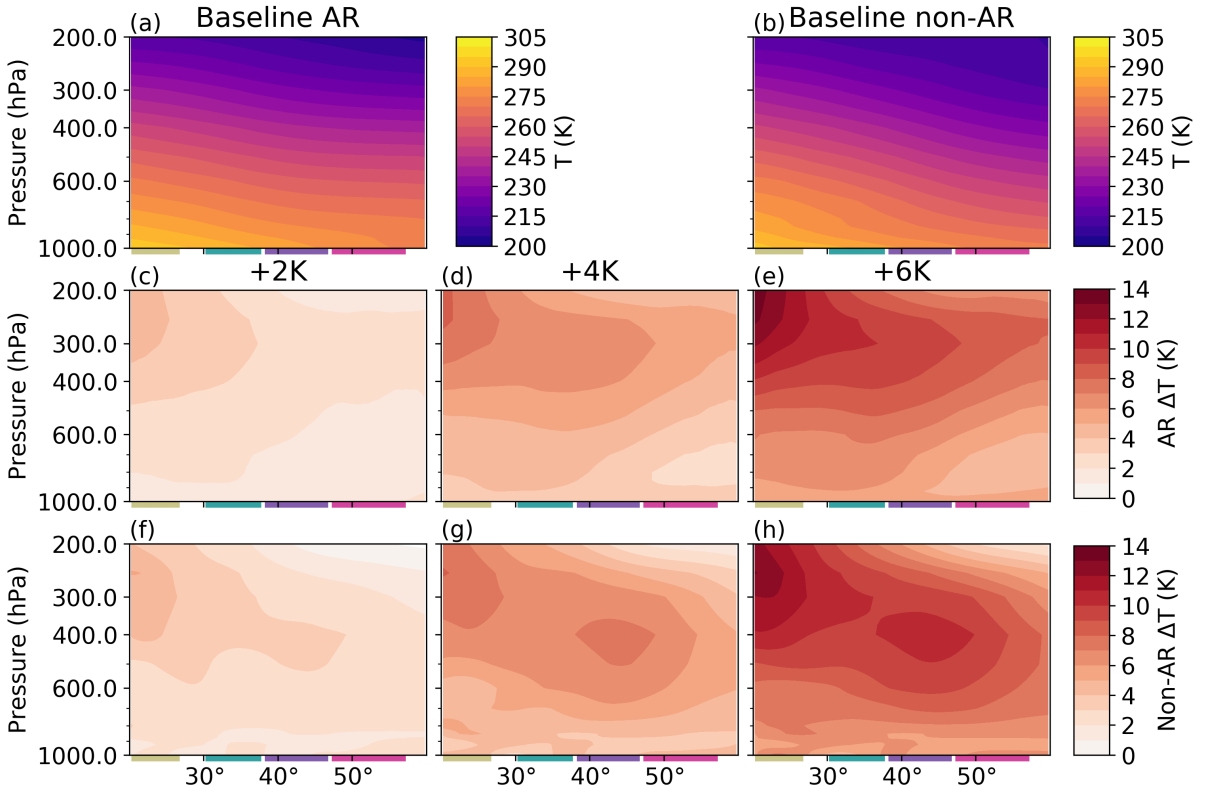

Figure 3.7: Vertical distributions of zonal mean absolute temperature in (a) AR and (b) non-AR grid points. (c-e) Vertical distributions of the absolute change in absolute temperature in AR grid points. (f-h) Vertical distributions of the absolute change in absolute temperature in non-AR grid points. Boxes delineating subregions are as for the previous figures, and are shown for reference.

enhanced latent heat release aloft (Siler and Roe, 2014; Payne et al., 2020). Meanwhile, the mid-tropospheric warming maximum in non-AR grid points in the LML and UML is similar to that seen in previous studies citing more complicated physical mechanisms for tropospheric warming in the midlatitudes which are beyond the scope of this manuscript (e.g., O'Gorman and Singh, 2013).

While the temperature analysis facilitated by Figure 3.7 provides a qualitative evaluation of model output with respect to theoretical predictions, it does not address why non-AR IWV tends to increase at higher rates than AR IWV (Figure 3.6). To investigate this, we leverage relative humidity (RH), an ideal variable in this scenario since it directly shows the departure of specific humidity from saturation specific humidity under a given SST increase, providing important context for the differing responses between AR

and non-AR IWV. To that end, Figure 3.8 shows vertical profiles of the absolute change of RH in AR and non-AR grid points for each SST run. These profiles show that RH decreases through most of the column and at most latitudes whether or not we select for AR conditions, though the decrease is generally larger at AR grid points. Since oversea mid-tropospheric RH decreases through the subtropics and midlatitudes have been noted before (e.g., O'Gorman, 2015), we focus our discussion here on changes within ARs. For a general RH decrease in AR grid points through the LST and UST, a role is likely played by largely sub-CC increases in surface evaporative fluxes (Figure A.6), which we note are consistent with previous thermodynamic studies (e.g., Held and Soden, 2006; O'Gorman and Muller, 2010; O'Gorman et al., 2012). Compounding this effect is an overall decrease in column moisture flux convergence (MFC) into AR grid points in the subtropics which is particularly strong in the LST (Figure A.7) and likely arises as a result of the poleward expansion of the HC edge (Figure 3.3). Meanwhile, despite decreasing condensation of AR moisture onto the surface in the LML and UML (Figure A.6), the sub-CC increases in MFC through these regions (Figure A.7) also likely contribute to RH decreases here. The only location where ARs get closer to saturation under SST increases is the UST mid-troposphere, though the RH increase here is very slight and is likely facilitated by enhanced meridional vapor advection out of the LST (Figure 3.5h).

3.3.4 Dynamic response

To broadly understand the dynamical component of AR IVT, we examine AR winds at the 850 hPa level. Zonal means show a robust decrease in AR 850 hPa wind speeds (Figure A.5), which we decompose into histograms of zonal and meridional winds taken over all AR points within each subregion (Figure 3.9). These distributions reveal that zonal winds at AR points generally weaken as SST increases, with the most robust of these decreases occurring through the UST and LML. Since the EDJ shifts from primarily occurring in the LML to the UML under higher SST conditions (Figure 3.3b), this slowing is likely related to a poleward shift in the strongest steering winds. Meanwhile, 850 hPa meridional winds in ARs show a more complicated response, characterized less by a systematic shift towards lower values, and more by an increased sampling of grid points featuring weak

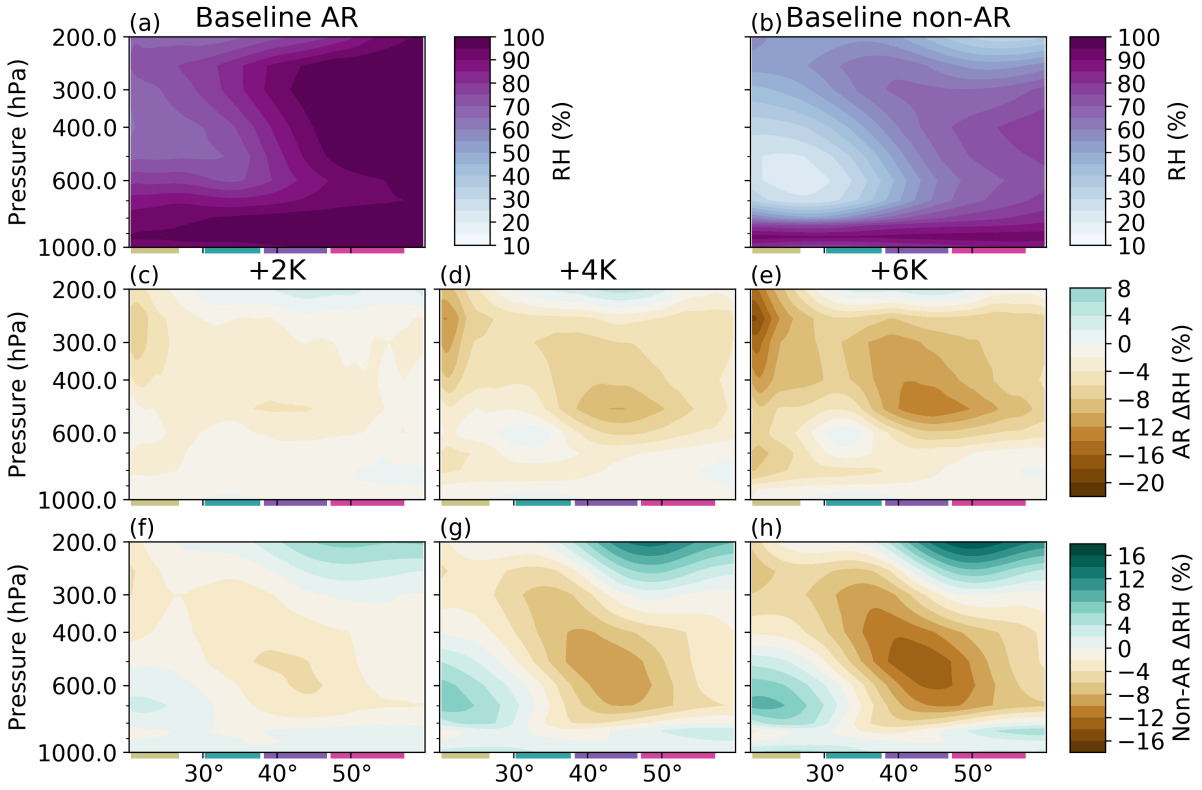

Figure 3.8: Same as Figure 3.7, but for relative humidity (RH; %).

or even equatorward meridional winds. That is, the upper tails of all four histograms ($>$ 20m/s)—representing points largely drawn from the AR core—exhibit essentially no change in meridional wind speed.

As stated earlier, we roughly consider IVT to be the product of IWV and low-level wind speed. With this in mind, the decreased magnitude of zonal mean IVT increases compared to IWV increases suggests that slowing winds attenuate the IVT response. We compactly show the compensatory relationship between IWV and low-level winds on IVT by returning to the weighted area-mean fractional changes of IVT and IWV (Figures 3.4 and 3.6) for each of our analysis subregions, and compute the same for 850 hPa wind speed (U_{850}). Following this, we describe a relative change in IVT as

$$\frac{\Delta IVT}{IVT} = \frac{\Delta IWV}{IWV} + \frac{\Delta U_{850}}{U_{850}} + r \tag{3.3.1}$$

where r is the residual value. We plug in the area-weighted fractional changes for IVT, IWV, and U_{850} to Equation 3.3.1, the results of which are summarized in Table 3.1.

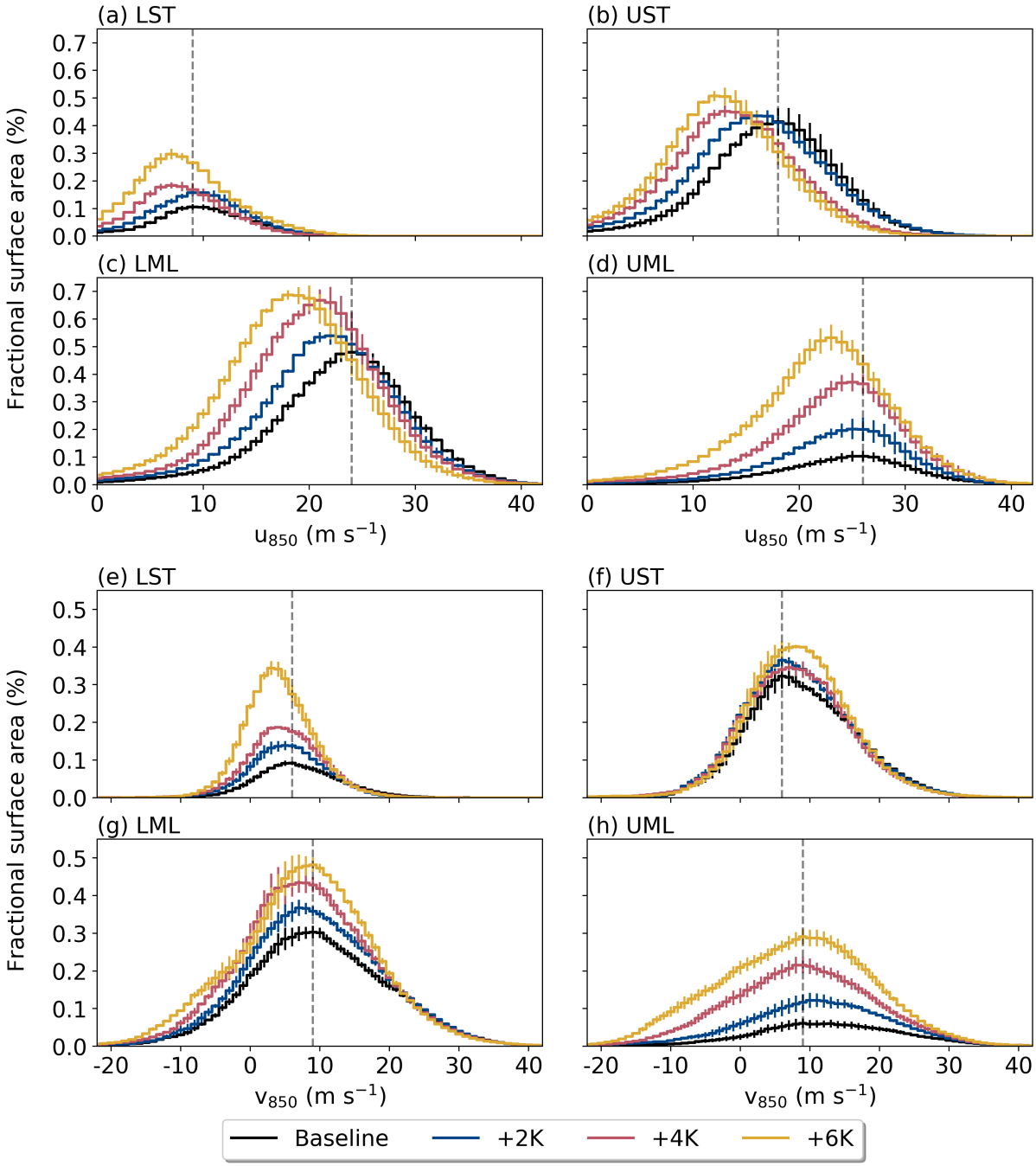

Figure 3.9: Histograms of AR (a-d) zonal wind at 850 hPa (u_{850}) and (e-h) meridional wind at 850 hPa (v_{850}) in each analysis subregion, with spacing at 1 m/s. Y-axis shows the fractional area of the subregion occupied by a particular bin value. Steps show the median of the three-month ensemble members, while error bars show the inter-quartile range with respect to $N = 20$ ensemble members. The gray, dashed lines show the mode of the Baseline histogram for reference.

		$\frac{\Delta IVT}{IVT}$	$\frac{\Delta IWV}{IWV}$	$\frac{\Delta U_{850}}{U_{850}}$	r
LST	+2K	**3.49** (6.04)	**7.03** (9.44)	**-5.51** (-2.11)	**1.97** (-1.29)
	+4K	**3.44** (7.59)	**7.77** (10.76)	**-4.33** (-1.07)	**0.00** (-2.10)
	+6K	**3.87** (6.76)	**8.03** (11.37)	**-4.22** (-1.69)	**0.06** (-2.92)
UST	+2K	**4.98** (2.68)	**7.69** (7.86)	**-2.96** (-4.10)	**0.25** (1.08)
	+4K	**4.87** (1.86)	**9.18** (9.29)	**-3.53** (-4.98)	**-0.78** (-2.95)
	+6K	**5.44** (2.74)	**9.70** (9.91)	**-3.12** (-4.13)	**-1.14** (-3.04)
LML	+2K	**5.11** (5.71)	**7.03** (8.17)	**-2.14** (-1.43)	**0.22** (-1.03)
	+4K	**5.53** (5.26)	**8.44** (9.38)	**-2.76** (-2.47)	**-0.15** (-1.65)
	+6K	**5.82** (5.32)	**8.97** (9.84)	**-2.50** (-2.37)	**-0.65** (-2.15)
UML	+2K	**5.43** (12.39)	**6.33** (9.65)	**-0.78** (3.02)	**-0.12** (-0.28)
	+4K	**6.35** (14.28)	**7.47** (10.83)	**-1.15** (3.10)	**0.03** (0.35)
	+6K	**6.55** (14.04)	**8.03** (11.48)	**-1.23** (2.26)	**-0.25** (0.30)

Table 3.1: Area-weighted mean relative changes for IVT, IWV, and U_{850} for each latitude band in all SST experiments. We also show the residual value, r, as expressed in Equation 3.3.1. AR values are expressed in boldface, while non-AR values are contained in parentheses. All values have units of % K^{-1} conditioned on the given uniform SST increase.

Performing this simplified analysis allows us to see the relative roles of thermodynamics (i.e., moisture fields) and dynamics (in this case, wind magnitude) in modulating AR and large-scale vapor transport. In particular, it allows us to see the opposition between the thermodynamic and dynamic components under warmer SST regimes. The generally small magnitudes of the r values in AR grid points indicates that absent changes in wind speed, AR IVT increases are approximated by those in AR IWV, a result which agrees well with several previous analyses (Dettinger, 2011; Lavers et al., 2013; Warner et al., 2014; Gao et al., 2015, 2016; Payne et al., 2020). Non-AR U_{850} values illustrate this especially well, as their changes do not represent a systematic decrease so much as a poleward-shifting maximum. As a result, non-AR IVT values in the LST, UST, and LML regions all increase at rates lower than non-AR IWV, while increases in UML non-AR IVT far exceed those of non-AR IWV, due to enhanced U_{850} at these high latitudes.

3.3.5 Precipitation

We move on now to perhaps the most widely associated feature of ARs. We begin by examining zonal means within AR and non-AR grid points, as in previous sections. From here, we examine the drivers of precipitation and its changes first by applying a simplified physical model of precipitation analogous to that found in Table 3.1. We follow this up by examining distributions of AR precipitation and vertical velocities in more detail. Last, we characterize changes in AR precipitation independent of changes in AR areal extent.

3.3.5.1 Bulk properties and drivers of AR precipitation

Figure 3.10 shows zonal mean 3-hourly average precipitation rates as well as the fractional change of those rates with respect to the prescribed SST increase. Non-AR precipitation exhibits a pattern consistent with the poleward shifts in the HC edge and the EDJ position (Figure 3.3), which together serve to enhance moisture flux convergence (MFC) in the UML and suppress it through the UST, though the MFC increase in the UML is very slight (Figure A.7). Generally speaking, this pattern is consistent with other thermodynamic scaling studies of mean precipitation rates (e.g., Held and Soden, 2006; O'Gorman and Schneider, 2009b), so we turn our focus now to AR precipitation, whose response shows a similar pattern to non-AR precipitation but with marked meridional shifts. For instance, like fractional changes in AR vIVT (Figure 3.5h) the spatial pattern of the AR precipitation response through the LST and UST (Figure 3.10b) tracks more closely with observed shifts in the STJ position than in the HC edge (Figure 3.3). Hence, while decreasing AR precipitation through the LST may be related to the expansion of the HC's descending branch through this subregion, we also suspect effects associated with changing patterns of convergence and divergence in the vicinity of the STJ.

To contextualize our findings on AR precipitation, we perform a simplified analysis similar to that performed for IVT in Section 3.3.4. To do so, we assume the local precipitation rate (P) of AR grid points over the ocean is roughly equal to the vertically integrated condensation rate; we can thus characterize it with the following proportionality:

$$P \sim \int_0^{p_s} \omega \frac{dq^*}{dp}\bigg|_{\theta_e} dp \tag{3.3.2}$$

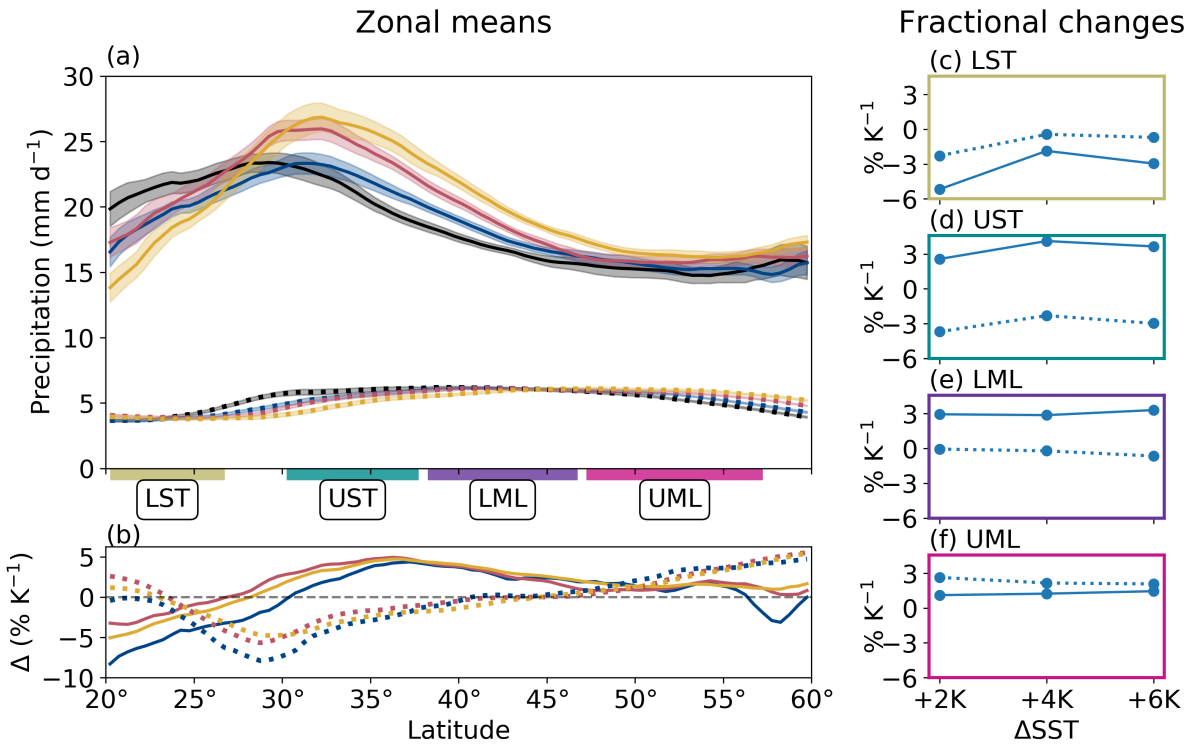

Figure 3.10: The same as Figure 3.4, but for 3-hourly average precipitation rate.

where ω is the vertical velocity in pressure coordinates and dq^*/dp is the vertical gradient of specific humidity evaluated along a moist adiabat with constant equivalent potential temperature θ_e. Given the moist-neutral thermal stratification of strong ARs (Ralph et al., 2017), dq^*/dp can be integrated in pressure coordinates to yield the surface specific humidity, q^*_{sfc}; since ARs are approximately saturated near the surface (Figure 3.8), we set $q^*_{sfc} = q_{sfc}$ at AR grid points. We furthermore simplify this relation by evaluating ω only at the 700 hPa level. Accordingly, a fractional change in AR precipitation can be expressed as:

$$\frac{\Delta P}{P} = \frac{\Delta q_{sfc}}{q_{sfc}} + \frac{\Delta \omega_{700}}{\omega_{700}} + r \tag{3.3.3}$$

As with the earlier IVT analysis (Table 3.1), we compute terms with respect to weighted areal means within each analysis subregion. The results of this analysis are summarized in Table 3.2. Generally speaking, residual values tend to be small (Table 3.2), indicating that Equation 3.3.3 captures changes in zonal mean AR precipitation rates reasonably well.

		$\frac{\Delta P}{P}$	$\frac{\Delta q_{sfc}}{q_{sfc}}$	$\frac{\Delta \omega_{700}}{\omega_{700}}$	r
LST	+2K	**-5.17**	**5.67**	**-11.89**	**1.05**
	+4K	**-1.87**	**6.31**	**-7.41**	**-0.77**
	+6K	**-2.96**	**6.63**	**-7.87**	**-1.72**
UST	+2K	**2.57**	**6.59**	**-3.38**	**-0.64**
	+4K	**4.12**	**7.17**	**-3.13**	**0.07**
	+6K	**3.66**	**7.58**	**-3.25**	**-0.68**
LML	+2K	**2.94**	**6.47**	**-4.08**	**0.56**
	+4K	**2.87**	**6.93**	**-5.25**	**1.19**
	+6K	**3.31**	**7.40**	**-4.31**	**0.22**
UML	+2K	**1.11**	**6.66**	**-4.97**	**-0.57**
	+4K	**1.24**	**7.09**	**-5.35**	**-0.50**
	+6K	**1.45**	**7.56**	**-4.84**	**-1.27**

Table 3.2: As for Table 3.1, but for Equation 3.3.3 instead and only considering AR grid points. Note that a negative change in the ω_{700} ratio means less vigorous upward motion (i.e., vertical velocities are getting more positive). Additionally, only AR values are shown because non-AR ω_{700} approaches 0 at some points in the UST, where relative changes will approach infinity (and thereby artificially inflate area-mean values).

We find the most substantial weakening in ω_{700} in the LST, coincident with the largest decrease in precipitation rates. Meanwhile, in the UST, where some of the largest precipitation increases occur, we also see the slightest weakening in ω_{700} and some of the largest near-surface q increases, suggesting that substantial increases in moisture may help overcome weakening upward motions in some regions. A similar explanation can be used for the LML, where fractional changes in AR precipitation follow a nearly linear increase with SST. While the UML also shows a nearly linear fractional increase in precipitation, the smaller magnitudes overall are facilitated by the stronger suppression of ω_{700} here. As for why vertical motions systematically decrease in magnitude under warming SST conditions, this outcome appears to be a consequence of weakening vertical temperature gradients (Section 3.3.3) and a subsequent strengthening in local static stability. We recognize that the enhanced static stability in the UML is likely somewhat

artificially inflated by the use of the prescribed SST, since a variety of mechanisms (e.g., atmosphere-ocean feedbacks, enhanced poleward latent heat flux by ARs and other processes) would normally lead to a larger SST increase here (e.g., Langen et al., 2012; Roe et al., 2015). Regardless, this analysis produces results similar to those for IVT, in that thermodynamic effects alone (q_{sfc}) serve to enhance AR precipitation, while dynamical effects (here ω_{700}) attenuate this enhancement (and in this case, even compensate for it sufficiently to decrease mean precipitation rates in the LST).

3.3.5.2 AR precipitation in more detail

We recognize that neither seasonal-length zonal means of AR precipitation rates (nor large-scale area integrals of them) are the most informative metric, especially when the most extreme AR events can lead to catastrophic flooding (e.g., Ralph et al., 2006). To that end, Figure 3.11a-d shows histograms of precipitation rates at AR grid points stratified by analysis subregion, alongside histograms of ω_{700} for reference (Figure 3.11e-h). We find an overall increase in our sample size for each subregion, consistent with increased AR occurrence and area (Figure 3.2). In the LST, this increase is notably more significant at precipitation rates below 20 mm/day, accounting for the observed decrease in mean precipitation rates here (Figure 3.10). Similarly, ω_{700} in the LST also exhibits an enhanced sampling of weaker grid points. We attribute this increased sampling of weaker precipitation rates and vertical velocities in this subregion to the large enhancement of AR zonal extent (Figure 3.2) here: by sampling more grid points at the periphery of AR objects, we also expect to sample grid points exhibiting less vigorous vertical velocities and lower precipitation rates. However, extreme precipitation rates (>70 mm/day) also cover more area within this region as SSTs increase, indicative of an enhancement in extreme precipitation and a larger spread in AR precipitation rates overall.

By contrast, both the UST and LML regions have marked increases in the most intense precipitation rates (> 70 mm/day) that are in turn responsible for driving up the mean precipitation rates. Interestingly, we do not see a similar uptick in intense vertical velocities in these subregions; however, as per the analysis presented in Table 3.1, enhanced AR precipitation rates here are related mostly to strongly enhanced AR moisture

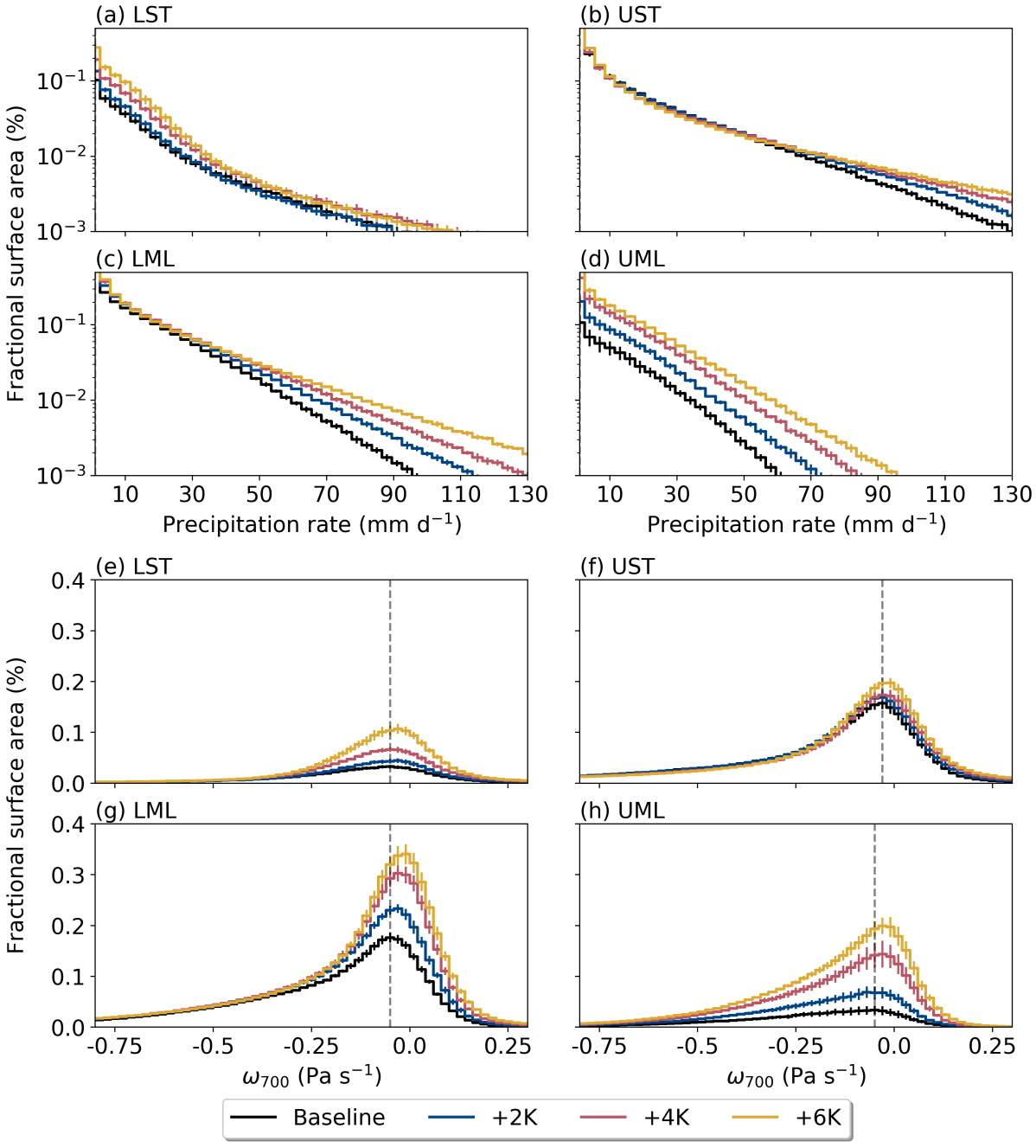

Figure 3.11: The same as Figure 3.9, but for 3-hourly average (a-d) precipitation rates and (e-h) pressure velocities at 700 hPa (ω_{700}). For (a-d), bin spacing is 1 mm/day with every third bin shown for clarity; we only consider points precipitating with a rate of at least 1 mm/day. For (e-h), bin spacing is 0.01 Pa/s, with every other shown.

in these subregions, rather than changes in ω_{700}. Last, UML precipitation histograms display near-uniform increases in the sampling of all precipitation rates, reflecting the smallest change in mean precipitation rates here (Figure 3.10). Similarly, histograms of ω_{700} in the UML show an enhanced sampling across a broad range of vertical velocities, both more and less negative than the Baseline mode. Regardless, these changes skew more towards positive ω_{700} values, accounting for the apparent damping of vertical velocities here.

3.3.5.3 Accounting for increasing AR area

We have discussed already that as SST increases in these experiments, so too does AR area. This enhancement in our sample size then makes it difficult to compare AR statistics across SST runs, particularly because means presented are obscured by an increased sampling of grid points farther from the narrow AR core which features the highest IVT and most intense oversea precipitation rates (Neiman et al., 2008). We first leveraged histograms of AR quantities to make comparisons despite unequal sample sizes, since that avoided issues associated with averaging AR core and periphery points together. Unfortunately, increasing AR area still makes histograms difficult to interpret, first because the upward shift can make left- or rightward shifts less obvious, and second because it cannot explicitly filter for core or periphery AR points.

We first wish to determine the contribution of changing AR area on mean AR precipitation rate changes. To that end, we compare fractional changes in AR area (AR_A; that is, the average combined area of all ARs in a given subregion) and AR area-integrated precipitation (P_A). Table 3.3 presents fractional changes of these quantities under SST increases.

We find that fractional increases in AR area are much larger than those in AR P_A in the LST, further supporting our assertion that decreases in mean AR precipitation rates here are related to enhanced AR areal coverage featuring weaker rates. The UST tells a different story however, with fractional changes in AR P_A exceeding those of AR area for all SST test runs, particularly the +4K and +6K scenarios. The precipitation distributions for this subregion (Figure 3.11b) show a marked increase in fractional area

		$\frac{\Delta P_A}{P_A}$	$\frac{\Delta AR_A}{AR_A}$			$\frac{\Delta P_A}{P_A}$	$\frac{\Delta AR_A}{AR_A}$
LST	+2K	**2.77**	**10.64**	UST	+2K	**5.97**	**5.78**
	+4K	**14.82**	**20.41**		+4K	**6.61**	**3.61**
	+6K	**15.12**	**24.75**		+6K	**6.47**	**3.55**
LML	+2K	**13.00**	**12.19**	UML	+2K	**34.25**	**37.23**
	+4K	**12.38**	**11.81**		+4K	**48.22**	**50.01**
	+6K	**11.27**	**9.88**		+6K	**50.42**	**54.83**

Table 3.3: Fractional changes of mean area-integrated AR precipitation (P_A) and AR area coverage (AR_A) in each analysis subregion (% K^{-1}).

occupied by intense AR precipitation rates ($\geq$70 mm/day) under higher SST conditions, allowing fractional increases in AR P_A to surpass those in AR area. ARs in the LML behave similarly, though fractional changes in AR P_A only just outpace those in AR area. Again, histograms of precipitation in this subregion (Figure 3.11c) provide additional context for these changes: much of the increased areal extent of AR precipitation occurs at above-average rates ($\geq$30 mm/day), facilitating the observed slight acceleration of changes in AR P_A with respect to AR area. Finally, results in Table 3.3 for the UML reinforce expectations set up by the precipitation distributions (Figure 3.11d), wherein nearly-equivalent changes in AR P_A and AR area are supported by a relatively uniform rise in the occurrence of all AR precipitation rates.

Second, we test the hypothesis that computed area-mean AR precipitation changes (Figures 3.10c-f) are influenced heavily by an increased sampling of weak, periphery AR points which naturally feature lower precipitation rates. We do this by comparing total precipitation rates against total precipitation rates weighted with IVT values. We compute these "IVT-weighted" precipitation means (P_{IVT}) like so:

$$P_{IVT} = \frac{\int_A P \cdot IVT dA}{\int_A IVT dA} \tag{3.3.4}$$

where A is the area of the subregion and dA is the grid point area. This approach has a two-fold advantage: by weighting precipitation proportionally to IVT, it not only skews area means towards ARs without necessitating a binary AR filter, but also weights the

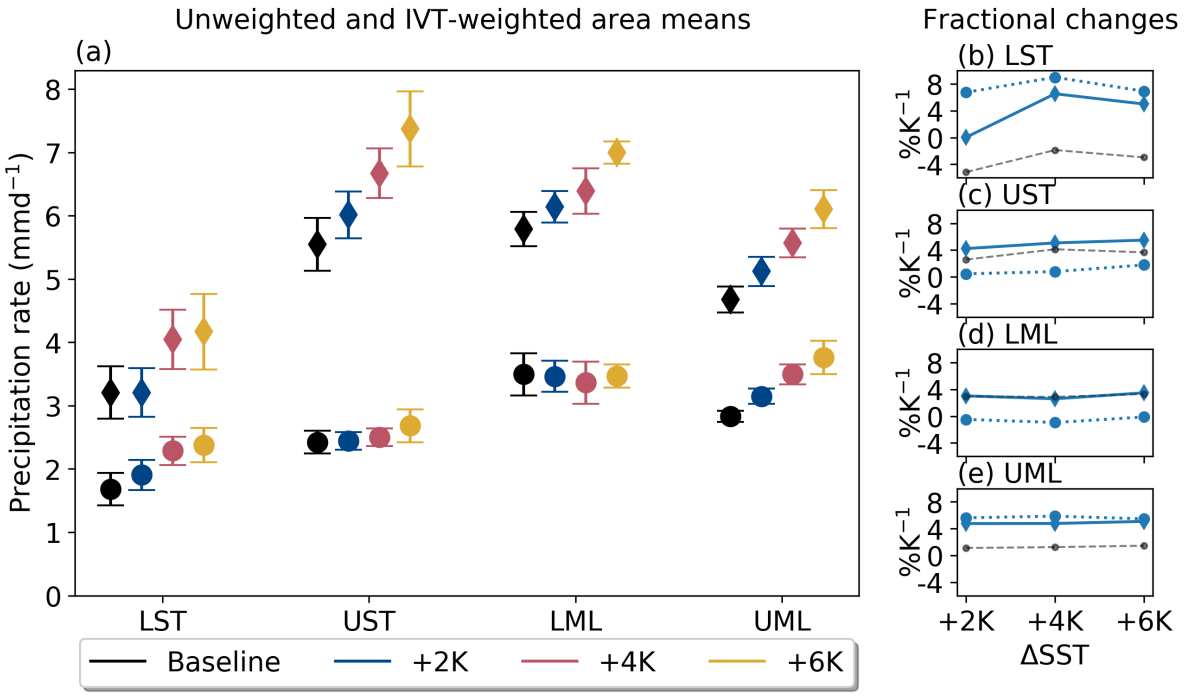

Figure 3.12: (a) Area-mean precipitation rates for all SSTs (mm/day). Circles indicate unweighted means, while diamonds indicate that the means were weighted by IVT values, as described by Equation 3.3.4. Markers show the median value with respect to the 20-member ensemble, while error bars show the interquartile range. (b-e) shows the fractional change in area precipitation means with respect to the Baseline for each uniform SST increase (% K^{-1}). We use dotted lines for non-weighted and solid lines for IVT-weighted, with line markers consistent with those used in (a). Gray, dashed lines show the same fractional changes in AR precipitation as in Figure 3.10c-f for reference.

analysis towards the highest IVT points found in ARs. Therefore, we consider the P_{IVT} means shown in Figure 3.12 analogous to precipitation rates in the high-IVT AR core. We thus compare fractional changes in them side-by-side with those computed directly for AR precipitation in Figure 3.12, in an effort to tease apart the effect of enhanced AR area on mean changes in AR precipitation rates.

In the LST in particular, we see a marked difference in the fractional changes of AR precipitation rates and P_{IVT}: while the former decreases as SST increases, the latter shows no change under the +2K scenario, and large increases in the +4K and +6K SST forcings of 6.54 and 5.00% K^{-1}, respectively (Figure 3.12b). For the UST, increases in P_{IVT} only slightly outpace those in AR precipitation rates (Figure 3.12c); since AR area does not increase more than AR P_A here (Table 3.3), we would not expect substantially larger

changes in P_{IVT} here either. Meanwhile, in the LML, changes in P_{IVT} track almost exactly with those in AR precipitation rates (Figure 3.12d), suggesting that increasing AR area does not play a large role in AR precipitation rate statistics in this subregion. Last, Figure 3.12e shows that P_{IVT} enhancement in the UML remains steady at approximately 5% K^{-1}, providing a stark contrast to the mean AR precipitation rate increases of approximately 1% K^{-1} here. Overall, this analysis indicates that high-IVT grid points such as those found in or near AR cores will feature regionally large enhancement in mean precipitation rates.

3.4 Conclusions

CAM5 was employed in its aquaplanet configuration (global, zonally-symmetric, prescribed SSTs) with uniformly increased SSTs of +2K, +4K, and +6K over the control "QOBS" profile (Neale et al., 2010). While certainly not a realistic model configuration or climate change signal, this experimental setup allowed us to isolate the impacts of increased SST on ARs, with the goal of evaluating fractional changes conditioned on SST of AR IVT, IWV, and precipitation rates, and validating the model response against more than a decade of theory. We detected ARs with an objective algorithm conditioned on finding local ridges in the IVT field at any given time step (i.e., the algorithm is insensitive to horizontal average increase in specific humidity). To facilitate simple regional comparisons, we divide our analysis domain into four subregions of approximately equal surface area.

We find that as SSTs increase so too does AR occurrence frequency, especially towards the higher latitudes in our test domain (Figure 3.2a). We attribute this domain-wide enhancement in AR occurrence frequency largely to an overall increase in the size of ARs, (defined here as "zonal extent"; Figure 3.2b), a result which agrees with previous work using an independently developed ARDT (Espinoza et al., 2018). Meanwhile, the steady poleward movement of AR occurrence frequency maxima under SST warming is related to a poleward shift in EDJ position (Figure 3.3b), another result in agreement with existing AR literature (Gao et al., 2016; Mundhenk et al., 2016; Shields and Kiehl, 2016).

Alongside changes in AR occurrence and morphology, we also find changes in AR vapor transport statistics. In general, ARs experience super-CC enhancement in IWV with respect to SST (from $\sim$ 6.3 to 9.7% K^{-1} depending on subregion and SST scenario; Figure 3.6), though the magnitude of this enhancement is in part a response to upper-tropospheric temperature increases that outpace those in SST (Figure 3.7). Since the large enhancement of warming in the upper troposphere arises as a natural consequence of a dampened moist-adiabatic lapse rate under surface warming conditions (e.g., Siler and Roe, 2014; Payne et al., 2020), we consider this result more reassuring than surprising. Similar rates of AR IWV enhancement have been observed in a coupled model (Gao et al., 2015) and shown to be related to enhancements in (a) CC sensitivity to below-freezing temperatures in the upper troposphere and (b) latent heat release aloft as the atmosphere moistens (Payne et al., 2020). Meanwhile, we find that AR IVT also increases, though it occurs at a lower rate than IWV for all subregions ($\sim$ 3.4 to 6.6% K^{-1}; Table 3.1). We perform a very simplified analysis of the dynamical and thermodynamical contributions to AR IVT (Equation 3.3.1) and find that this result is related to a systematic decrease in AR low-level winds speeds, which slow at fractional rates of $\sim$ -0.8 to -5.5% K^{-1} (Table 3.1).

Taken together, the relative changes in AR IWV and IVT are comparable to those seen in other studies (Warner et al., 2014; Gao et al., 2015) as is the finding that AR IVT will increase mostly due to thermodynamical effects (enhanced AR IWV) rather than dynamical ones (AR low-level winds) (Dettinger, 2011; Lavers et al., 2013; Warner et al., 2014; Gao et al., 2015, 2016). Dynamical changes are further observed in changing patterns of AR characteristics. Specifically, a poleward-shifting EDJ (Figure 3.3b) pushes ARs poleward with the storm track (Figure 3.2a), a result which is documented in comprehensive climate models (Gao et al., 2016; Shields and Kiehl, 2016). We also find an apparent connection between the STJ and AR vIVT characterized by a fractional enhancement of AR vIVT on the cyclonic side of the STJ, and a suppression of AR vIVT on its anticyclonic side (Figure 3.5g-h). Although the STJ shows a discontinuous response to SST increase (Figure 3.3b), the result suggests a relatively easily diagnosed large-scale

dynamical control on potential moisture sources for ARs.

Despite systematic increases in AR IWV and IVT, AR precipitation has a much more varied response across latitudes (~ -5.2 to 4.1 % K^{-1} ; Figure 3.10). Similar to our analysis on AR IVT, we perform a simplified calculation derived from theory to contextualize these changes in terms of dynamical and thermodynamical contributions (Equation 3.3.3), and generally find a compensatory relationship characterized by consistent increases in moisture (in this case, near-surface q) and a systematic damping in mid-troposphere vertical velocities (Table 3.2). An examination of precipitation distributions provides some important context for these findings: across all analysis subregions, the highest precipitation rates always increase, hinting at a robust enhancement in AR extreme precipitation even in areas where mean AR precipitation decreases (Figure 3.11a-d). Further complicating our results on mean precipitation rates is the finding that AR area increases as SST does (Figure 3.2b and Table 3.3). While AR area increases have been noted before (Espinoza et al., 2018), the enhanced AR area can nevertheless obscure interpretation of ARDT-derived conclusions about mean AR characteristics. Here, a simple analysis on AR area and precipitation (Section 3.3.5.3) shows that by sampling more grid points towards the weaker periphery of AR objects, fractional changes in zonal mean AR precipitation rates are damped in three out of four analysis subregions (Figure 3.12). Nonetheless, a clear enhancement in precipitation rates within ARs is observed in the UST and LML analysis subregions (Figure 3.12b-c).

We approached this study with the goal of leveraging an idealized model to investigate the sensitivity of AR statistics to isolated SST warming. In fact, the idealizations present in this experiment design provide a means to more clearly elucidate the underlying physical processes and explain the relevant theory. The analyses of AR IWV and precipitation described here provide physical context for results obtained in comprehensive climate models, where compensatory or compound effects can confound interpretation and leave open questions about the mechanistic relationships between forcings and impacts.

Acknowledgments

We wish to thank the editor and anonymous reviewers, whose input greatly improved this manuscript. Previous and current CESM versions are freely available online (at `http://www.cesm.ucar.edu/models/cesm2/`). TempestExtremes AR detection software are available for public use on GitHub (at `http://www.github.com/ClimateGlobalChange/tempestextremes`). Data used to generate figures for this manuscript, as well as model configuration and AR detection details, are archived at Zenodo (`http://doi.org/10.5281/zenodo.3912050`). This work has been supported by NASA award NNX16AG62G "TempestExtremes: Indicators of change in the characteristics of extreme weather" and Department of Energy Office of Science award number DE-SC0016605, "An Integrated Evaluation of the Simulated Hydroclimate System of the Continental US." This project is also supported by the National Institute of Food and Agriculture, U.S. Department of Agriculture, hatch project under California Agricultural Experiment Station project accession nos. 1010971 and 1016611. This research used resources of the National Energy Research Scientific Computing Center, a DOE Office of Science User Facility supported by the Office of Science of the U.S. Department of Energy under Contract No. DE-AC02-05CH11231.

Chapter 4

Response of Atmospheric River Width and Intensity to Sea-Surface Temperatures in an Aquaplanet Model

This is a slightly modified version of a manuscript submitted to *Journal of Geophysical Research: Atmospheres* that is under review as:

> **McClenny, E. E.** & Ullrich, P. A., (2020). "Response of Atmospheric River Width and Intensity to Sea-Surface Temperatures in an Aquaplanet Model". *Journal of Geophysical Research: Atmospheres*

Abstract

Transient corridors of enhanced integrated vapor transport (IVT) called atmospheric rivers (ARs) are crucial features of the global hydroclimate, but their response to climate change is still poorly understood. Since ARs are narrow [O(1000 km)] and the watershed features which they impact exist on a smaller scale [O(100 km)], width represents a critical AR characteristic. Previous research already suggests robust AR widening, even across a diverse set of AR detection tools (ARDTs) which define AR lateral boundaries. To remove the influence of the ARDT, this study takes a novel approach by defining AR impacts-relevant width (wi; conditioned on the critical threshold IVT > 250 kg m^{-1} s^{-1})

by modeling AR IVT profiles as idealized Gaussian curves with free parameters background IVT (IVT0), intensity above background (dIVT), and IVT profile breadth (wd; the width encompassing 95% of the total IVT) to determine the quantitative contributions of each factor. To minimize effects from regional topography, this study uses the aquaplanet configuration of the Community Atmosphere Model version 5, first with a Baseline sea-surface temperature (SST) distribution, then adding two, four, and six Kelvin over this Baseline. Quantitative analysis finds that AR wi expands by approximately 35 km per K SST warming, with the majority of this widening related to thermodynamically driven increases in IVT0. Separating this analysis along the AR spine reveals additional insights, that wi expansion is dominated by thermodynamics (dIVT and IVT0 increases) on the equatorward side and dynamics (wd) on the poleward side related to weakening wind gradients.

4.1 Introduction

In a seminal paper, Zhu and Newell (1998) partitioned snapshots of midlatitude moisture fluxes into those performed by weak "broad fluxes" and those performed by coherent filaments of enhanced vapor transport. This partitioning allowed them to determine that these narrow "atmospheric rivers" (ARs) accomplish virtually all of the meridional moisture flux through the midlatitudes despite occupying less than ten percent of the region's zonal circumference (Zhu and Newell, 1998). For one study day in particular, they estimated that in order to accomplish this, each AR must transport an average of $\sim 2.2 \times 10^8$ kg of water vapor per second through a cross-sectional width of less than 1000 km. Since then, larger studies have confirmed the magnitudes of both AR vapor transport and cross-sectional width: a dropsonde study of 21 ARs by Ralph et al. (2017), as well a reanalysis study by Guan et al. (2018) featuring a much larger sample size ($\sim$ 6000 ARs) found that each AR transports an average of $\sim 5 \times 10^8$ kg of water vapor per second through a cross-sectional width of $\sim$890 km (Ralph et al., 2017). Summing this vapor transport across the approximately three to five ARs typically present in each hemisphere indeed accounts for virtually all of the meridional moisture transport through

the midlatitudes (Ralph et al., 2017), revealing the crucial role these systems play in global water and energy transport despite their often delicate, filamentary morphology.

On land, this vapor transport through such a narrow region can add up to extreme impacts: since ARs are approximately moist-neutral through the lower troposphere (Ralph et al., 2017), their moisture does not resist orographic uplift, granting them the potential to be impressive and even destructive precipitation events (Neiman et al., 2002). For instance, an observational study by Ralph et al. (2006) found that all seven flooding events along California's Russian River in an eight-year period occurred during AR conditions characterized by heavy orographic precipitation. Likewise, Lavers et al. (2012) examined 31 years of flooding across nine basins in Great Britain, and attributed 40-80% of the events to persistent AR conditions. Aside from flooding, ARs still have an oversized impact compared to their modest widths: along the United States' west coast, landfalling ARs contribute $20 - 50\%$ of the total cool-season precipitation (Dettinger et al., 2011; Lavers and Villarini, 2015) and $30 - 40\%$ of the total mountain snowpack's snow-water equivalent (Guan et al., 2010). AR precipitation fraction is even larger on the South American west coast, where Viale et al. (2018) found that ARs contributed $40 - 60\%$ of annual precipitation totals from $2001 - 2016$. Meanwhile, the western European coast receives comparatively less (up to $20 - 30\%$) of its precipitation totals from ARs (Lavers and Villarini, 2015), but these fractional accumulations are impressive nonetheless. Taken together, ARs are credited with providing over one-fifth of water runoff globally (Paltan et al., 2017), once again cementing the role of these narrow systems role as dominant features of the global hydroclimate.

Since ARs have such clear importance to global water balance and regional water resources, their response to climate change will play a crucial role in the future hydroclimate (Payne et al., 2020). Still, their status as relatively newly identified systems—Zhu and Newell (1998) is credited as the first study to describe them as distinct features—has stymied large-scale, systematic studies of ARs under present-day or climate-change conditions. One specific issue was only very recently addressed: the American Meteorological Society (AMS) *Glossary of Meteorology* (*GoM*) first added an entry for ARs in 2017 af-

ter extensive inter-institutional effort to converge on an acceptable definition (see Ralph et al., 2018, for a summary of this process). This definition characterizes ARs as "long, narrow, and transient corridor[s] of strong horizontal water vapor transport...typically associated with a low-level jet stream ahead of the cold front of an extratropical cyclone," and notes that they are, on average, 850 km wide and 3 km deep (AMS, 2017). While the AR entry in the *GoM* provides researchers with a commonly accepted definition for these critical climate features, it intentionally leaves out quantitative guidance on identifying AR lateral boundaries in order to leave room for "future and specialized developments [in AR research]" (Ralph et al., 2018).

Returning to the studies cited earlier on AR vapor transport (e.g., Zhu and Newell, 1998) and overland impacts (e.g., Ralph et al., 2006) it should be clear that AR lateral boundary identification is necessary not only for attribution purposes, but in itself represents a critical AR statistic. ARs exist on a relatively fine scale in terms of their cross-sectional width and landfall location [$\mathcal{O}$(1000 km)], but the watersheds which they impact typically exist on an even finer one [$\mathcal{O}$(100 km)]. Hence the average 300 km AR landfall position error recorded at three-day lead times (Wick et al., 2013b; DeFlorio et al., 2018) represents a significant limitation for planning and preparedness. As a result, certain details of AR landfall—such as location, orientation with respect to topography, and the area of local AR impacts—are considered key observational gaps (Ralph et al., 2020); moreover, research on the response of these AR characteristics to surface warming can then lead to an important understanding of the underlying process drivers. To this end, oversea AR width statistics have been employed to provide some simplified yet intriguing insights: in the first global assessment of AR statistics under present-day and climate-change conditions, Espinoza et al. (2018) found that the number of individual ARs decreased by $\sim$10%, but AR length and width both increased by $\sim$25%, an effect which was robust across 21 models. Likewise, McClenny et al. (2020) found that increasing zonal mean AR occurrence frequency under uniform sea-surface temperature (SST) warming in an aquaplanet model was dominated by increasing AR zonal extent, a surprising result given the ARDT employed there is insensitive to additive changes in background IVT. In

any case, it showed the importance of AR area in understanding climate-driven changes in AR statistics.

Despite the qualitative agreement between Espinoza et al. (2018) and McClenny et al. (2020), substantial spread exists in AR climate change predictions as a function of AR detection tool (ARDT) choice: a comparison of AR statistics derived from several ARDTs across multiple models showed that while all ARDTs produced an increase in overall areal extent under climate-change conditions, the inter-ARDT variation of changes in AR count or size dominated the inter-model variation (O'Brien et al., 2020, *in preprint*). Given these results, we argue that an examination of AR width changes that is largely independent of ARDT will provide an important comparison against the existing inter-ARDT spread. We furthermore argue that simplified surface boundary conditions are useful for clarifying the mechanisms behind any AR width changes by allowing us to isolate the physical drivers (Held, 2005). To facilitate this, we examine ARs in a series of aquaplanet simulations featuring increasing uniform SST warming. We also define a series of AR widths not derived directly from ARDT-identified lateral boundaries. A novel aspect of this paper is the representation of AR cross-sections in integrated vapor transport (IVT; Equation 4.2.1) as Gaussian curves with free parameters *background IVT* ($IVT0$), *AR intensity above background* ($dIVT$), and *dynamic width* (wd), defined here as the lateral region through which ∼95% of the total vapor transport occurs (Equation 4.2.2). Notably, the definition for wd does not include any explicit numerical thresholds, in contrast to most ARDTs which feature either a relative (percentile-based) or absolute threshold (usually the region featuring IVT greater than 250 kg m^{-1} s^{-1}; see Shields et al., 2018, for a review). We then assume that this critical IVT threshold corresponds to the impacts-relevant region of the AR, and so define an AR *impact width* (wi) conditioned on it but derived with respect to the Gaussian approximations (Equation 4.2.4). In all, we use these Gaussian fits and the widths derived from them to answer the following questions:

(a) Are AR IVT cross-sections well-represented as simplified Gaussian functions?

(b) How do AR local background IVT ($IVT0$) and peak IVT intensity ($dIVT$) change as a result of uniform SST increases?

(c) How do different measures of AR width change under uniform SST increases?

(d) Finally, how much of the change in the impacts-relevant AR width can be attributed to changes in AR background IVT ($IVT0$), AR IVT intensity above the local background IVT ($dIVT$), and the overall broadening of AR IVT profiles (dynamic width; wd)?

Related to question (d), we also revisit a question left unanswered from McClenny et al. (2020)—namely, why does the TempestExtremes ARDT produce wider ARs under uniform SST increases, given its baked-in insensitivity to uniform increases in the IVT field?

For reference, Figure 4.1 shows a series of idealized AR IVT cross-sections as Gaussian curves. These curves correspond to a baseline Gaussian curve as well as various transformations of this baseline curve as a result of isolated increases in each variable. In all cases, the lateral boundaries corresponding to $IVT = 250$ kg m^{-1} s^{-1} indeed widen, but there are important distinctions to be made between each resulting IVT profile: specifically, an isolated increase to wd results in an overall broader IVT field, while rising $IVT0$ corresponds to a uniform upward shift in the IVT field, and enhanced $dIVT$ describes an AR cross-section which elongates along the y axis without changes in the background IVT field (that is, $IVT0$).

We present this paper as follows: first, Section 4.2 describes our experimental procedures, including details on the ARDT, all measures of AR width, and the curve-fitting procedures, then ends with a brief description of the model setup. After this, Section 4.3 starts with a summary of bulk AR cross-sections, then a validation of Gaussian fits compared to AR IVT profiles. We then examine AR cross-section statistics for each SST scenario, and quantitatively examine the contributions of $IVT0$, $dIVT$, and wd to changes in AR impact width. Finally, Section 4.4 presents conclusions from this analysis.

4.2 Methods

In order to investigate AR width and changes therein resulting from SST warming, we must first define the lateral boundaries of ARs. To that end, we begin this section by defin-

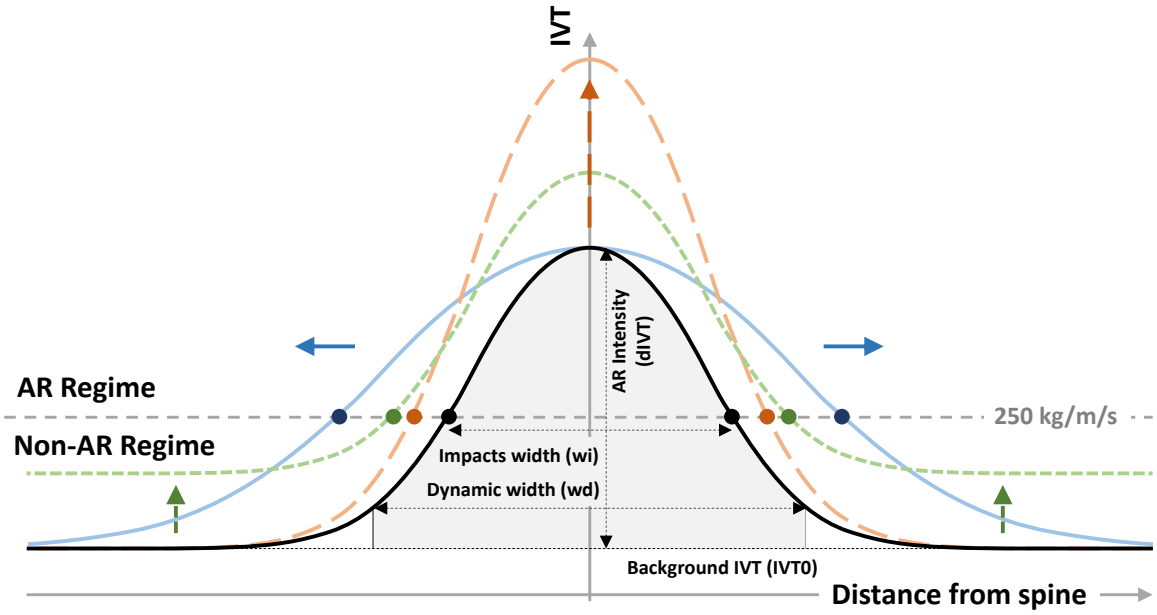

Figure 4.1: A depiction of an idealized AR IVT cross-section (black curve) as a Gaussian curve characterized by the background IVT ($IVT0$), intensity above background ($dIVT$), and dynamic width (wd). The impact width (wi) then refers to the cross-sectional width of the region where IVT exceeds 250 kg m^{-1} s^{-1}. Changes to the impact width can be due to changes in the background IVT (short dashed green curve), changes in the intensity above background (long dashed red curve), or changes in the dynamic width (blue curve).

ing terms used throughout the manuscript, as well as summarizing the AR identification and cross-section generation procedures used here. We follow this with a discussion of the concept of AR cross-sections as Gaussian curves in the local IVT field, a characterization from which we can extract key information, including a novel estimate of AR width. We then move on to describe several other distinct AR width measurements employed here, each of which enriches our understanding in a unique way. After this, we provide details on the curve-fitting procedure, then conclude with a brief description of the model setup.

4.2.1 Definitions

A depiction of the terminology employed in this paper is given in Figure 4.2. IVT is computed as

$$IVT = \sqrt{\left(-\frac{1}{g}\int_{p_0}^{p_T} qudp \right)^2 + \left(-\frac{1}{g}\int_{p_0}^{p_T} qvdp \right)^2} \tag{4.2.1}$$

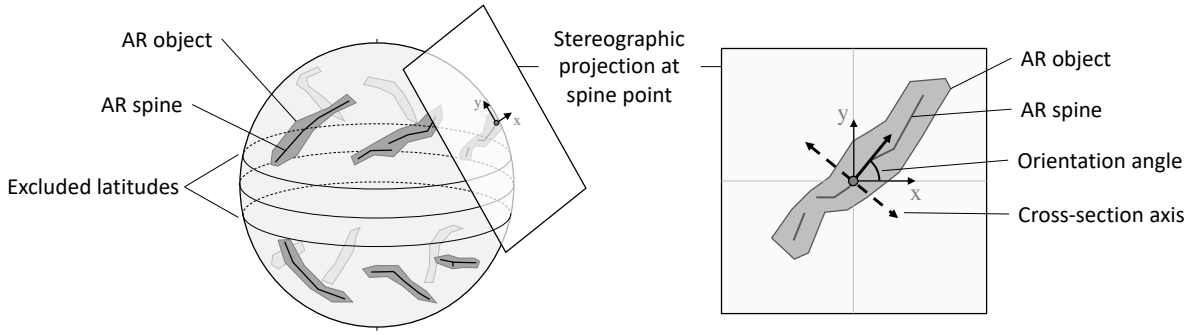

Figure 4.2: A depiction of the terminology used to describe the output of the TempestExtremes ARDT.

where $p_0 = 1000$ hPa, $p_T = 300$ hPa, g is gravitational acceleration, q is water vapor mixing ratio, and u and v are the zonal and meridional wind velocities, respectively.

Grid points are considered part of an atmospheric river object if they satisfy the TempestExtremes (TE) criteria for ARs. Briefly, TE computes the Laplacian of IVT (L^2IVT) at each grid point using an eight-point stencil (each cardinal and intercardinal direction) with a radius of ~ 800 km. It then identifies contiguous areas of at least 50 adjacent grid points (an area of approximately 125,000km^2) with $L^2\text{IVT} < -40000$ kg m^{-1} s^{-1} rad^{-2}. These criteria are motivated by the observation that a large negative Laplacian of IVT corresponds to points in an IVT profile that are strongly curved downward—namely, one should expect that long, narrow filaments of IVT should have a large negative Laplacian. The area criteria is then employed to remove isolated peaks in the IVT field. Note that these criteria are only employed in this study to downselect AR points that would be subsequently used for identifying the AR spine; since the spine of the AR is generally expected to pass through the AR core—a feature which is detected by essentially all ARDTs (Shields et al., 2018; Rutz et al., 2019)—we argue that our results will be largely independent of ARDT.

Once the footprint of the AR is identified, points are then considered part of the *AR spine* if they are tagged as AR points and have the largest IVT value within five degrees in either the zonal or meridional direction (Figure 4.3a shows an example AR object with spine). The orientation of the AR object is defined at each spine point locally via

stereographic projection of the spine point and its contiguous neighbors, followed by linear regression through spine points. The cross-section is then defined at each spine point as a straight line in the stereographic projection through the origin, which corresponds to a great circle arc perpendicular to the direction of AR orientation (Figure 4.2). Each AR cross-section features the AR spine at the midpoint with 15 equally spaced points on each end ($\Delta x \approx 55.59$ km) to capture sufficient background IVT. Figure 4.3b shows an example AR and its IVT cross-section.

Since we find that TE's AR detection criteria tends to misclassify tropical cyclones (TCs) and tropical easterly waves as AR objects, we exclude any points equatorward of 20° N/S, and furthermore apply a separate TC-detection utility also available from TE. To summarize, TE identifies a TC as all points within an 8.0° GCD radius of the most intense local sea-level pressure (SLP) minimum in a 2.0° GCD (a) whose SLP increases by at least 375 Pa over a 3.6° radius and (b) whose 300 minus 500 hPa geopotential height thickness decreases by six meters over 7.5° to detect warm-core storms. For more details on TC detection, we refer readers to Ullrich and Zarzycki (2017) and Zarzycki and Ullrich (2017).

4.2.2 Gaussian approximation to IVT

The cross-sectional IVT profile for each atmospheric river is approximated via a Gaussian profile,

$$IVT(\Delta\sigma) = IVT0 + dIVT \exp\left[-\frac{8\Delta\sigma^2}{wd^2}\right], \tag{4.2.2}$$

where $\Delta\sigma$ denotes the signed GCD (positive equatorward) from the peak of the AR IVT distribution, $IVT0$ is the background IVT, $dIVT$ is the intensity of the AR above the background, and wd is herein referred to as the *dynamic width*. The form of this profile is defined so that $\approx 95\%$ of the AR IVT above the background state occurs within the band $\Delta\sigma \in [-wd/2, wd/2]$, namely

$$\frac{\int_{-wd/2}^{wd/2} IVT(x)dx}{\int_{-\infty}^{\infty} IVT(x)dx} = \mathsf{erf}(\sqrt{2}) \approx 95\%. \tag{4.2.3}$$

We calculate the free parameters of each AR by fitting Equation 4.2.2 to AR cross-sections normalized by spine IVT to ensure a consistent range of values across samples. We accomplish this using software provided under the Scientific Python package (Section 4.2.4 provides further details on the curve-fitting procedure).

Some additional complexity is introduced by the asymmetry of ARs (e.g., Figure 4.5). While this is certainly related to the latitude-dependence of background moisture and wind fields, it is compounded further by the cold frontal region typically present on the poleward side of ARs (Ralph et al., 2004a; Cordeira et al., 2013; Ralph et al., 2017). To flexibly account for this asymmetry, we compute all widths in piece-wise fashion from the poleward and equatorward sides of each IVT cross-section. Hence, $wd = wd_p + wd_e$, where wd_p and wd_e are the poleward and equatorward dynamic widths, respectively. This allows us to have unequal half-widths on each side of the spine and prevents over- or under-estimation of AR wd as a result of lateral asymmetry. Note that, hereafter, the term "Gaussian" refers to a piece-wise Gaussian separated at the spine, as described. Figure 4.3 illustrates the utility of our piece-wise fit, since imposing a symmetric Gaussian here would result in an overestimation of AR wd on the equatorward side, and an underestimation on the poleward side. While this shows that AR IVT cross-sections are not captured as Gaussian curves but as piece-wise Gaussians, we can nevertheless use the derived fitting parameters to assess AR cross-sections.

4.2.3 Other measures of AR width

While the definition of AR dynamic width (hereafter wd) provides a measure of AR lateral boundaries that isolates the AR's anomaly with respect to the local background IVT field, we nevertheless define a series of other AR widths for comparison, which we describe below.

Algorithmic width (wa): We initially detect our sample of ARs with the TE algorithm, but only as a starting point for further analysis. Nonetheless, we include the lateral boundary measurements garnered from the criteria described in Section 4.2.1 to evaluate its sensitivity to background climatology with respect to wd. Put more explicitly, wa characterizes AR width as all points across a detected object featuring

$L^2\text{IVT} < -40000$ kg m^{-1} s^{-1} rad^{-2} over a radius of approximately 800 km. We do not interpolate these values but preserve their underlying grid, making this is the only discrete measurement of AR width employed here. Notably since TE is primarily designed to detect the most intense parts of the AR (the AR core), the algorithmic width tends to be much smaller than the other width measures (as later seen in Figure 4.7).

Literature width (wl): The *GoM* defines AR lateral boundaries with a threshold of $IVT \geq 250$ kg m^{-1} s^{-1} (AMS, 2017). We thus include a width computation based around this threshold by finding the first point on each side of the AR spine which drops below this value via linear interpolation to avoid under- or over-estimates associated with IVT gradients on a relatively coarse grid. This measure exists to provide a reference point for AR width as measured via this common threshold (e.g. Shields et al., 2018).

Impact width (wi): Finally, since $IVT \geq 250$ kg m^{-1} s^{-1} is often considered important for assessing AR impacts, we obtain a width which achieves this value from Equation 4.2.2 as:

$$wi = wd\sqrt{-\frac{1}{8}\ln\left[\frac{IVT_{ref} - IVT0}{dIVT}\right]}. \tag{4.2.4}$$

where $IVT_{ref} = 250$ kg m^{-1} s^{-1}. This equation is obtained by solving (4.2.2) for $IVT(\Delta\sigma) = 250$ kg m^{-1} s^{-1}.

Importantly, wi is equivalent to wl for ARs that are perfectly Gaussian; as such, the difference between these two measurements is an alternative metric for computing AR and its best-fit Gaussian. While ARs are not perfectly Gaussian, the definition of wi here nevertheless has the advantage of determining AR lateral boundaries using an impacts-relevant threshold, but with the additional benefit of being described by a known function with variables wd, $IVT0$, and $dIVT$. Hence we use wi not only to estimate impacts-relevant changes to AR width, but also to isolate how these variables drive changes in AR wi under warming SST conditions.

4.2.4 Curve-fitting and software details

We fit Gaussian curves (Section 4.2.2) to AR IVT cross-sections with the Scientific Python (SciPy) optimization package, which uses least squares to optimize the free parameters

of a function to best fit the data (Virtanen et al., 2020). The Gaussian is assumed to be centered at the centroid of each AR object in order to minimize computation and avoid over- or under-representation of objects as a result of their length. AR centroids are found by the image processing package scikit-image (Walt et al., 2014), which accepts both a binary object image as well as an "intensity image" to produce weighted statistics. Accordingly, a field of cosine-latitude-weighted IVT is fed to scikit-image alongside the binary AR object data to ensure that the centroid is weighted by AR intensity rather than binary footprint. In the event that the weighted centroid does not correspond to an AR spine point, we find the closest spine point in terms of great circle distance (GCD) and take our sample from there.

We take cross-sections over a total GCD length of 3200 km to capture the AR background, but note this may introduce inconsistencies associated with peripheral points. To minimize the influence of the AR periphery when fitting a Gaussian curve, we introduce a simple weighting function which describes the relative uncertainty (α) of AR IVT cross-sections as a function of GCD from the AR spine ($\Delta\sigma$):

$$\alpha = 1 + \sqrt{|\Delta\sigma|} \tag{4.2.5}$$

This function describes increasing error (decreasing confidence) as distance from the spine increases. A number of such functions were evaluated, with this one eventually chosen because it seemed to produce better agreement along the AR spine and its immediate periphery, where this study focuses. While subjectively determined, this weighting function has the advantage of applying the most confidence to IVT in the AR spine, while the rapidly decreasing confidence about it helps in isolating ARs from a frequently noisy background. We use a similar weighting when evaluating the performance of our Gaussian fits with respect to the AR cross-sectional IVT via a weighted root-mean-squared error (RMSE) calculation in order to maintain consistency with our weighted curve fits. For reference, Figure 4.3 shows an example AR exhibiting a near-Gaussian IVT profile in terms of RMSE, while Figures B.1-B.3 show ARs featuring higher RMSE values included

in this analysis. The weighting function for the RMSE goes as follows:

$$\beta = \sigma - \sqrt{|\Delta\sigma|} \tag{4.2.6}$$

where σ is the location of the AR spine. In a qualitative sense, this function acts as the inverse of α in that it describes rapidly decreasing weight (that is, confidence) as distance from the spine increases.

4.2.5 Model setup

The model setup used here is identical to that used for a previous analysis of ARs (McClenny et al., 2020), so we provide only a brief summary here. We use the Community Earth System Model version 2 (CESM2) with Community Atmosphere Model version 5 (CAM5) physics (Neale et al., 2010) and a spectral element dynamical core with NE60 resolution under an aquaplanet (AQP) configuration. The AQP has no land, sea ice, topography, or axial tilt (i.e., perpetual equinox conditions), and features a single-layer "data ocean" which thermally forces the atmosphere with a fixed SST. We prescribe this SST as an analytic function in latitude; specifically, we use the "QOBS" profile from Neale and Hoskins (2000), while the warming scenarios feature globally uniform SST increases of two, four, and six K, respectively. Other than these SST changes, we retain default CAM5 values. We remap model output to a uniform 0.5° finite volume grid using the TempestRemap software suite (Ullrich and Taylor, 2015; Ullrich et al., 2016) before computing derived variables, detecting ARs, or performing analyses.

We recognize our use of an AQP configuration makes it impossible to directly evaluate changes in landfall statistics (although they could still be ascertained indirectly), but we argue that the idealizations provide benefits well worth the trade-off. First, the zonal uniformity of SST as well as the lack of seasonality eliminates variability in surface boundary conditions, allowing for a relatively small sample size of ARs to have sufficiently small confidence bounds. Meanwhile, the AQP's atmosphere rapidly responds to the prescribed SST, such that we only remove the first month of each integration for spin-up. Last, the SST symmetry about the equator allows us to effectively double our sample size, to the extent that the northern and southern hemispheres can be considered independent from

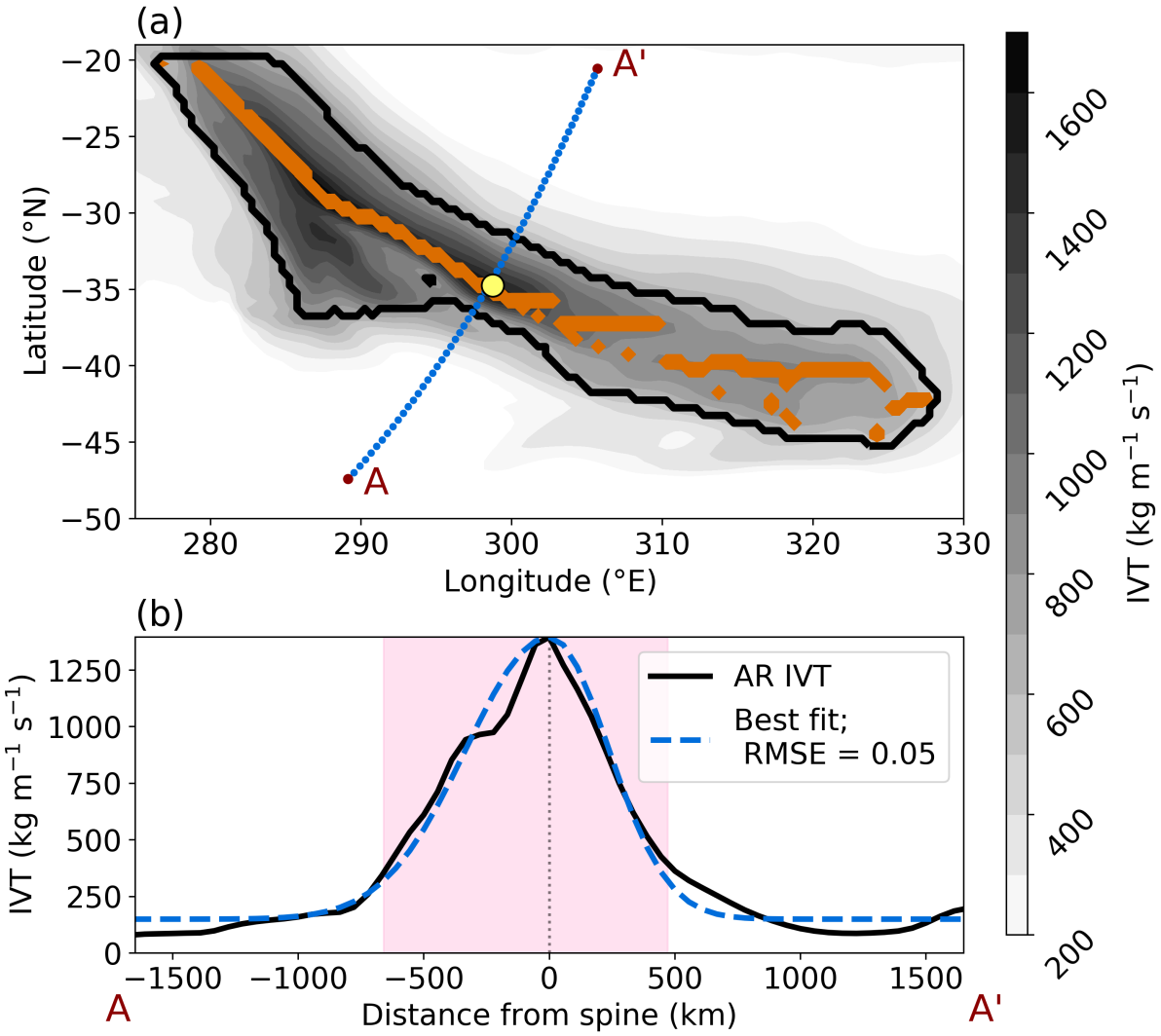

Figure 4.3: Example of a near-Gaussian AR in terms of RMSE. (a) IVT field (grayscale contours). Shown also are the AR boundaries (thick, black outline), spine (thick, orange lines), and cross-section points (blue, dotted line; bounded by points A and A') as detected by TE, as well as the mass-weighted AR centroid determined by scikit-image. (b) Cross-section in IVT from A to A' (black, solid curve) and the best-fit piece-wise Gaussian (blue, dashed curve). Pink shading shows wd, while the dotted line shows the spine location to clarify the asymmetry.

one another. Taken together, this essentially leaves us with a 60-month sample size from a 31-month total integration; we break this total up into a series of 90-day samples which we consider analogous to a 20-season ensemble.

4.3 Results

We begin our analysis by assessing the AR centroid cross-sections obtained by TE. After this, we describe changes in each measure of AR width, and examine the contributions of background IVT ($IVT0$) and AR intensity ($dIVT$) to AR spine IVT values. We wrap this section up with a quantitative analysis of the drivers of AR impact width.

4.3.1 AR cross-sections

Since we only use TE as a first-pass method for identifying ridges in the AR field, we follow up our ARDT results with additional filtering before running any statistics. Specifically, we remove an AR centroid cross-section if it meets any of the following criteria:

(a) Its maximum IVT does not exist at the midpoint of the cross-section, which occurs when two parallel spines exist in a single cross-section.

(b) An AR grid point (as identified by TE) exists at its periphery (defined here as $\sim$ last 250 km on each side). We remove these since we only wish to consider isolated events.

(c) It contains a TC grid point.

(d) Its RMSE with respect to the best-fit Gaussian (Equation 4.2.2) is 0.2 or greater.

(e) *For the impact width analysis only:* Its $IVT0 \geq 250$ kg m^{-1} s^{-1}, since this makes it impossible to evaluate wi (Equation 4.2.4).

Table 4.1 summarizes the results of these refinements. In all, we keep the majority of AR centroids, with the greatest losses usually related to double-spine AR objects (that is, objects whose maximum IVT occurs at some location other than the spine). Note that this criterion is imposed to prevent double-counting of these double-spine objects, since

the same object can be retained for analysis once the spine point does correspond to the maximum cross-sectional IVT.

	+0K	+2K	+4K	+6K
Total cross-sections	5706.6 (180.5)	6059.35 (168.1)	6716.2 (245.9)	7202.25 (340.3)
Total analyzed	4756.2 (146.4)	4940.3 (119.3)	5148.45 (162.5)	5241.45 (194.5)
Impacts subset	4578.4 (129.1)	4506.15 (114.6)	4376.85 (211.3)	3943.7 (291.1)
Total thrown out	950.4 (96.3)	1119.05 (98.6)	1567.75 (135.6)	1960.8 (166.2)
Double spine	760.6 (79.4)	907.55 (75.0)	1288.2 (117.3)	1594.4 (119.2)
Periphery AR points	70.2 (14.9)	109.65 (24.6)	173.55 (26.7)	237.35 (40.3)
TC points	74.15 (33.9)	39.25 (23.4)	26.5 (18.4)	22.0 (14.4)
Weighted RMSE 0.2+	45.45 (10.9)	62.6 (10.9)	79.5 (10.0)	107.05 (15.1)
IVT0 > 250*	177.8 (60.7)	434.15 (81.1)	771.6 (129.0)	1297.75 (136.2)

Table 4.1: Mean (standard deviation) AR centroid cross-section counts for each SST run with respect to the 90-day ensembles. The first three rows show the number of AR centroid cross-sections detected by TE, the number kept for the *wd, wa* and *wl* analyses, and the number kept for the *wi* analysis, respectively. The following rows show the count of AR centroid cross-sections removed from analysis for each criterion.

Figure 4.4 shows composite AR centroid cross-sections (hereafter simply AR cross-sections) for each SST run. The cross-sections here feature a narrow region ($\sim$ 1000 km) of specific humidity (q) enhancement which extends into the mid-troposphere. Notably, this narrow region of enhancement tilts towards the poleward flank due to deformation along the accompanying frontal zone (Cordeira et al., 2013; Ralph et al., 2004a). Also along the poleward flank of the AR composite there exists the upper-level jet which provides the steering flow for these systems. In all, the composite cross-section for the Baseline run (ostensibly the run whose SSTs are closest to present-day observations) corresponds nicely to results obtained via dropsonde analyses by Ralph et al. (2017). Meanwhile, the composites for the test runs show a q enhancement which is consistent with basic thermodynamics, and a slight slowing in the upper-level jet.

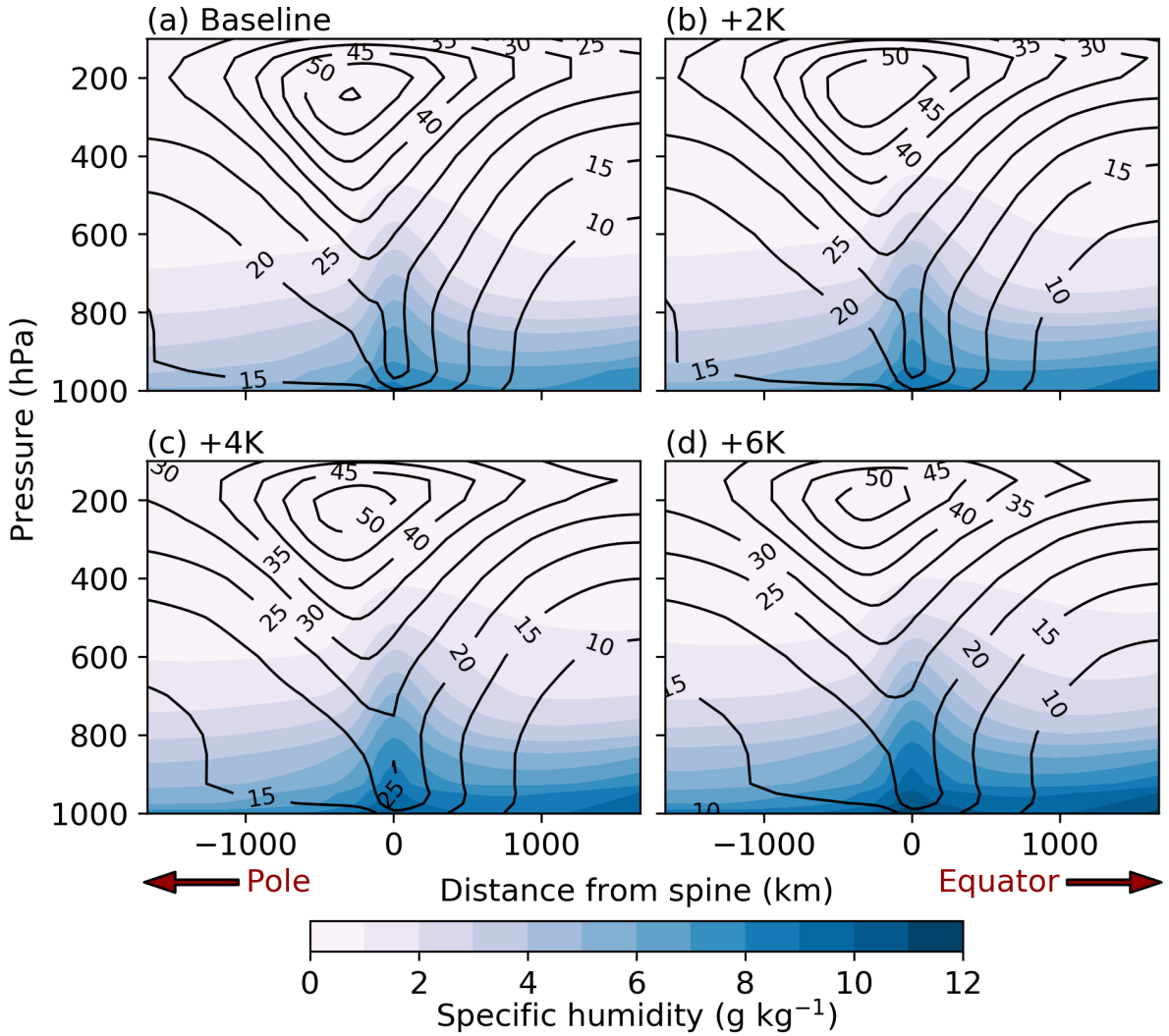

Figure 4.4: Composites of AR centroid cross-sections for each SST run. Shading shows specific humidity (q; g/kg) while unfilled contours show wind speed (m/s). Plots are oriented such that higher latitudes are to the left.

4.3.2 AR Gaussian fits

We next evaluate the ability of Gaussian curves to sufficiently capture cross-sections of AR IVT. Qualitatively speaking, most AR IVT cross-sections appear to generally follow a skewed Gaussian shape, though there are inconsistencies worth noting (Figure 4.5). In general, the best-fit curves tend to systematically underestimate IVT at the AR edges (i.e., at wi and wd). The effect is slight and is likely related to the weighting function, α (Equation 4.2.5), which results in $IVT \geq 250$ kg m^{-1} s^{-1} at wi on each side of the spine (Figure 4.5), and possibly slight underestimations of wd and wi (we discuss this more in Section 4.3.4). Additionally, while we allowed for the piece-wise fit to produce unequal half-widths on each side of the AR spine, we did not provide such flexibility for $IVT0$ since we wanted a single number which corresponds to a mean background IVT. As a result, $IVT0$ tends to be slightly overestimated on the equatorward side and underestimated on the poleward side (Figure 4.5).

High-IVT points ($IVT > 0.5$ *spine IVT*) towards AR peripheries are potentially problematic, since we desired a sample of ARs which are not closely interacting with other high-IVT objects. In some cases, these points could belong to the same AR object; as an example, Figure 4.3 shows an AR with a short filament of high IVT branching off to the southwest of the main spine. Other explanations could be any number of phenomena known to interact closely with ARs, including extratropical cyclones (Dacre et al., 2015; Eiras-Barca et al., 2018), mesoscale frontal waves (Neiman et al., 2016; Martin et al., 2019), or even other ARs with which they might be merging (e.g., Guan and Waliser, 2019). When it comes to the last possibility, we emphasize that while our removal of "double spine" objects might prevent these in many cases, it can only do so in the event that TE detects two distinct spines. Last, since we explicitly remove samples which feature TC grid points, we do not expect they account for a substantive proportion of high-IVT periphery points.

In any case, high-IVT points at the cross-section peripheries illustrate the utility of the "uncertainty function" (α) used for optimizing fits (Equation 4.2.5). Since α rapidly increases from the center point, the curve-fitting software places the most confidence in the

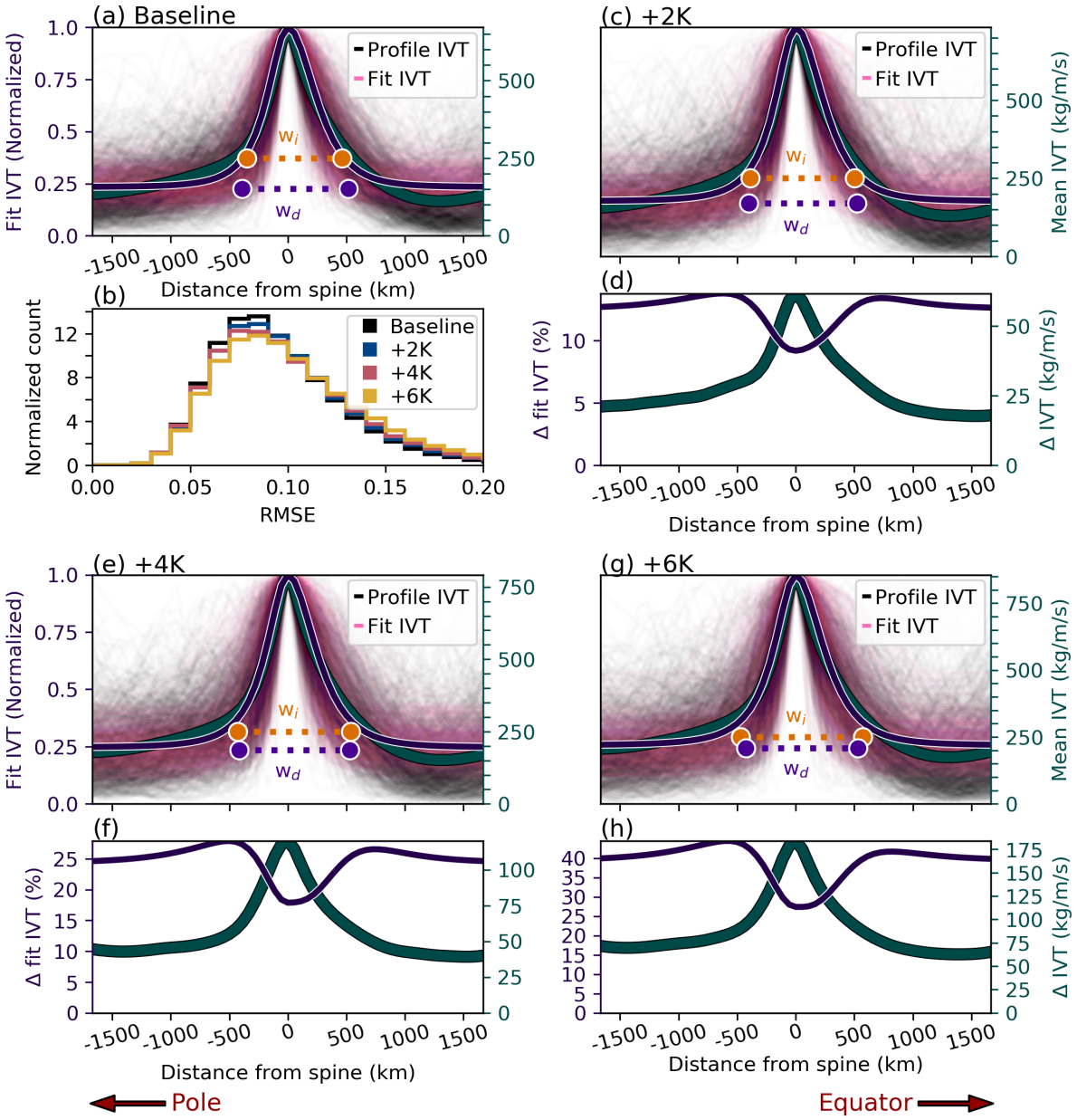

Figure 4.5: (a, c, e, g) AR cross-sections and Gaussian fits for each SST run. (Left y axis) Thin black lines show a randomly selected subsample ($N = 1000$) of AR IVT cross-sections, while thin pink lines show the corresponding best-fit Gaussians (all normalized by AR spine IVT for clarity and ease of plotting). (Right y axis) Thick, teal curves show mean AR IVT profile, while dark purple curves show the mean Gaussian estimate of AR IVT. Purple dotted lines and arrows show mean wd at $IVT =$ mean $IVT0$ for reference; meanwhile, corresponding orange annotations show mean wi at $IVT = 250$ kg m^{-1} s^{-1}, the reference value used here to determine impacts-relevant AR IVT. We show wd and wi here for reference only, and reserve discussion of them for Section 4.3.4. *Caption continues on the next page.*

Continued from previous page. (b) Histograms of weighted RMSE for each run, normalized by the total number of observations; note that these show the total sample, not just the 1000 random fits used for the cross-sections. (d, f, h) (Left y axis) The thinner purple curve shows the relative change of idealized Gaussian AR IVT, while the thicker teal curve shows the absolute change in the mean AR IVT profile (right y axis). These are shown here to clarify differences between plots a, c, e, and g, and will be discussed in later sections.

AR spine and the narrow region about it. This allows us to reliably isolate the AR without attempting to fit to these periphery points, which tended to result in broad Gaussians with unrealistically large widths not characteristic of ARs. Likewise, the weighting function for computing RMSE (Equation 4.2.6) is used here to ensure that these points along the periphery are not weighted as much as errors around the spine, where we are most confident that our IVT measurements correspond to the AR. Hence, RMSEs overall are quite low despite our relative exclusion of peripheral IVT points while optimizing fits, though steady rightward shifts in their distributions suggest nevertheless that Gaussian fits increasingly struggle to capture intra-AR IVT variance under warming conditions (Figure 4.5). Nonetheless, we can conclude that Gaussians are effective at capturing the general shape of the AR IVT distribution away from the periphery with few free parameters.

4.3.3 AR intensity

Now that we have examined AR IVT cross-sections and validated their respective best-fit Gaussian curves, we assess the IVT statistics derived from them. The response of aquaplanet AR IVT to uniform SST increases has been examined closely already (McClenny et al., 2020), but the recent addition of the cross-section generation functionality in TE now allows us to examine AR IVT in more detail. Namely, since the Gaussian IVT profile (Equation 4.2.2) includes $IVT0$ and $dIVT$ as fitting parameters, we can explicitly evaluate changes in AR spine IVT independently from changes in the AR's immediate background IVT. We find that while the means and medians of all three relevant IVT parameters increase roughly linearly with SST, this increase is mostly facilitated by changes at the highest IVT quantiles (75th and above), where IVT enhancement is largest (Figure

4.6; Tables B.1-B.3 compare relative changes in IVT parameters at multiple quantiles). That is, warmer sea-surface temperatures produce a greater spread in the intensity of ARs primarily through enhancement of the most extreme ARs.

We additionally find that each IVT parameter experiences conspicuously different relative changes: specifically, the relative enhancement in $IVT0$ outpaces that in $dIVT$, while the enhancement in spine IVT is consistent with its much larger contribution from $dIVT$. These results are shown by the relative changes in the AR Gaussian IVT fits (Figure 4.5f, d, h), which show a clear trough in ΔIVT at the AR spine and peaks at the inflection points. We note that this effect is especially pronounced on the poleward side of ARs and is attributed to thermodynamic effects; we reserve discussion of this for Section 4.3.5 where we carefully examine AR statistics on each side of the AR spine. In any case, the overall finding that background IVT increases outpace those in AR spine IVT are reflected in previous results: McClenny et al. (2020) found that IVT enhancement was overall larger in non-AR grid points than in those belonging to ARs, which was attributed to differing column responses in temperature and relative humidity between AR and non-AR grid points. While the AR and non-AR points in McClenny et al. (2020) do not strictly correspond to AR periphery and spine points, respectively, this qualitative consistency is nonetheless reassuring.

4.3.4 AR width

The overall IVT enhancement along the entire AR profile already implies AR widening for the Gaussian AR IVT model we use here (Figure 4.1); in fact we find that all width measures described in Section 4.2.3 systematically increase as SSTs warm (Figure 4.7), though clear differences exist from one width to another. We begin here by detailing results for the *literature width* (wl), since it acts as a direct comparison to a dropsonde study performed by Ralph et al. (2017) and so can be contextualized within the existing literature. Ralph et al. (2017) defined AR lateral boundaries as all points along a transect featuring $IVT \geq 250$ kg m^{-1} s^{-1} and found a mean width of 890 ± 270 km. Insofar as the Baseline SST scenario can be considered a proxy for present-day conditions, our finding that mean wl ($\overline{wl}$) = 982 km is inflated but not unreasonable. By comparison, we defined

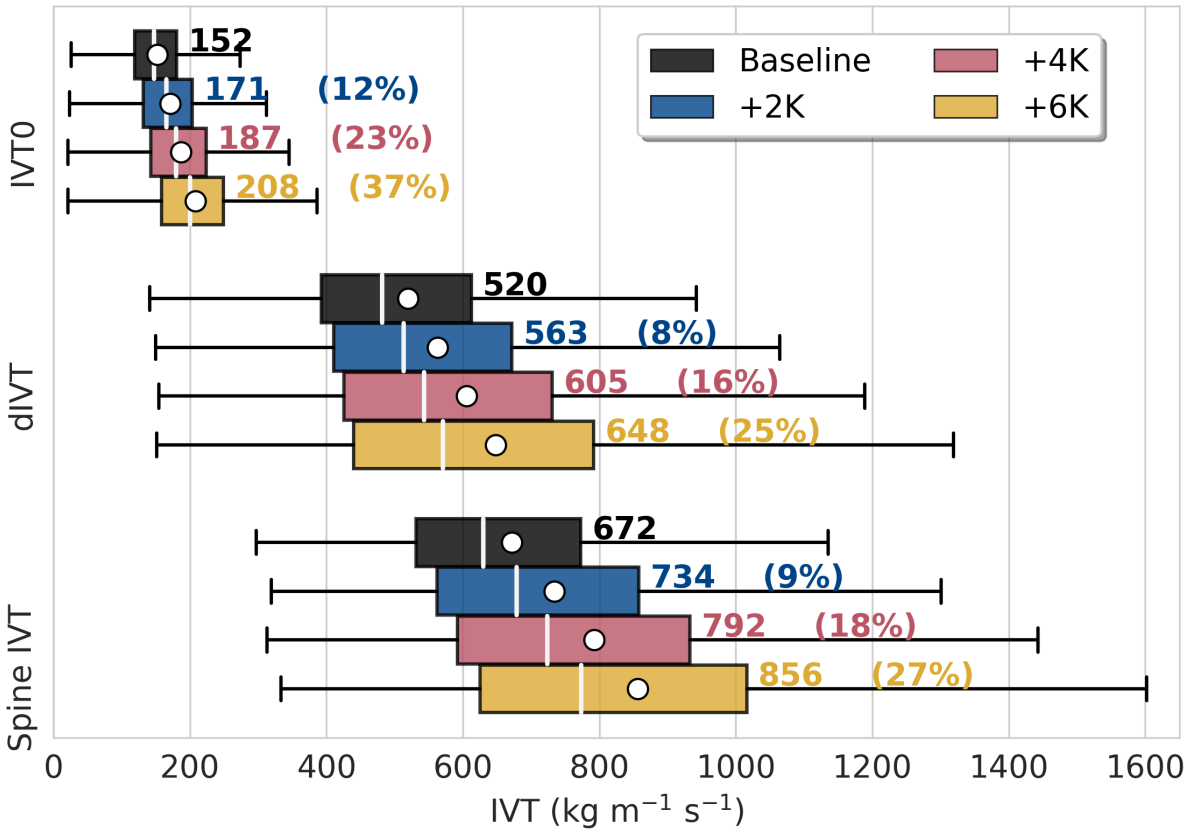

Figure 4.6: Box-and-whisker plots of AR IVT fit parameters ($IVT0$, $dIVT$) and spine IVT ($IVT0 + dIVT$; shown here for reference) for each SST run (kg m^{-1} s^{-1}). Means are shown both by white circles and as annotations. Parenthetical annotations show the relative change with respect to the Baseline mean for each test run.

wi to use the same critical threshold of IVT as wl but conditioned instead on the best-fit Gaussian curves. Thus the result here that $\overline{wi} = 812$ km is reasonable with respect to Ralph et al. (2017), but appears conspicuously underestimated when compared to $\overline{wl}$. This is related to a systematic underestimation of Gaussian IVT at approximately ±500 km of the AR spine (Figure 4.5). As a result, wd is slightly underestimated, though it could be improved with a more complicated fitting function. Still, the finding here that Baseline $\overline{wd} = 906$ km is well within reason, and it is notable that the Baseline distributions for wd and wi are qualitatively consistent with a distribution of reanalysis AR widths (Guan et al., 2018, see their Figure 4c): all feature a strong leftward skew with a mode under 1000 km and a long tail extending past 2000 km.

Since Guan et al. (2018) defined width with respect to the AR bounds as found by

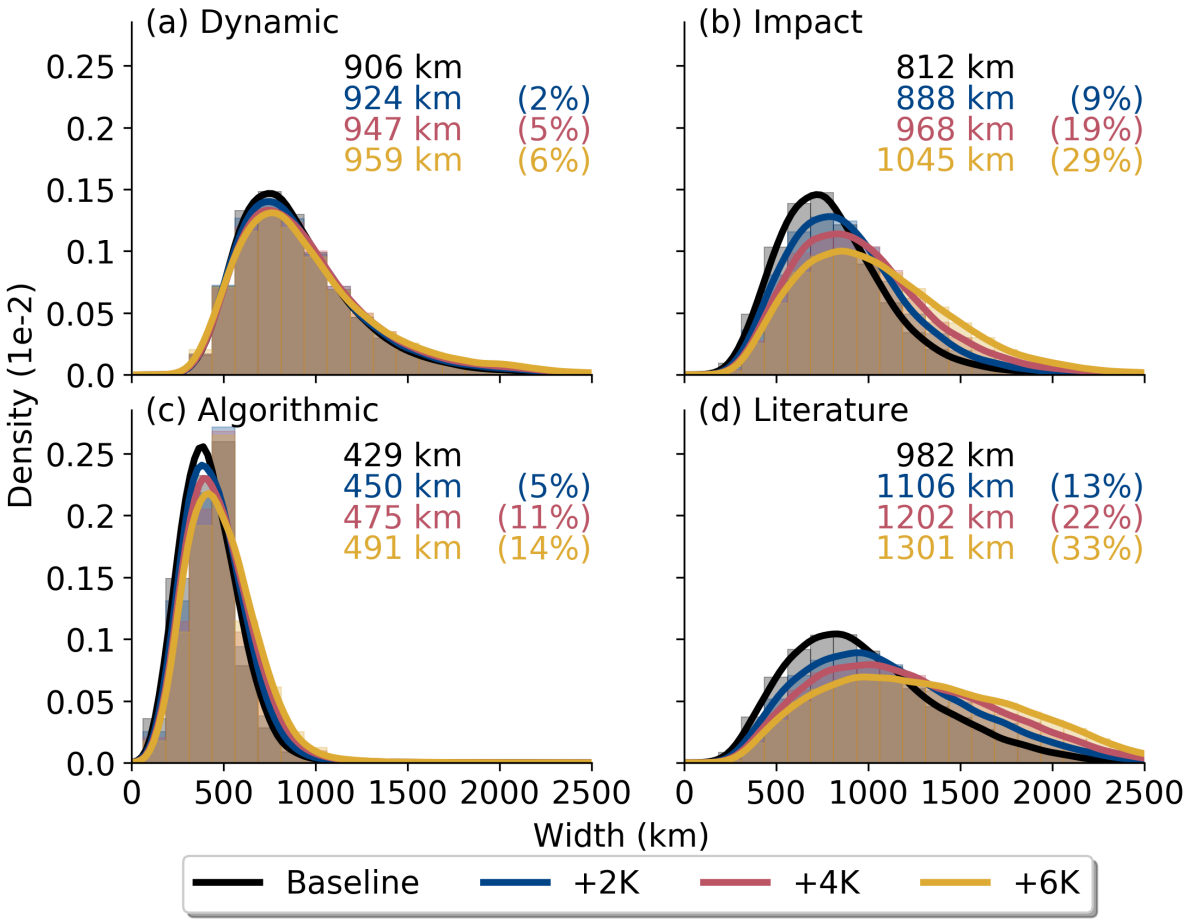

Figure 4.7: Distributions of AR width by method. Curves show kernel density estimates while shading shows the underlying histograms (bin spacing = 125 km). Annotations show the mean width in km for each run, while values in parentheses show the change with respect to the Baseline run expressed as a percentage.

their ARDT, our results for algorithmic width (wa) in particular highlight some of the differences across ARDTs. Specifically, while Guan et al. (2018) found a mean AR centroid width of approximately 850 km, we find here that $\overline{wa}$ = 429 km, indicative of what has been pointed out in the past—that tuning TE with the parameters described in Section 4.2.1 tends to identify the highest-IVT points immediately surrounding the AR spine. In other words, the finding here that TE produces substantially different wa results than other algorithms matches expectations, since the criteria employed here find the AR core rather than the entire AR object.

Given the disparate definitions of the AR widths explored here, we find it most illus-

trative to discuss changes in relative rather than absolute terms. To that end, Figure 4.7 shows the mean AR widths for each run, as well as their fractional changes with respect to the Baseline values. We find that mean AR width increases nearly linearly with SST warming for all definitions studied here, though there exist marked differences in terms of the magnitude of this slope. Namely, wd experiences the most subtle enhancement (approximately one percent per K SST warming), while wl expands at about six times this rate. The sensitivity of wl to SST is unsurprising given that it relies on an absolute IVT threshold which remains static regardless of changes to background IVT. Hence the finding that mean wl increases at approximately the same rate as mean $IVT0$ here (Figure 4.6) is reassuring in terms of internal consistency, but also illustrates the care with which researchers should assess AR climate change statistics derived from ARDTs which rely on absolute IVT thresholds (this point has already been discussed in Rutz et al., 2019). By contrast, the relatively modest enhancement in wa of $2-3$ percent per K reveals that the TE ARDT is relatively insensitive to changes in background IVT as facilitated by its use of the Laplacian to identify ridges in the IVT field. Nonetheless, since wa increases more than wd, this indicates that $IVT0$ and/or $dIVT$ statistics are relevant to TE (Section 4.3.6 elaborates on this further and shows that $dIVT$ changes largely account for this). Since wi relies on the same critical threshold of IVT as wl, its expansion at approximately the same rate as wl is reassuringly consistent. As far as why wi is systematically smaller than wl despite this similarity, we attribute this mostly to the idealized Gaussian IVT fits being imperfect representations of the actual AR profile; from Figure 4.5 it is clear that these fits tend to slightly underestimate the mean IVT profile at the inflection points. Nonetheless, this result does not affect our conclusions, and certainly some of this shift can be attributed to the Gaussian fits representing an AR isolated from surrounding objects whose IVT can easily exceed this threshold (e.g., ETCs, other ARs) which would spuriously inflate wl values.

4.3.5 AR skew

To deepen our understanding of the mechanisms behind the apparent AR widening, we begin by assessing how symmetric this widening is with respect to the AR spine. Since

we define each AR width as a linear combination of half-widths calculated separately on each side of the AR spine, we define a skew parameter, s, as:

$$s = \ln\left(\frac{w_e}{w_p}\right) \tag{4.3.1}$$

where ln is the natural logarithm and w_p and w_e refer to the widths on the poleward and equatorward side of the AR spine, respectively.

Taking the logarithm introduces a convenient sign into the analysis, such that a negative value for s corresponds to an AR whose w_p is greater than its w_e, while a positive s always means the opposite is true, and a zero indicates symmetry. Thus the finding here that s tends to be positive (Figure 4.8) indicates that ARs tend to be broader on their equatorward side, consistent with both the higher background moisture at lower latitudes, as well as the cold-frontal region frequently present on an AR's poleward side. Meanwhile, a tendency towards more negative s values as SST increases is reflected by systematically enhanced expansion of w_p over w_e, and indicates that a larger proportion of AR widening occurs on the poleward side than the equatorward side. This result follows nicely from expectations set up by basic thermodynamics: since the Clausius-Clapeyron (CC) relation describes an inverse function between local temperature and saturation vapor pressure (e^*), the larger relative e^* increases through these colder regions can result in an enhanced broadening of the IVT field here in the absence of changes to wind speed. That said, we do have to account for wind speed changes: returning to Figure 4.4, it is clear that wind speeds decrease slightly through the column, especially on the poleward sides of ARs. Given this side of an AR is frequently occupied by an accompanying ETC's cold front, this can be explained best by changes in ETC dynamics. In particular, this could occur as a result of weakening ETC background-to-core sea-level pressure (SLP) gradients, which is facilitated by decreasing background SLP in the storm-track region and leads to a relative weakening in ETC intensity (McDonald, 2011). In any case, the finding that relative changes in AR IVT increase overall and especially along ARs' poleward flanks (Figure 4.5d, f, h) despite these weakening winds indicates that q increases dominate changes in IVT. While the finding that q changes dominate IVT changes in ARs has already been discussed in-depth (McClenny et al., 2020), the cross-sections here

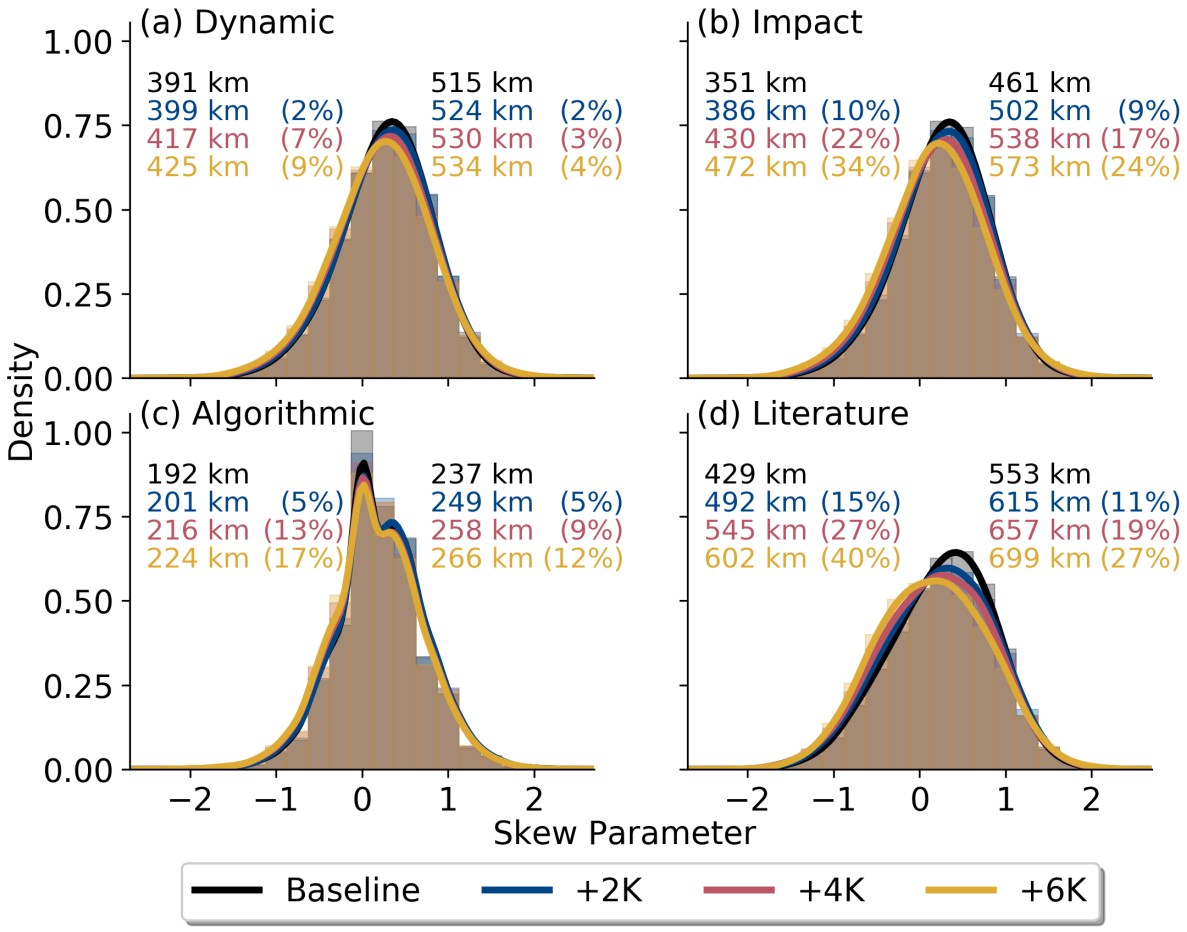

Figure 4.8: Distributions of AR skew parameter by method. Curves show kernel density estimates while shading shows the underlying histograms (bin spacing = .125). Textual annotations show half-widths (km) and their changes with respect to the Baseline run (%), with values on the left corresponding to the poleward side of the AR, and values on the right to the equatorward side. Note that this convention is consistent with all cross-section figures for reference.

have the advantage of explicitly illustrating the spatial variation of this effect. In particular, they show that a weakening AR periphery-to-core wind gradient under uniform SST increases works in synergy with thermodynamically modulated q changes along the poleward side to broaden the IVT field further, compounding the asymmetric widening seen here.

4.3.6 Relating impacts and dynamics in the context of AR width

We have demonstrated increases in AR width for all definitions, but in particular the impacts-relevant widths (that is, those conditioned on the critical threshold of $IVT \geq 250$ kg m^{-1} s^{-1}) show the strongest widening, in both the case of the AR IVT profiles themselves (wl) and their Gaussian approximations (wi). While some of this can be explained by the approximately linear enhancement in $IVT0$ under SST warming conditions (Figure 4.6), the simultaneous enhancement in wd also hints at an overall broadening in the AR IVT field. Returning to our definition for wi, we can quantitatively relate changes in wi to those in wd, $IVT0$, $dIVT$, or any combination thereof (Section 4.2.3). We evaluate the contribution of each via a first-order Taylor series expansion of Equation 4.2.4 with respect to each independent variable:

$$\Delta wi = \left.\frac{\partial wi}{\partial wd}\right|_B \Delta wd + \left.\frac{\partial wi}{\partial IVT0}\right|_B \Delta IVT0 + \left.\frac{\partial wi}{\partial dIVT}\right|_B \Delta dIVT + r \tag{4.3.2}$$

where r denotes a residual value, $\Delta X = X_t - X_B$ for all variables, and subscripts t and B refer to *test* and *Baseline* values, respectively. We refer to the terms on the right hand side as the *wd term*, *IVT0 term*, and *dIVT term*, respectively. We compute the prefixes for the Baseline AR cross-sections with mean wi and wd values:

$$\frac{\partial wi}{\partial wd} = \frac{wi}{wd}, \tag{4.3.3}$$

$$\frac{\partial wi}{\partial IVT0} = \frac{wd^2}{4\ wi\ (IVT_{ref} - IVT0)}, \tag{4.3.4}$$

$$\frac{\partial wi}{\partial dIVT} = \frac{wd^2}{4\ wi\ dIVT}. \tag{4.3.5}$$

In words, Equations 4.3.3, 4.3.4, and 4.3.5 each describe the first-order sensitivity of AR wi to AR wd, $IVT0$, and $dIVT$, respectively. Consequently, its derivative (Equation 4.3.2) can be used to evaluate how much each variable contributes to projected changes in AR wi. Table 4.2 shows the value of each term in Equation 4.3.2; notably, small r values ($\sim 5-10\%$ of the total magnitude) indicate that the linear approximations employed here can sufficiently characterize changes in AR wi. Meanwhile, Figure 4.9 also illustrates the

contribution of each. Like Figure 4.1, Figure 4.9 shows a collection of curves corresponding to an AR IVT Gaussian and a series of transformations on that Gaussian as each of the three free parameters is increased in turn, but instead uses the mean Baseline Gaussian IVT fit as a reference curve; accordingly, each transform is computed from the +6K mean Gaussian fit parameters, and the fitted mean +6K IVT Gaussian is also shown. Overall, this figure summarizes findings shown in Table 4.3 as well as those garnered from figures throughout the manuscript: first, that *wi* expansion far outpaces *wd* widening (Figure 4.7); second, that this widening is asymmetrical and characterized by greater widening on the poleward side than the equatorward side (Figure 4.8); third, that *wi* enhancement occurs mostly as a result of *wd* and $IVT0$ increases, which are nearly equal to each other and outpace $dIVT$ increases (Table 4.2); and last, this *wd* broadening occurs simultaneously with enhanced $IVT0$, whose mean steadily nears the critical threshold (Figure 4.6). Still, growing residuals with warming (Table 4.2) suggest that discrepancies in *wi* measurements (generally somewhat overestimated on the poleward side and underestimated on the equatorward side; Figure 4.9) indicate that a more detailed analysis may be necessary to characterize these changes.

	Δwi	*wd* Term	$IVT0$ Term	$dIVT$ Term	r
+2K	72.4	21.8	29.5	17.3	3.8
+4K	143.3	49.1	49.3	33.3	11.7
+6K	209.8	69.9	70.0	46.1	23.7

Table 4.2: Changes in AR *wi* under warming SSTs, as well as the contributions of changes in *wd*, $IVT0$, and $dIVT$ to *wi* as described in Equation 4.3.2. All values have units km.

To provide some of this additional detail, we perform the analysis summarized in Table 4.2 but treat the poleward and equatorward sides of the ARs as cross-sections distinct from one another. We accomplish this by (1) breaking up AR cross-sections into their left (poleward) and right (equatorward) halves, starting from the spine and extending to the last background IVT point; then (2) performing the same line-fitting procedures for *wd* and *wi* already described, but on each AR half independently from the other. Note that these capture more detail by having more flexibility. Specifically, fitting Equation

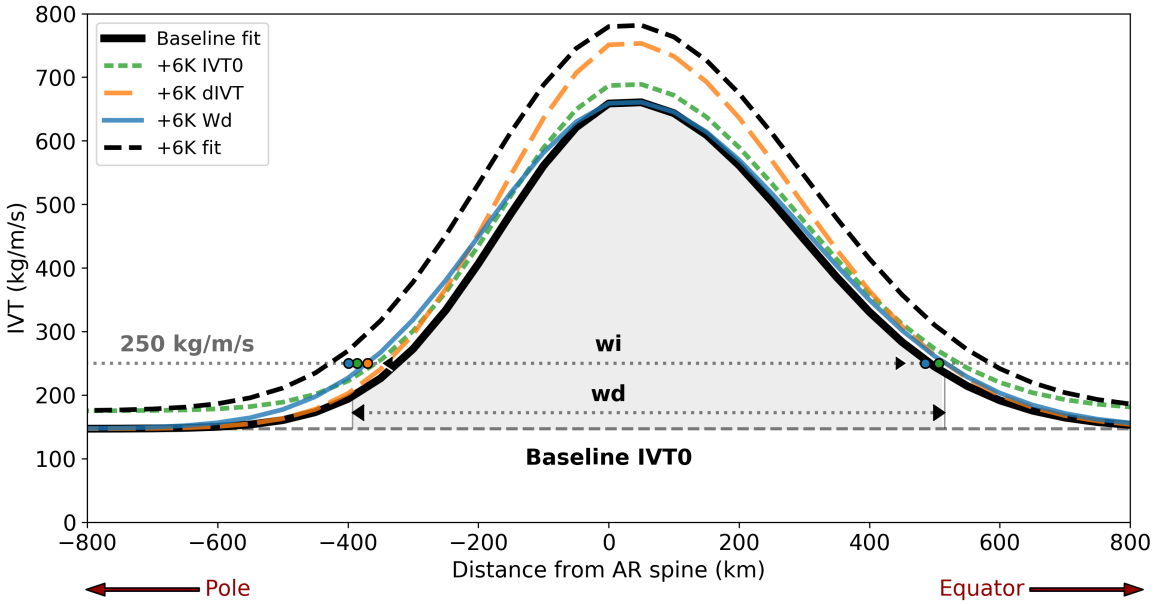

Figure 4.9: Analogous to Figure 4.1, but for Gaussian fits as derived in this paper. The thick, black curve shows the mean Gaussian IVT fit for the Baseline run, while the black, dashed curve shows the same for the +6K run. The other curves each correspond to a controlled, single-parameter transform on the Baseline curve derived from the +6K data: the short, green dashes show the Baseline Gaussian but with mean +6K $IVT0$; the long, orange dashes show the same, but with +6K's mean $dIVT$ instead; and the solid, blue curve shows the Baseline curve but with +6K mean wd. Corresponding dots along the $y = 250$ kg m^{-1} s^{-1} line show the resulting wi for each transform, which is slightly overestimated on the poleward edge and undestimated on the equatorward edge, for reasons already discussed (Section 4.3.2).

4.2.2 to each side separately essentially doubles the degrees of freedom from three to six IVT parameters, allowing for more precise wd estimates and minimizing the effect of the apparent underestimation of $IVT0$ along the AR poleward side and overestimation along the equatorward side. Table 4.3 summarizes this analysis and shows an overall decrease in r values, indicating that this additional flexibility does serve to capture more of the variability in each AR IVT profile. In particular, it captures important differences in the nature of AR wi changes on each side of the AR spine: whereas the wd term increasingly dominates the wi signal on the poleward side of ARs under SST warming (Table 4.3, left), the wi changes along the equatorward side of the AR have relatively equal contributions from all three terms, though $dIVT$ exceeds the others slightly and wd consistently shows the smallest change (Table 4.3, right).

	Δwi	wd Term	$IVT0$ Term	$dIVT$ Term	r
+2K	32.7	13.7	9.3	8.2	1.5
+4K	73.5	39.2	12.5	17.2	4.5
+6K	109.0	59.8	17.1	24.9	7.2
	Δwi	wd Term	$IVT0$ Term	$dIVT$ Term	r
+2K	38.1	11.4	11.8	13.1	1.7
+4K	67.4	18.2	22.1	24.5	2.5
+6K	101.7	28.4	31.0	37.5	4.8

Table 4.3: Same as Table 4.2, but for the poleward (top) and equatorward (bottom) sides of the AR cross-sections. Note that the sums of like terms for each side of the AR might not equal the corresponding term for the total AR in Table 4.2, since we allowed additional degrees of freedom when fitting separate IVT parameters for each side.

As noted in McClenny et al. (2020), and as observed here (Figure 4.7), although TE uses a Laplacian threshold for detection of ARs that should be invariant to changes in $IVT0$, it nonetheless produces wider ARs under warming conditions. The increased width of detected features tends to make ARs appear "less extreme" since the periphery points added through detection have lower IVT and precipitation compared with the AR core. In fact, if IVT0 is neglected from the change in impacts width (i.e., using Table 4.2 but only assessing $\Delta wi = \Delta wd + \Delta dIVT$) we would anticipate a mean AR width increase of 4.8%, 10.1% and 14.3% for the +2K, +4K and +6K simulations, which is perfectly in line with observations in Figure 4.7. Thus we can conclusively attribute increased AR widths in TE to broadening of ARs (wd) and intensification of ARs against the background IVT ($dIVT$).

4.4 Conclusions

This study used CAM5 in order to investigate in detail some of the physical drivers behind the apparent warming-related AR widening observed for a variety of simulation boundary conditions (BCs) and ARDTs (Espinoza et al., 2018; McClenny et al., 2020; O'Brien et al., 2020). To minimize variability related to BC differences, we use an AQP

configuration featuring an idealized reference SST profile and three test SST profiles with uniform increases of two, four, and six K over the reference. Likewise, we seek to avoid the sensitivity of AR width statistics to ARDT selection. We do this by only using the ARDT (as described in Section 4.2.1) as a first filter for AR points, instead focusing primarily on the pointwise local maxima of the IVT field (referred to as the "AR spine") and then examining interpolated cross-sections through the spine. We expect our methodology produces nearly identical results regardless of the ARDT employed. Four definitions for the AR cross-sectional width are then contrasted: (1) the lateral boundaries found by the ARDT (wa; Section 4.2.3), (2) wl, which defines AR width as all points along the cross-section featuring $IVT \geq 250$ kg m^{-1} s^{-1} and is used here to provide a direct comparison to an observational study by Ralph et al. (2017); (3) wd, which computes AR width with respect to a Gaussian fit of AR cross-sectional IVT (Equation 4.2.2); and (4) wi, which like wl is conditioned on the critical threshold $IVT \geq 250$ kg m^{-1} s^{-1}, but is instead determined with respect to the same Gaussian IVT curve as wd (Figure 4.1 provides a schematic view of wd and wi on a Gaussian AR IVT profile).

We present a summary of our findings below in parallel with the questions outlined in Section 1:

(a) Idealized Gaussian fits of AR IVT capture most of the variance of the AR IVT profile (weighted RMSEs generally remain under 0.10; Figure 4.5), though these fits benefited substantially from the use of a simple weighting function (Equation 4.2.5) to ensure that high-IVT points at AR peripheries did not unduly influence the wd and wi calculations. Because of asymmetries related to a skew of AR IVT toward their equatorward flank, the fit can be improved by using a half-Gaussian on each side of the spine.

(b) AR background IVT ($IVT0$) systematically increases more than AR intensity ($dIVT$), though both show nearly linear increases in their means ($\sim 6\%$ versus $\sim 4\%$ per K SST warming; Figure 4.6). In words, we show that the local background IVT field is enhanced with respect to AR peak IVT. This finding reflects earlier results that uniform SST increases generally lead to larger enhancements in non-AR IVT than

in AR IVT (McClenny et al., 2020), though instead featuring a partitioning of AR points between their peak IVT values and their background environment. In all, this effect is attributed to points already discussed in McClenny et al. (2020), which showed that AR relative humidity decreases through the column since temperature changes aloft outpaced the prescribed SST increases.

(c) All measures of AR width systematically increase under uniform SST warming, though substantial variation exists in terms of the magnitudes of these relative changes (Figure 4.7). We show that AR dynamic width (wd) is the least sensitive with a mean increase of $\sim 1\%$ per K, while the TE ARDT produces ARs which expand by $\sim 2.5\%$ per K SST on average. Meanwhile, the AR widths concerned with the impacts-relevant critical IVT threshold ($IVT \geq 250$ kg m^{-1} s^{-1}) show the largest increases under SST warming: wi and wl both expand by $\sim 5-6\%$ per K. As for the smaller expansion rate seen in wi compared to wl, we cannot rule out spurious effects associated with the curve-fitting procedure, which tends to underestimate AR IVT at the profile's inflection points (Section 4.3.4). That said, the Gaussian fits from which we compute wi have the advantage of isolating the AR IVT signal from a noisy background (Figure 4.5), suggesting that nearby high-IVT objects (e.g., other ARs, ETCs) can inflate AR widths conditioned on this IVT threshold. In any case, it is notable that each AR width estimate exhibits an asymmetric sensitivity to SST warming characterized by larger relative width increases on the poleward than the equatorward side (Figure 4.8), which is attributed to an enhanced thermodynamic sensitivity in e^* at lower temperatures.

(d) Mean AR wi, which corresponds to the impacts-relevant width of an AR's idealized Gaussian representation, widens overall at a rate of ~ 35 km per K SST (Table 4.2). Broken down by term, we see the largest contribution to this wi expansion comes from an enhancement in background IVT ($IVT0$, accounting for ~ 13 km per K), then changes in dynamic width (wd, adding ~ 11.5 km per K), and the lowest contribution from AR intensity ($dIVT$, of ~ 8.2 km per K). When this analysis is partitioned along the AR spine and examined separately for each the poleward and

equatorward sides of ARs, a clearer picture of the processes behind the asymmetric widening discussed in (c) emerges (Table 4.3). While each side shows an equivalent mean widening of $\sim$ 17.6 km per K SST warming, the contributions of each term vary substantially across the AR spine. On the poleward side, wi increases are dominated by wd ($\sim$ 9 km per K) and receive comparable contributions from enhancements in $IVT0$ and $dIVT$ ($\sim$ 3.5 and $\sim$ 4.2 km per K, respectively). At the same time, wi along the equatorward side exhibits a much smaller contribution from wd ($\sim$ 5 km per K), and larger contributions from thermodynamic enhancements in $IVT0$ ($\sim$ 5.5 km per K) and $dIVT$ ($\sim$ 6.3 km per K) than the poleward side. The finding that wd dominates wi increases on the poleward side is intriguing and suggests that AR IVT profile changes here are sensitive to an enhanced breadth in the overall IVT field which is facilitated here in part by CC scaling but also by weakening frontal wind gradients (Figure 4.4). Our results further explain that the increase in AR width observed in McClenny et al. (2020) using the TE ARDT is in near-perfect agreement to increases in $dIVT$ and wd, indicating that the TE ARDT is effective at filtering changes in width due to increases in the background IVT.

This study carefully leveraged idealized models in two notable senses: first, the use of an AQP model allowed us to isolate the influence of uniform SST warming on AR IVT intensity and width; second, information about AR width and its responses to SST warming was itself derived from idealized Gaussian fits to AR IVT cross-sections. While these idealized approximations of AR IVT cross-sections invariably smooth out natural variability, they have the advantage of representing AR impacts-relevant width (wi) in terms of a known function with free parameters derived from the local IVT field for each cross-section (Equation 4.2.4). In this framework, an increase in any of these parameters could account for the AR wi increases, likewise elucidating the physical drivers of previously documented AR widening across warming scenarios and ARDTs (Espinoza et al., 2018; McClenny et al., 2020; O'Brien et al., 2020). Quantitative analysis presented here shows that AR wd increases—that is, an overall broadening of the AR IVT profile—on the poleward side of ARs accounts for $\sim$ 28% of wi widening in the warmest SST scenar-

ios (+4K and +6K), making its contribution roughly twice the magnitude of any other (Table 4.3). While this is certainly facilitated in part by simple thermodynamic effects in this relatively cold AR region, we argue that dynamical effects also play a crucial role. Namely, given the frequent presence of an ETC's cold front along an AR's western edge (Ralph et al., 2017), it follows that weakening ETC SLP gradients (McDonald, 2011) similarly weaken AR wind gradients (Figure 4.4). This finding of AR IVT poleward expansion paired with the finding that AR background IVT increases outpace those in AR spine IVT (Figure 4.6) together suggest that researchers take care when characterizing AR intensity in terms of maximum IVT.

Acknowledgments

Previous and current CESM versions are freely available online (at `http://www.cesm.ucar.edu/models/cesm2/`). TempestExtremes AR detection software are available for public use on GitHub (at `http://www.github.com/ClimateGlobalChange/tempestextremes`). Data used to generate figures for this manuscript, as well as model configuration and AR detection details, are archived at Zenodo (`https://doi.org/10.5281/zenodo.4393034`). This material is based upon work supported by the U.S. Department of Energy, Office of Science, Office of Biological and Environmental Research program under Award Number DE-SC0016605 "A framework for improving analysis and modeling of Earth system and intersectoral dynamics at regional scales." This project is also supported by the National Institute of Food and Agriculture, U.S. Department of Agriculture, hatch project under California Agricultural Experiment Station project accession nos. 1010971 and 1016611. This research used resources of the National Energy Research Scientific Computing Center, a DOE Office of Science User Facility supported by the Office of Science of the U.S. Department of Energy under Contract No. DE-AC02-05CH11231.

Chapter 5

Conclusions

The overarching motivation of this research was to develop confidence in conclusions about AR responses to climate change. We proposed that this confidence could be developed best by leveraging an assortment of simpler models. First, we minimized uncertainty related to surface boundary conditions and complex climate change forcings by performing all experiments within an aquaplanet. Within this aquaplanet framework we performed a simple forcing experiment of uniform SST increases in order to insulate findings from effects associated with a changing meridional SST gradient (and other changes) normally found in climate change experiments. This allowed us to isolate the impact of increased SST, a first for a global AR study.

5.1 Summary

In Chapter 2, we provided a brief overview of the wide variety of AR detection tools (ARDTs) described in the literature. We also detailed TempestExtremes (TE), an ARDT which is novel because it accepts a threshold for the Laplacian of IVT (L^2IVT) rather than for a "raw" IVT field, the variable on which most ARDTs depend. The use of L^2IVT allows TE to identify ARs as ridges in the IVT field. We show that this has the advantage of isolating ARs from their background without enforcing an absolute IVT threshold which is sensitive to background climatology, or a relative threshold which requires percentiles that can be sensitive to the spatiotemporal extent of the calculation (e.g., does the percentile calculation use zonal mean IVT? Does it compute new percentiles

for climate change scenarios, or does it use present-day data?). Using L^2IVT is somewhat complicated however; analysis presented in Chapter 2 show that it benefits from tuning for individual models, in particular as a function of the model's grid spacing. Nevertheless the flexibility with respect to the changing IVT background afforded by the use of L^2IVT makes it a novel ARDT, useful in and of itself and in the context of the ARTMIP effort, where it provides a unique point of comparison.

In Chapter 3, we tested the response of AR occurrence frequency (OF), IVT, and precipitation rates to uniform SST increases. We found that AR OF increases overall and mostly as a result of increased AR zonal extent, while a poleward displacement of the AR OF maximum followed the same for the EDJ. Meanwhile, we kept with the theme of simpler models by examining changes in zonal mean AR IVT and precipitation rate with linear decompositions of thermodynamic and dynamical contributions to tease apart the individual factors leading to these changes. We find that for AR IVT the thermodynamic contributions dominate; that is, enhanced AR IWV compensates for decreasing mean AR low-level wind speeds. We noted that this increase in AR IWV masks AR RH decreases at upper levels which occur as a result of enhanced upper-tropospheric warming with respect to the prescribed SST increases. This upper-tropospheric warming is not surprising and results as a consequence of a dampened moist-adiabatic lapse rate under surface warming conditions; nevertheless it is reassuring to see the model results follow theory-based predictions.

As for AR IVT, Chapter 3 also used a simple linear model to describe changes in AR precipitation rate. Once again, we found increasing AR moisture (in this case, q_{sfc} rather than IWV) and weakening AR dynamics (ω_{700}) are at odds with one another, though this time the weakening dynamics were sometimes sufficient to contribute to a decrease in zonal mean AR precipitation rates. We also showed that increasing AR area as SST increases somewhat obscures conclusions about zonal-mean AR precipitation rates, since the expansion of AR area produced by TE resulted in the inclusion of weaker AR periphery points featuring less vigorous precipitation.

The result of expanding ARs using the TE ARDT was unexpected because the use

of L^2IVT makes it insensitive to uniform additive IVT increases, and TE should only produce a $\sim$1% wider AR for a 50% uniform multiplicative increase in IVT (Text A.1). We hypothesized in Chapter 3 that this widening occurred as a result of a broadening in the IVT field about an AR cross-section. Once again we investigated this by leveraging a simpler model, in this case by characterizing AR IVT cross-sections as Gaussian curves with three free parameters: the constant background IVT ($IVT0$), the intensity of the AR peak IVT above the background ($dIVT$), and the overall breadth of the IVT field (also called the *dynamic width*; wd). First, we established that Gaussian curves provide reasonable estimates of AR IVT cross-sections. We next examined changes in $IVT0$ and $dIVT$, and found that $IVT0$ overall exhibits larger relative increases than $dIVT$, in keeping with results in Chapter 3 which showed that non-AR IVT increases at greater rates than AR IVT for a given uniform SST increase.

After establishing the sensitivity of the IVT fit parameters in Equation 4.2.2, Chapter 4 used the Gaussian fits of the AR IVT cross-sections to define an impacts-relevant AR width (wi) conditioned on the common critical threshold $IVT \geq 250\ \mathrm{kg\ m^{-1}\ s^{-1}}$ (Equation 4.2.4). We compared the wd and wi values against a *literature width* (wl) which was computed simply as all points along an AR transect which exceeded the critical threshold of IVT, and against the *algorithmic width* (wa), or the AR boundaries as identified by TE. We found systematic increases in all widths, though the widths conditioned on the critical IVT threshold (wi and wl) showed the most sensitivity to SST warming, while wa and wd showed the lowest sensitivity.

Like the linear decompositions of AR IVT and precipitation rate into dynamical and thermodynamic contributions used in Chapter 3, differentiating the equation describing wi with respect to each variable provided us with a framework to study the individual contributions of each parameter to any observed changes (Equation 4.3.2). From this analysis we found that $IVT0$ and wd enhancement contributed equivalently to wi increases, with $dIVT$ contributions trailing behind. The overall widening result is not symmetric however: an analysis which partitioned ARs into their equatorward and poleward sides revealed that the poleward sides of ARs are most sensitive to wd changes,

while the equatorward side received nearly equal contributions from all three parameters. We attribute the expansion of wd on the poleward side to a mix of enhanced Clausius-Clapeyron-mediated moisture increases and a broadening lower-level wind field. Last, we showed that TE produces wider ARs under SST warming due to enhancements in wd and $dIVT$, supporting our earlier hypothesis that TE is insensitive to changes in background IVT.

5.2 Recommendations

The works contained herein inspire us to make a few recommendations. First, in Chapter 2 we commented on the challenge of tuning TE parameters, both within a single model and when comparing AR statistics across models. Despite the tuning already done, there could be additional efforts towards it. One open question involves the scaling of IVT and L^2IVT to grid size—while we established some theoretical ground on that, the practical results (Figure 2.7) suggest that further scaling efforts may improve inter-model consistency. That said the comparison of different models makes it difficult to assess if improved scaling can indeed improve the AR OF spread, since model differences aside from grid spacing can contribute to discrepancies in AR statistics. Addressing this could involve a simplified approach: rather than compare AR statistics derived from untuned and grid-size-tuned L^2IVT criteria across a collection of models, we could instead interpolate one model (e.g., MERRA2) to a collection of different grid sizes, thereby allowing us to examine grid size sensitivities in an experiment which is controlled better for confounding factors.

Second, we expect that results from Chapter 3 could be further clarified by using techniques developed for Chapter 4, specifically the AR spine identification and cross-section generation procedures. For instance, in Chapter 3 we used an IVT-weighted analysis of precipitation rates to tease apart the influence of changes in AR "core" versus periphery points, with the rationale that AR cores tend to feature the highest IVT values along an AR cross-section. That approach certainly provided valuable insight, but our ability now to explicitly examine variables through an AR cross-section can be used to provide additional insight. We are particularly interested in revisiting the linear decompositions of

IVT and precipitation, this time evaluated at different points along the AR cross-section. This could be as simple as defining a core about the AR spine, while AR boundaries on each side could be determined with each of the width methods defined in Chapter 4 to assess the sensitivity of findings to them. We could then directly assign changes in AR variables as changes happening within the core or towards the AR periphery, giving us valuable insight to the spatial variation of intra-AR characteristics.

Last, results from Chapters 3 and 4 are limited to an aquaplanet setting, a tightly controlled and highly idealized framework. The advantages have already been discussed, specifically that the simplified setting allowed us to isolate the impact of SST warming in the absence of any other changes; still, we emphasize that aquaplanets and other simpler models leveraged in this work (e.g., the linear IVT/precipitation rate decompositions, the representation of AR cross-sections as Gaussians) are best viewed as tools for understanding AR responses to specific climate change forcings, rather than for predicting future AR behavior in general. As such, we recommend that the analyses in Chapters 3 and 4 be extended to coupled models, such as those in CMIP5/6 or in the High-Resolution Model Intercomparison Project (HighResMIP), since leveraging the model hierarchy in such a way can allow us to raise confidence in results obtained in these more complete yet complex climate model settings.

Appendices

Appendix A

Supplementary Information for Chapter 3

Contents of this appendix

1. Figure A.1
2. Text A.1
3. Figures A.2 to A.7

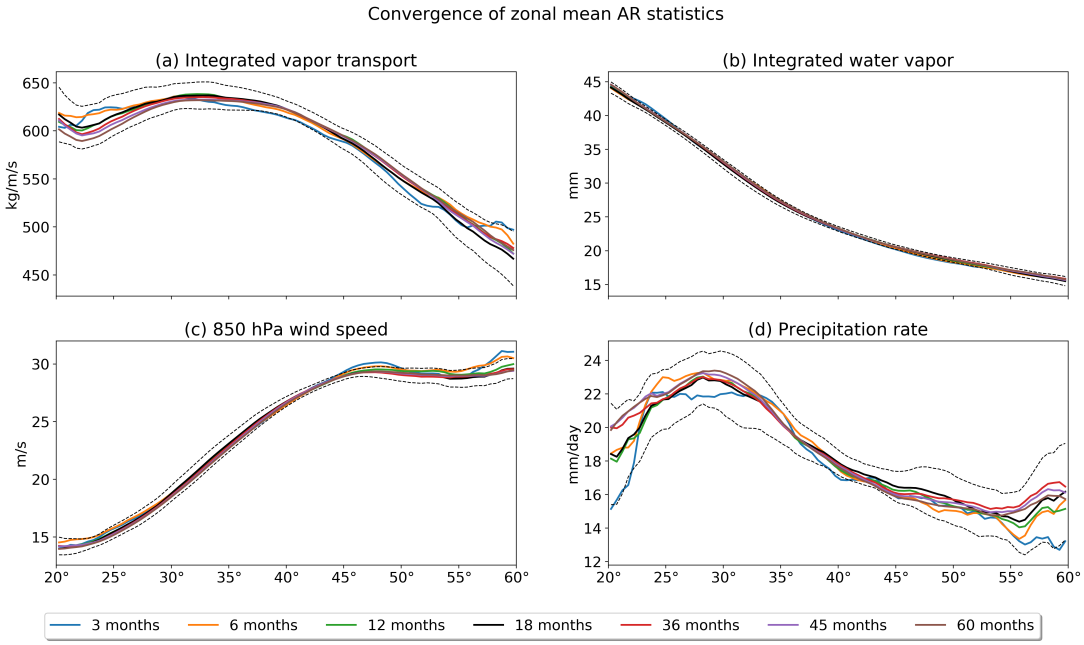

Figure A.1: Zonal mean AR quantities for the "Baseline" SST run. Line colors indicate the number of months in the sample. Black dashes show the 18-month mean +/- one standard deviation with respect to the full ensemble.

A.1 Sensitivity of Atmospheric River Width to Laplacian IVT Criterion

In this section we examine the sensitivity of the AR width to the Laplacian criteria under a multiplicative enhancement in total IVT. We begin by considering an idealized atmospheric river with Gaussian cross-section in IVT,

$$IVT(s) = IVT0 + dIVT \exp(-s^2/w^2), \tag{A.1.1}$$

where $IVT(s)$ is the pointwise IVT at distance s meters along the cross-section, $IVT0$ is the constant background IVT, $dIVT$ is the anomalous IVT enhancement from the AR, and w is the e-folding width of the AR. Since $IVT0$ is unimportant to the Laplacian criteria, we set $IVT0 = 0$ in this analysis. Figure A.2 depicts two such Gaussian profiles with e-folding width $w = \pi/90$ rad $= 222$ km, and a baseline $dIVT = 500$ kg/m/s and $dIVT = 500 \times 1.07^6 \approx 750$ kg/m/s, the latter corresponding to a 7% increase in IVT per degree C under a +6K experiment.

The second derivative of (A.1.1) with respect to s, which is equivalent to the Laplacian

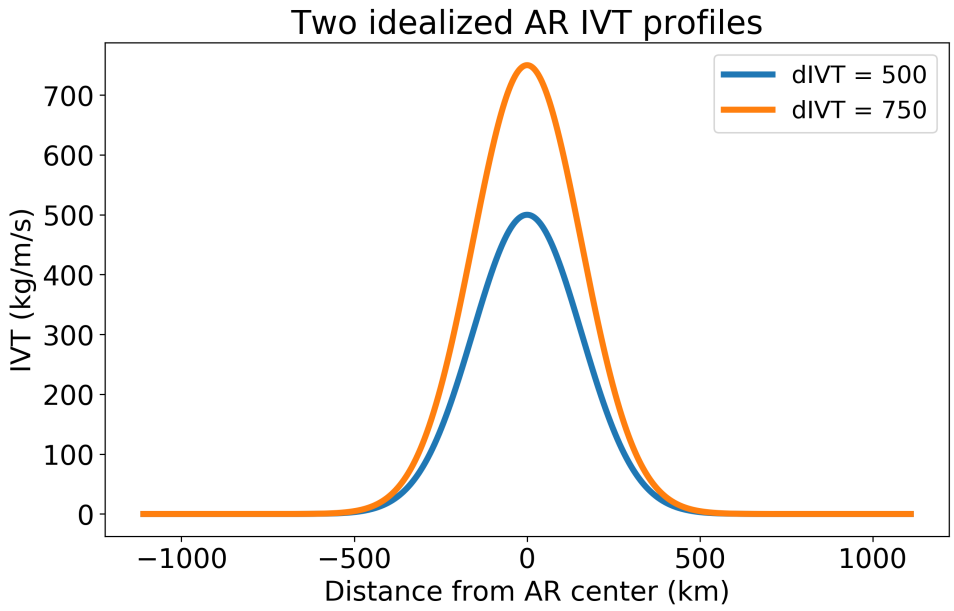

Figure A.2: A depiction of the idealized Gaussian cross-sections used in this analysis with $dIVT = 500$ kg/m/s and $dIVT = 750$ kg/m/s, which represent typical ARs under baseline and +6K experiments.

for an AR with no variation perpendicular to the cross-section, is then given by

$$\frac{d^2IVT}{ds^2}(s) = \frac{dIVT(4s^2 - 2w^2)}{w^4} \exp(-s^2/w^2), \tag{A.1.2}$$

with units of kg/m/s/m^2. To convert to kg/m/s/rad^2, which is used in our ARDT, we multiply by $(6.37122 \times 10^6$ m/rad$)^2$. The resulting profiles of the Laplacian are depicted in Figure A.2 along with the employed threshold of -40000 kg/m/s/rad^2. As can be seen in this figure the number of points satisfying the Laplacian threshold – that is, those points where the curve is below the dotted line – does not significantly change even when the strength of the AR is enhanced by 50%. To get a better handle on the magnitude of this change we can solve numerically for the point at which the second derivative hits our threshold and find that this occurs at $s = 5263$ m for the baseline AR and $s = 5335$ m for the +6K AR. Thus the multiplicative enhancement results in a mere 1.4% increase in the AR width.

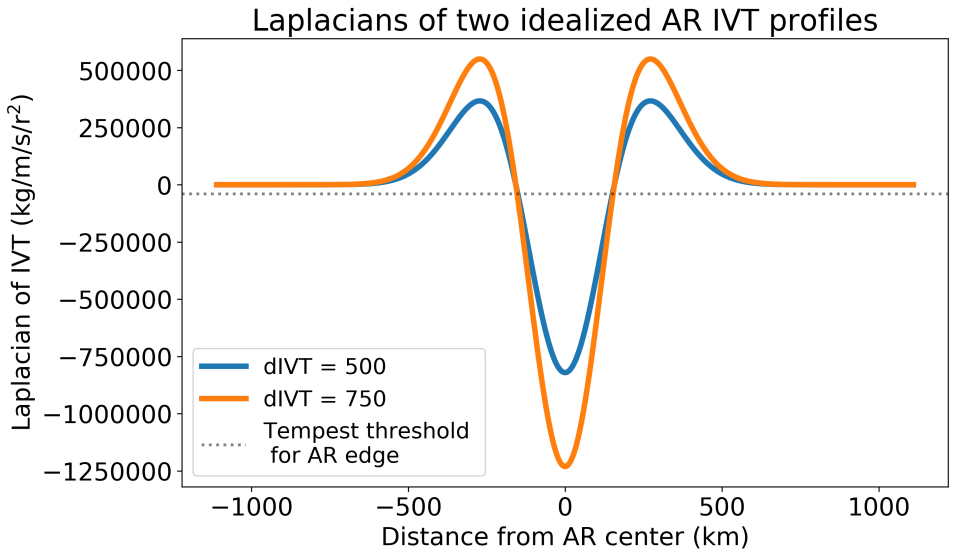

Figure A.3: As in Figure A.2, except depicting the second derivatives of the Gaussian cross-sections.

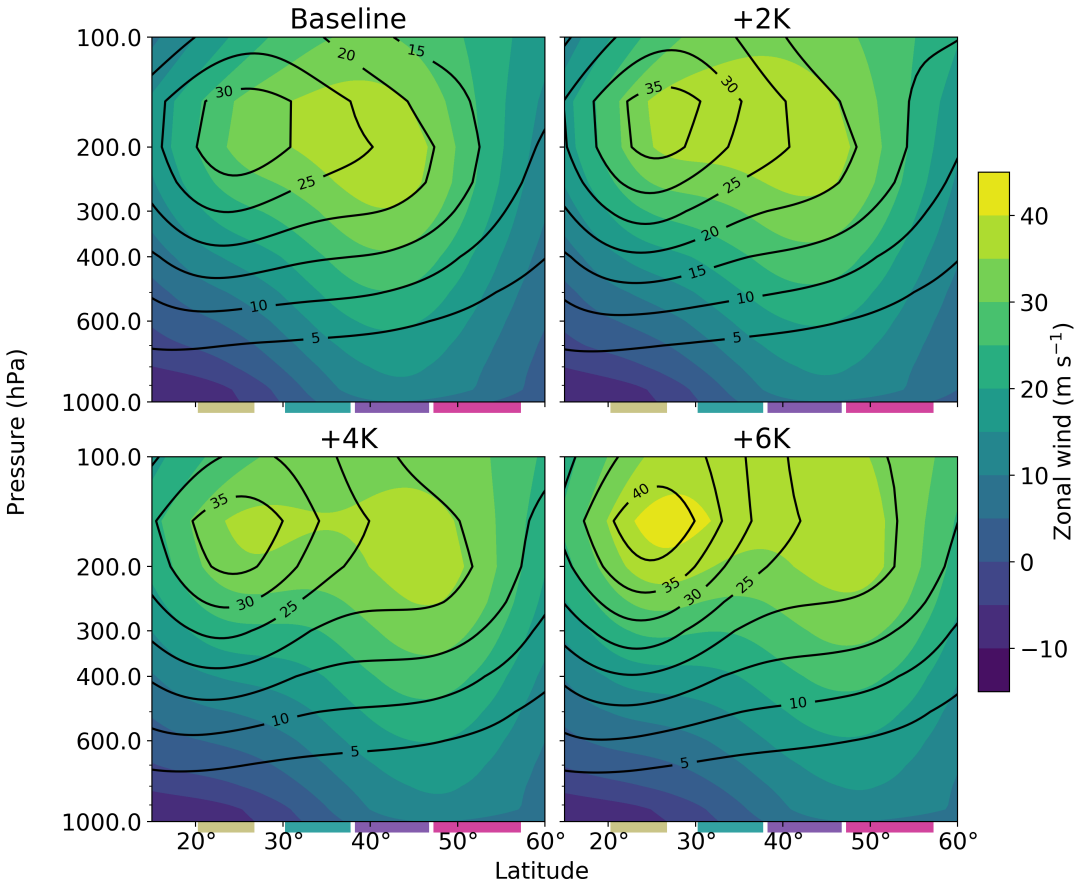

Figure A.4: Zonal jets for each SST run. Filled contours show zonal-mean zonal wind (m/s); the eddy-driven jet can be seen extending through the troposphere in the mid-latitudes. Unfilled contours show zonal-mean zonal wind minus 850 hPa zonal wind; the upper-tropospheric maximum seen in each panel is the subtropical jet. Colored boxes and labels on x-axis denote analysis subregions described in the main text (Section 3.2.4).

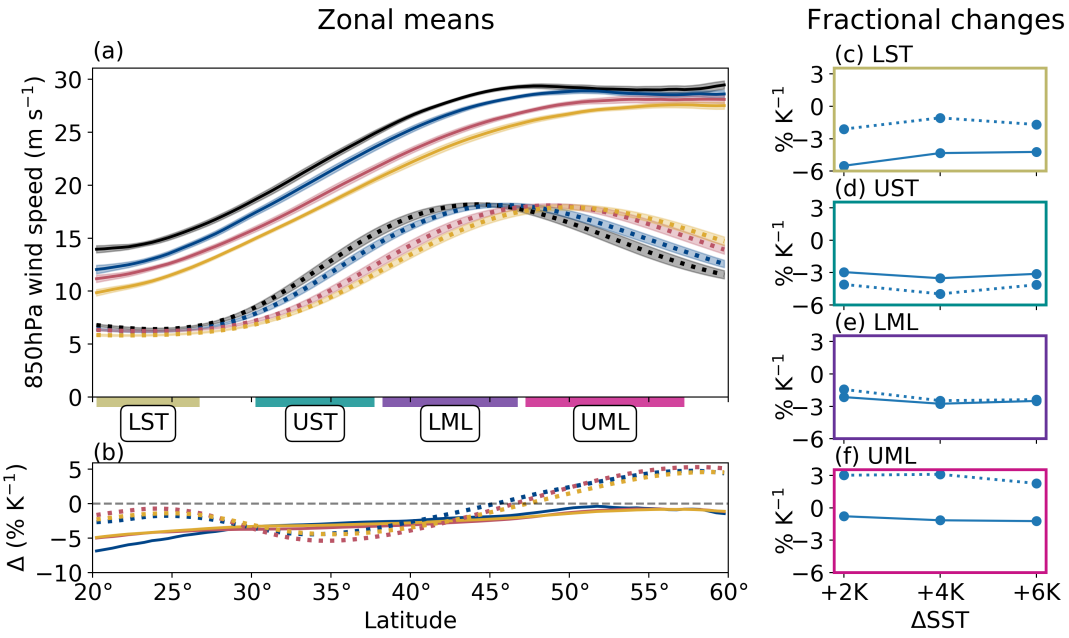

Figure A.5: (a) Meridional distributions of zonal mean AR (solid) and non-AR (dotted) 850 hPa wind speed. Shading shows 95% confidence intervals. (b) Relative differences with respect to the Baseline SST (%/K), using the same line color and style conventions. (c-f) Area-weighted mean relative change per K SST increase (blue; line style conventions as before). Colored boxes and labels on x-axis denote analysis subregions described in the main text (Section 3.2.4).

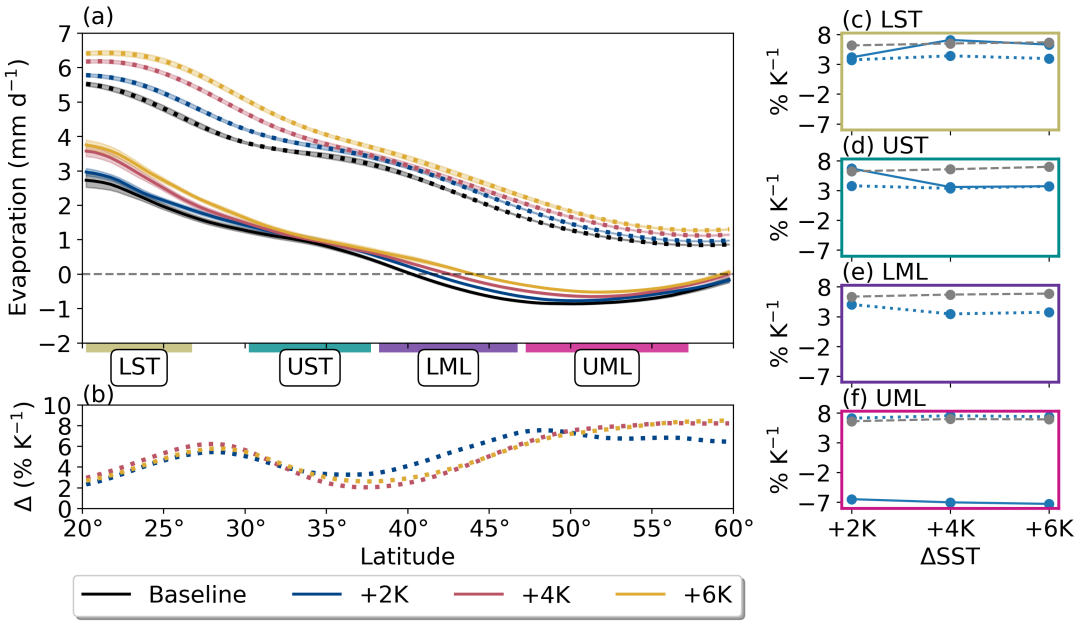

Figure A.6: As Figure A.5, but for surface evaporative flux, and with the addition of Clausius-Clapeyron predictions for near-surface saturation vapor pressure for reference (grey, dashed lines in c-f). Note numerical issues prevented us from plotting fractional changes in AR surface evaporative flux: since AR evaporation is near-zero in the LML, fractional changes through this region were artificially inflated.

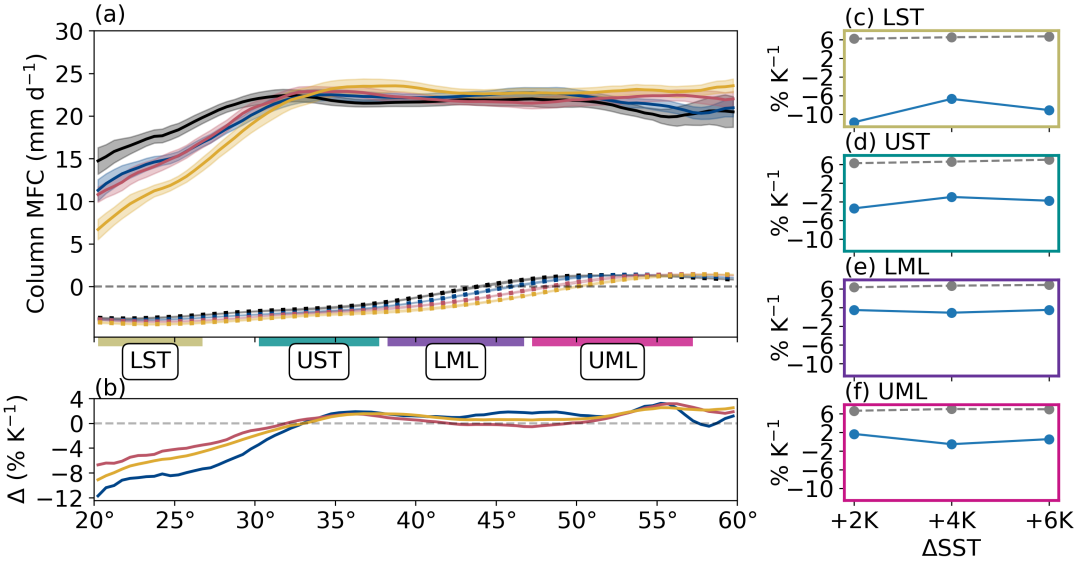

Figure A.7: As Figure A.5, but for column-integrated moisture flux convergence (MFC). Fractional changes are not shown for non-AR MFC since its very small magnitudes tended to result in spuriously large values.

Appendix B

Supplementary Information for Chapter 4

Contents of this appendix

1. Tables B.1 to B.3

2. Figures B.1 to B.3

Q	+0K	+2K	+4K	+6K
0.05	80.28	87.81 (9.38%)	96.23 (19.86%)	104.54 (30.21%)
0.25	118.67	131.42 (10.74%)	142.56 (20.13%)	158.08 (33.21%)
0.5	147.48	165.14 (11.97%)	179.82 (21.93%)	200.48 (35.93%)
0.75	180.75	203.58 (12.63%)	223.55 (23.68%)	249.4 (37.98%)
0.95	240.2	273.05 (13.68%)	301.18 (25.39%)	338.35 (40.86%)
Mean	152.37	170.71 (12.04%)	186.91 (22.67%)	208.18 (36.63%)

Table B.1: Absolute (relative) changes in AR $IVT0$ in kg/m/s (%) computed for a given quantile, Q.

Q	+0K	+2K	+4K	+6K
0.05	305.9	317.46 (3.78%)	324.74 (6.16%)	331.53 (8.38%)
0.25	392.21	410.44 (4.65%)	425.73 (8.55%)	439.87 (12.15%)
0.5	481.28	513.33 (6.66%)	543.15 (12.86%)	570.88 (18.62%)
0.75	612.23	672.06 (9.77%)	730.96 (19.39%)	791.53 (29.29%)
0.95	860.92	968.32 (12.48%)	1088.12 (26.39%)	1204.84 (39.95%)
Mean	519.67	563.02 (8.34%)	605.25 (16.47%)	647.86 (24.67%)

Table B.2: Same as Table B.1, but for AR $dIVT$.

Q	+0K	+2K	+4K	+6K
0.05	441.9	465.5 (5.34%)	485.96 (9.97%)	507.4 (14.82%)
0.25	531.05	562.38 (5.9%)	592.08 (11.49%)	625.28 (17.74%)
0.5	630.28	678.51 (7.65%)	723.81 (14.84%)	773.09 (22.66%)
0.75	772.77	857.97 (11.03%)	932.5 (20.67%)	1016.03 (31.48%)
0.95	1045.32	1178.84 (12.77%)	1321.77 (26.45%)	1467.12 (40.35%)
Mean	672.04	733.73 (9.18%)	792.17 (17.87%)	856.04 (27.38%)

Table B.3: Same as Tables B.1 and B.2, but for AR *spine IVT*.

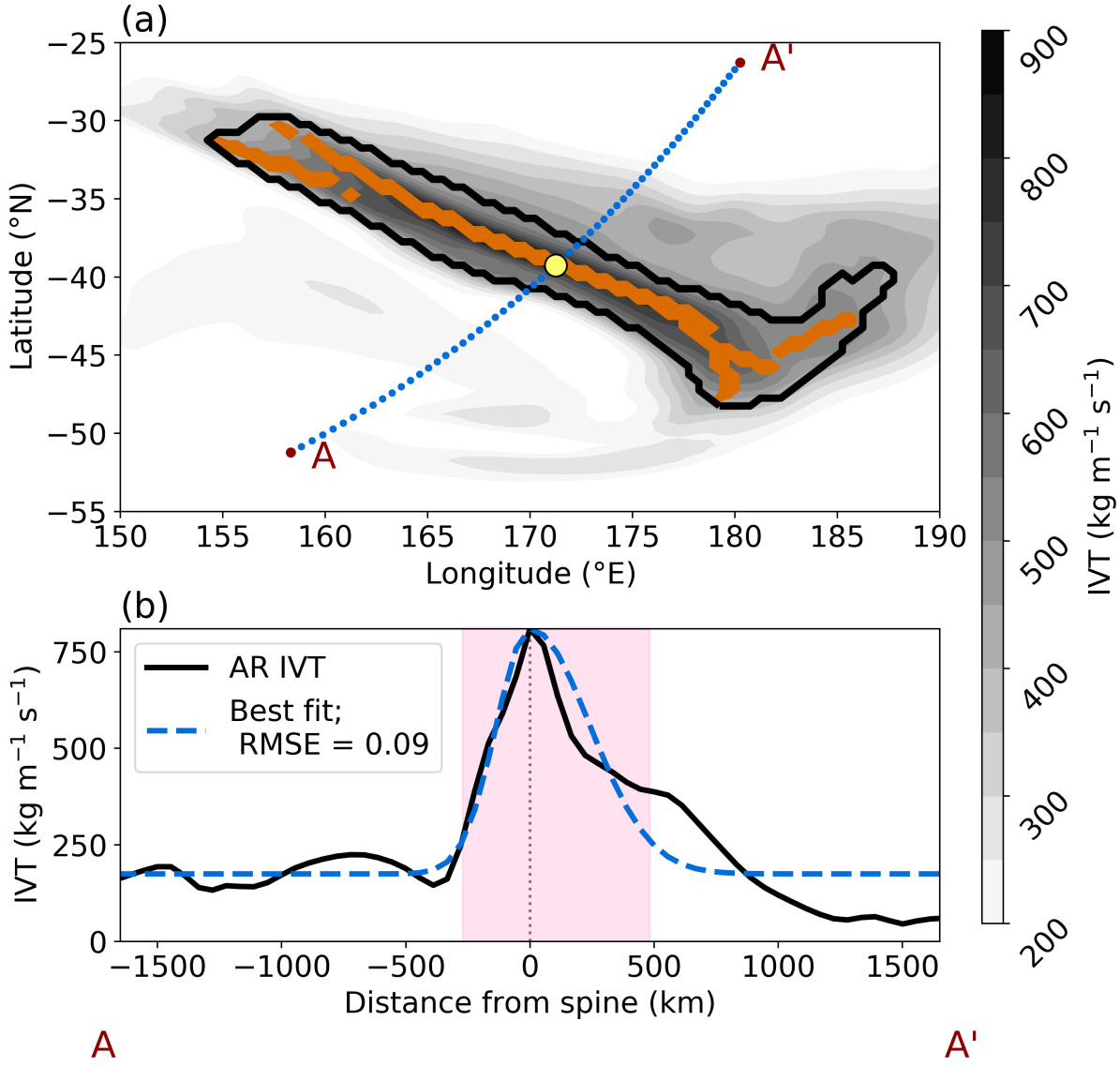

Figure B.1: Example of an AR featuring an RMSE between 0.05 and 0.1 with respect to its best-fit Gaussian. (a) IVT field (grayscale contours). Shown also are the AR boundaries (thick, black outline), spine (thick, orange lines), and cross-section points (blue, dotted line; bounded by points A and A') as detected by TE, as well as the mass-weighted AR centroid determined by scikit-image. (b) Cross-section in IVT from A to A' (black, solid curve) and the best-fit piece-wise Gaussian (blue, dashed curve). Pink shading shows wd, while the dotted line shows the spine location to clarify the asymmetry.

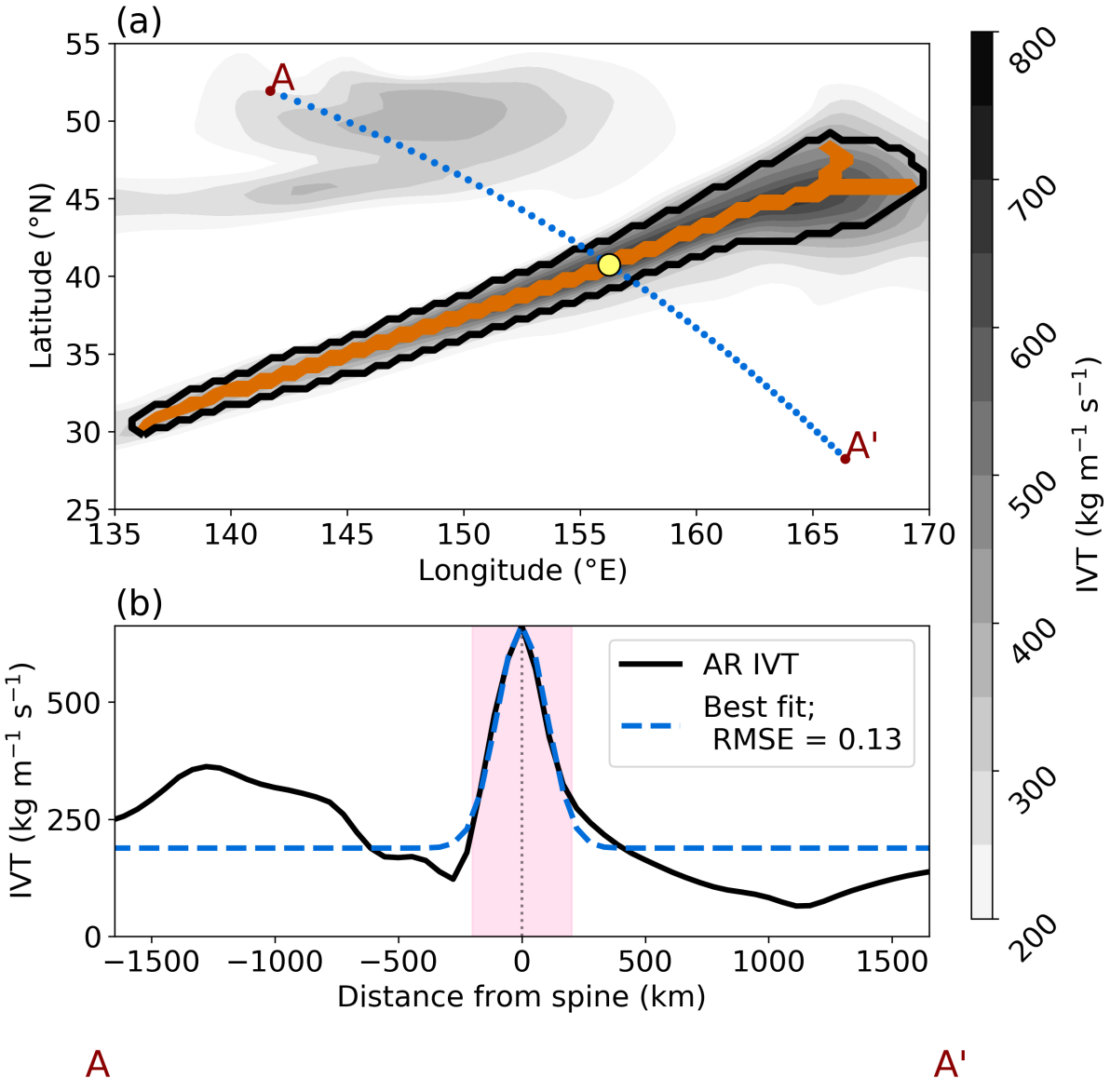

Figure B.2: As in Figure B.1, but for an AR featuring a moderate RMSE (between 0.05 and 0.1) with respect to its best-fit Gaussian.

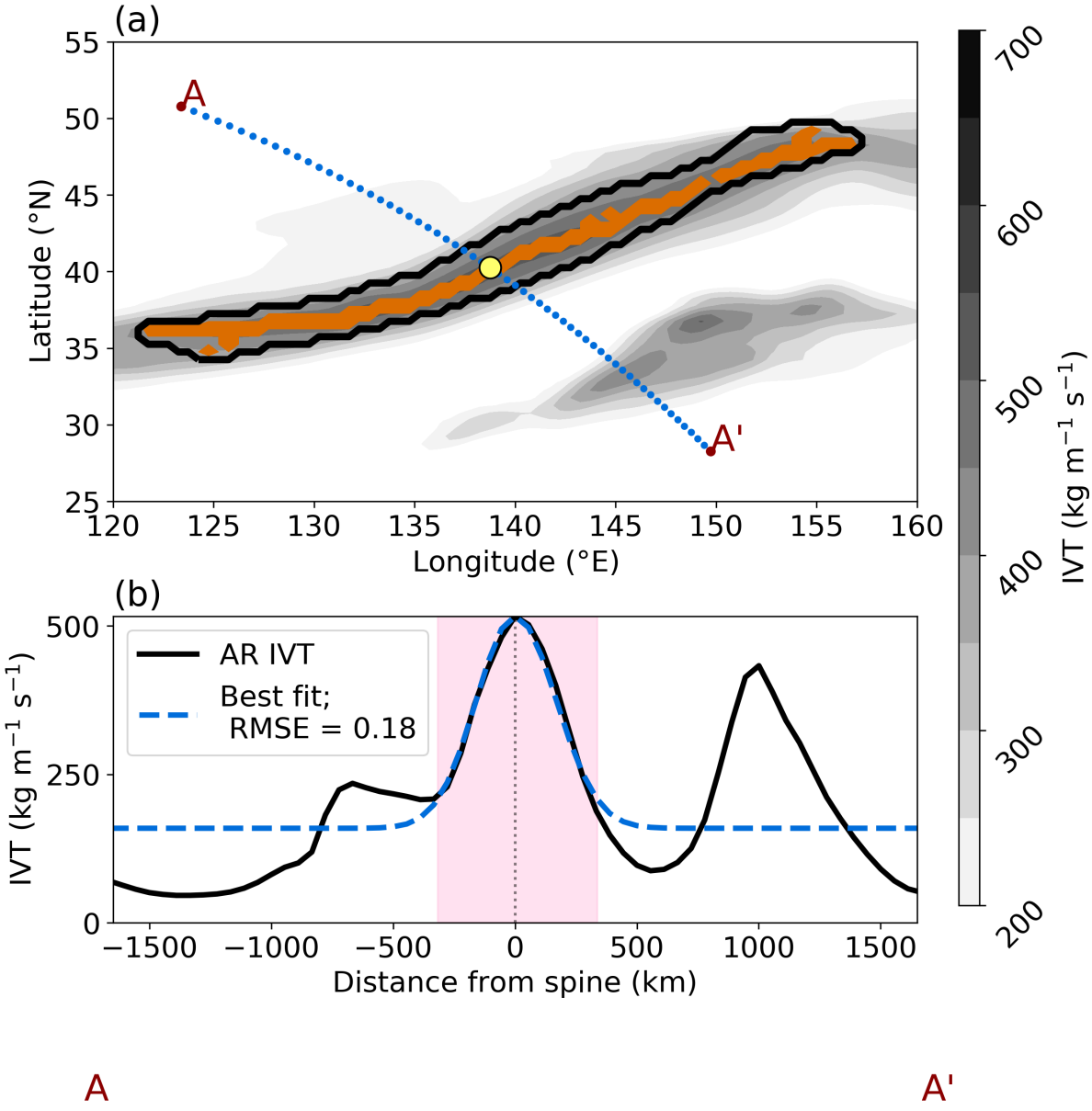

Figure B.3: As in Figures B.1 and B.2, but for an AR featuring a RMSE near the maximum allowed for study here (for reference, we did not consider ARs with RMSE > 0.2 with respect to their best-fit Gaussian curve). Since this fit is compromised mostly by a nearby high-IVT object, this example shows nicely the utility of Gaussian curves in isolating ARs from their environment and potential confounding objects.

References

AMS. Atmospheric river, May 2017. URL https://glossary.ametsoc.org/w/index.php?title=Atmospheric_river&direction=prev&oldid=13819.

J-W. Bao, S. A. Michelson, P. J. Neiman, F. M. Ralph, J. M. Wilczak, J-W. Bao, S. A. Michelson, P. J. Neiman, F. M. Ralph, and J. M. Wilczak. Interpretation of Enhanced Integrated Water Vapor Bands Associated with Extratropical Cyclones: Their Formation and Connection to Tropical Moisture. Monthly Weather Review, 134(4):1063–1080, 2006. ISSN 0027-0644. doi: 10.1175/MWR3123.1. URL http://journals.ametsoc.org/doi/abs/10.1175/MWR3123.1.

J. Bjerknes and H. Solberg. Life cycle of cyclones and the polar front theory of atmospheric circulation. Geophysisks Publikationer, 3(1):18, 1922. ISSN 1477-870X. doi: https://doi.org/10.1002/qj.49704920609. URL https://rmets.onlinelibrary.wiley.com/doi/abs/10.1002/qj.49704920609. _eprint: https://rmets.onlinelibrary.wiley.com/doi/pdf/10.1002/qj.49704920609.

Amy H. Butler, David W. J. Thompson, and Ross Heikes. The Steady-State Atmospheric Circulation Response to Climate Change–like Thermal Forcings in a Simple General Circulation Model. Journal of Climate, 23(13):3474–3496, July 2010. ISSN 0894-8755. doi: 10.1175/2010JCLI3228.1. URL https://journals.ametsoc.org/jcli/article/23/13/3474/32473/The-Steady-State-Atmospheric-Circulation-Response.

T.N Carlson. Mid-Latitude Weather Systems. American Meteorological Society, Boston, 1998. ISBN 1-878220-30-6.

Edmund K. M. Chang, Yanjuan Guo, and Xiaoming Xia. CMIP5 multimodel ensemble projection of storm track change under global warming. Journal of Geophysical Research: Atmospheres, 117(D23), 2012. ISSN 2156-2202. doi: 10.1029/2012JD018578. URL https://agupubs.onlinelibrary.wiley.com/doi/abs/10.1029/2012JD018578.

Jason Cordeira. Mid-Latitude Dynamics and Atmospheric Rivers; conference presentation available at: http://cw3e.ucsd.edu/. 2016. URL http://cw3e.ucsd.edu.

Jason M. Cordeira, F. Martin Ralph, and Benjamin J. Moore. The Development and Evolution of Two Atmospheric Rivers in Proximity to Western North Pacific Tropical Cyclones in October 2010. Monthly Weather Review, 141(12):4234–4255, 2013. doi: 10.1175/MWR-D-13-00019.1. URL http://journals.ametsoc.org/doi/abs/10.1175/MWR-D-13-00019.1.

H. F. Dacre, P. A. Clark, O. Martinez-Alvarado, M. A. Stringer, and D. A. Lavers. How Do Atmospheric Rivers Form? Bulletin of the American Meteorological Society, 96(8):1243–1255, 2015. ISSN 0003-0007. doi: 10.1175/BAMS-D-14-00031.1. URL https://journals.ametsoc.org/doi/full/10.1175/BAMS-D-14-00031.1.

Nicholas Davis and Thomas Birner. Seasonal to multidecadal variability of the width of the tropical belt. Journal of Geophysical Research: Atmospheres, 118(14):7773–7787, 2013. ISSN 2169-8996. doi: 10.1002/jgrd.50610. URL https://agupubs.onlinelibrary.wiley.com/doi/abs/10.1002/jgrd.50610.

Nicholas Davis and Thomas Birner. Climate Model Biases in the Width of the Tropical Belt. Journal of Climate, 29(5):1935–1954, March 2016. ISSN 0894-8755. doi: 10.1175/JCLI-D-15-0336.1. URL https://journals.ametsoc.org/jcli/article/29/5/1935/35098/Climate-Model-Biases-in-the-Width-of-the-Tropical.

Michael J. DeFlorio, Duane E. Waliser, Bin Guan, David A. Lavers, F. Martin Ralph, and Frédéric Vitart. Global Assessment of Atmospheric River Prediction Skill. Journal of Hydrometeorology, 19(2):409–426, February 2018. ISSN 1525-755X. doi: 10.1175/JHM-D-17-0135.1. URL https://journals.ametsoc.org/jhm/article/19/2/409/69586/Global-Assessment-of-Atmospheric-River-Prediction.

Michael Dettinger. Climate Change, Atmospheric Rivers, and Floods in California – A Multimodel Analysis of Storm Frequency and Magnitude Changes. Journal of the American Water Resources Association (JAWRA), 47(3):514–523, 2011. doi:

10.1111/j.1752-1688.2011.00546.x. URL https://ca.water.usgs.gov/pubs/2011/climate-change-atmospheric-rivers-floods-california-dettinger.pdf.

Michael Dettinger, F. Ralph, and David Lavers. Setting the Stage for a Global Science of Atmospheric Rivers. Eos, 96, 2015. ISSN 2324-9250. doi: 10.1029/2015EO038675. URL https://eos.org/meeting-reports/setting-the-stage-for-a-global-science-of-atmospheric-rivers.

Michael D. Dettinger, Fred Martin Ralph, Tapash Das, Paul J. Neiman, and Daniel R. Cayan. Atmospheric Rivers, Floods and the Water Resources of California. Water, 3 (2):445–478, 2011. ISSN 2073-4441. doi: 10.3390/w3020445. URL http://www.mdpi.com/2073-4441/3/2/445. Publisher: Molecular Diversity Preservation International.

Claude E. Duchon. Lanczos Filtering in One and Two Dimensions. Journal of Applied Meteorology, 18(8):1016–1022, August 1979. ISSN 0021-8952. doi: 10.1175/1520-0450(1979)018⟨1016:LFIOAT⟩2.0.CO;2. URL https://journals.ametsoc.org/doi/abs/10.1175/1520-0450%281979%29018%3C1016%3ALFIOAT%3E2.0.CO%3B2.

Jorge Eiras-Barca, Alexandre M Ramos, Joaquim G Pinto, Ricardo M Trigo, Margarida L R Liberato, and Gonzalo Miguez-Macho. The concurrence of atmospheric rivers and explosive cyclogenesis in the North Atlantic and North Pacific basins. Earth Syst. Dynam, 9:91–102, 2018. doi: 10.5194/esd-9-91-2018. URL https://doi.org/10.5194/esd-9-91-2018.

J. Elsner and A.B. Kara. Hurricanes of the North Atlantic: Climate and Society. Oxford University Press, 1999. URL https://rmets.onlinelibrary.wiley.com/doi/abs/10.1002/joc.662.

Vicky Espinoza, Duane E. Waliser, Bin Guan, David A. Lavers, and F. Martin Ralph. Global Analysis of Climate Change Projection Effects on Atmospheric Rivers. Geophysical Research Letters, 45(9):4299–4308, 2018. ISSN 1944-8007. doi: 10.1029/2017GL076968. URL https://agupubs.onlinelibrary.wiley.com/doi/abs/10.1029/2017GL076968.

Dargan M. W. Frierson, Jian Lu, and Gang Chen. Width of the Hadley cell in simple and comprehensive general circulation models. Geophysical Research Letters, 34 (18), September 2007. ISSN 0094-8276. doi: 10.1029/2007GL031115. URL https://agupubs.onlinelibrary.wiley.com/doi/full/10.1029/2007GL031115.

T. Theodore Fujita. Tornadoes and Downbursts in the Context of Generalized Planetary Scales. Journal of the Atmospheric Sciences, 38(8):1511–1534, August 1981. ISSN 0022-4928, 1520-0469. doi: 10.1175/1520-0469(1981)038⟨1511:TADITC⟩2.0.CO;2. URL https://journals.ametsoc.org/view/journals/atsc/38/8/1520-0469_1981_038_1511_taditc_2_0_co_2.xml. Publisher: American Meteorological Society Section: Journal of the Atmospheric Sciences.

Yang Gao, Jian Lu, L. Ruby Leung, Qing Yang, Samson Hagos, and Yun Qian. Dynamical and thermodynamical modulations on future changes of landfalling atmospheric rivers over western North America. Geophysical Research Letters, 42(17):7179–7186, 2015. ISSN 00948276. doi: 10.1002/2015GL065435. URL http://doi.wiley.com/10.1002/2015GL065435. Publisher: Wiley-Blackwell.

Yang Gao, Jian Lu, and L. Ruby Leung. Uncertainties in Projecting Future Changes in Atmospheric Rivers and Their Impacts on Heavy Precipitation over Europe. Journal of Climate, 29(18):6711–6726, June 2016. ISSN 0894-8755. doi: 10.1175/JCLI-D-16-0088.1. URL https://journals.ametsoc.org/doi/10.1175/JCLI-D-16-0088.1.

Ronald Gelaro, Will McCarty, Max J. Suárez, Ricardo Todling, Andrea Molod, Lawrence Takacs, Cynthia A. Randles, Anton Darmenov, Michael G. Bosilovich, Rolf Reichle, Krzysztof Wargan, Lawrence Coy, Richard Cullather, Clara Draper, Santha Akella, Virginie Buchard, Austin Conaty, Arlindo M. da Silva, Wei Gu, Gi-Kong Kim, Randal Koster, Robert Lucchesi, Dagmar Merkova, Jon Eric Nielsen, Gary Partyka, Steven Pawson, William Putman, Michele Rienecker, Siegfried D. Schubert, Meta Sienkiewicz, Bin Zhao, Ronald Gelaro, Will McCarty, Max J. Suárez, Ricardo Todling, Andrea Molod, Lawrence Takacs, Cynthia A. Randles, Anton Darmenov, Michael G. Bosilovich, Rolf Reichle, Krzysztof Wargan, Lawrence Coy, Richard Cullather, Clara Draper,

Santha Akella, Virginie Buchard, Austin Conaty, Arlindo M. da Silva, Wei Gu, Gi-Kong Kim, Randal Koster, Robert Lucchesi, Dagmar Merkova, Jon Eric Nielsen, Gary Partyka, Steven Pawson, William Putman, Michele Rienecker, Siegfried D. Schubert, Meta Sienkiewicz, and Bin Zhao. The Modern-Era Retrospective Analysis for Research and Applications, Version 2 (MERRA-2). Journal of Climate, 30(14):5419–5454, 2017. ISSN 0894-8755. doi: 10.1175/JCLI-D-16-0758.1. URL http://journals.ametsoc.org/doi/10.1175/JCLI-D-16-0758.1.

Alexander Gershunov, Tamara Shulgina, F. Martin Ralph, David A. Lavers, and Jonathan J. Rutz. Assessing the climate-scale variability of atmospheric rivers affecting western North America: Atmospheric River Climate-Scale Behavior. Geophysical Research Letters, 44(15):7900–7908, August 2017. ISSN 00948276. doi: 10.1002/2017GL074175. URL http://doi.wiley.com/10.1002/2017GL074175.

N. Goldenson, L. R. Leung, C. M. Bitz, and E. Blanchard-Wrigglesworth. Influence of Atmospheric Rivers on Mountain Snowpack in the Western United States. Journal of Climate, 31(24):9921–9940, December 2018. ISSN 0894-8755, 1520-0442. doi: 10.1175/JCLI-D-18-0268.1. URL https://journals.ametsoc.org/doi/10.1175/JCLI-D-18-0268.1.

Bin Guan and Duane E. Waliser. Detection of atmospheric rivers: Evaluation and application of an algorithm for global studies: Detection of Atmospheric Rivers. Journal of Geophysical Research: Atmospheres, 120(24):12514–12535, December 2015. ISSN 2169897X. doi: 10.1002/2015JD024257. URL http://doi.wiley.com/10.1002/2015JD024257.

Bin Guan and Duane E. Waliser. Tracking Atmospheric Rivers Globally: Spatial Distributions and Temporal Evolution of Life Cycle Characteristics. Journal of Geophysical Research: Atmospheres, 124(23):12523–12552, 2019. ISSN 2169-8996. doi: 10.1029/2019JD031205. URL https://agupubs.onlinelibrary.wiley.com/doi/abs/10.1029/2019JD031205.

Bin Guan, Noah P. Molotch, Duane E. Waliser, Eric J. Fetzer, and Paul J. Neiman. Extreme snowfall events linked to atmospheric rivers and surface air temperature via satellite measurements. Geophysical Research Letters, 37(20), 2010. ISSN 1944-8007. doi: 10.1029/2010GL044696. URL https://agupubs.onlinelibrary.wiley.com/doi/abs/10.1029/2010GL044696.

Bin Guan, Duane E. Waliser, and F. Martin Ralph. An Intercomparison between Reanalysis and Dropsonde Observations of the Total Water Vapor Transport in Individual Atmospheric Rivers. Journal of Hydrometeorology, 19(2):321–337, February 2018. ISSN 1525-755X, 1525-7541. doi: 10.1175/JHM-D-17-0114.1. URL http://journals.ametsoc.org/doi/10.1175/JHM-D-17-0114.1.

Samson Hagos, L. Ruby Leung, Qing Yang, Chun Zhao, and Jian Lu. Resolution and Dynamical Core Dependence of Atmospheric River Frequency in Global Model Simulations. Journal of Climate, 28(7):2764–2776, April 2015. ISSN 0894-8755, 1520-0442. doi: 10.1175/JCLI-D-14-00567.1. URL http://journals.ametsoc.org/doi/10.1175/JCLI-D-14-00567.1.

Samson M. Hagos, L. Ruby Leung, Jin-Ho Yoon, Jian Lu, and Yang Gao. A projection of changes in landfalling atmospheric river frequency and extreme precipitation over western North America from the Large Ensemble CESM simulations. Geophysical Research Letters, 43(3):1357–1363, 2016. ISSN 1944-8007. doi: 10.1002/2015GL067392. URL https://agupubs.onlinelibrary.wiley.com/doi/abs/10.1002/2015GL067392.

Isaac M. Held. The Gap between Simulation and Understanding in Climate Modeling. Bulletin of the American Meteorological Society, 86(11):1609–1614, 2005. doi: 10.1175/BAMS-86-11-1609. URL http://journals.ametsoc.org/doi/10.1175/BAMS-86-11-1609. Publisher: American Meteorological Society.

Isaac M. Held and Brian J. Soden. Robust Responses of the Hydrological Cycle to Global Warming. Journal of Climate, 19(21):5686–5699, 2006. doi: 10.1175/JCLI3990.1. URL http://journals.ametsoc.org/doi/abs/10.1175/JCLI3990.1.

Hye-Mi Kim, Yang Zhou, and Michael A. Alexander. Changes in atmospheric rivers and moisture transport over the Northeast Pacific and western North America in response to ENSO diversity. Climate Dynamics, 52(12):7375–7388, June 2019. ISSN 1432-0894. doi: 10.1007/s00382-017-3598-9. URL https://doi.org/10.1007/s00382-017-3598-9.

Peter Knippertz, Heini Wernli, Peter Knippertz, and Heini Wernli. A Lagrangian Climatology of Tropical Moisture Exports to the Northern Hemispheric Extratropics. Journal of Climate, 23(4):987–1003, 2010. ISSN 0894-8755. doi: 10.1175/2009JCLI3333.1. URL http://journals.ametsoc.org/doi/abs/10.1175/2009JCLI3333.1.

Peter L. Langen, Rune Grand Graversen, and Thorsten Mauritsen. Separation of Contributions from Radiative Feedbacks to Polar Amplification on an Aquaplanet. Journal of Climate, 25(8):3010–3024, April 2012. ISSN 0894-8755. doi: 10.1175/JCLI-D-11-00246.1. URL https://journals.ametsoc.org/jcli/article/25/8/3010/106976/Separation-of-Contributions-from-Radiative.

David A. Lavers and Gabriele Villarini. The contribution of atmospheric rivers to precipitation in Europe and the United States. Journal of Hydrology, 522:382–390, March 2015. ISSN 0022-1694. doi: 10.1016/j.jhydrol.2014.12.010. URL http://www.sciencedirect.com/science/article/pii/S0022169414010208.

David A. Lavers, Gabriele Villarini, Richard P. Allan, Eric F. Wood, and Andrew J. Wade. The detection of atmospheric rivers in atmospheric reanalyses and their links to British winter floods and the large-scale climatic circulation: ARS AND BRITISH WINTER FLOODS. Journal of Geophysical Research: Atmospheres, 117(D20), October 2012. ISSN 01480227. doi: 10.1029/2012JD018027. URL http://doi.wiley.com/10.1029/2012JD018027.

David A. Lavers, Richard P. Allan, Gabriele Villarini, Benjamin Lloyd-Hughes, David J. Brayshaw, and Andrew J. Wade. Future changes in atmospheric rivers and their implications for winter flooding in Britain. Environmental Research Letters, 8(3):

034010, July 2013. ISSN 1748-9326. doi: 10.1088/1748-9326/8/3/034010. URL https://doi.org/10.1088%2F1748-9326%2F8%2F3%2F034010.

L. Ruby Leung and Yun Qian. Atmospheric rivers induced heavy precipitation and flooding in the western U.S. simulated by the WRF regional climate model: ATMOSPHERIC RIVER, PRECIPITATION, FLOOD. Geophysical Research Letters, 36(3):n/a–n/a, February 2009. ISSN 00948276. doi: 10.1029/2008GL036445. URL http://doi.wiley.com/10.1029/2008GL036445.

Jian Lu, Gabriel A. Vecchi, and Thomas Reichler. Expansion of the Hadley cell under global warming. Geophysical Research Letters, 34(6), 2007. ISSN 1944-8007. doi: 10.1029/2006GL028443. URL https://agupubs.onlinelibrary.wiley.com/doi/abs/10.1029/2006GL028443.

Penelope Maher, Michael E. Kelleher, Philip G. Sansom, and John Methven. Is the subtropical jet shifting poleward? Climate Dynamics, 54(3):1741–1759, February 2020. ISSN 1432-0894. doi: 10.1007/s00382-019-05084-6. URL https://doi.org/10.1007/s00382-019-05084-6.

Andrew C. Martin, F. Martin Ralph, Anna Wilson, Laurel DeHaan, and Brian Kawzenuk. Rapid Cyclogenesis from a Mesoscale Frontal Wave on an Atmospheric River: Impacts on Forecast Skill and Predictability during Atmospheric River Landfall. Journal of Hydrometeorology, 20(9):1779–1794, September 2019. ISSN 1525-755X. doi: 10.1175/JHM-D-18-0239.1. URL https://journals.ametsoc.org/jhm/article/20/9/1779/344247/Rapid-Cyclogenesis-from-a-Mesoscale-Frontal-Wave.

Elizabeth E. McClenny, Paul A. Ullrich, and Richard Grotjahn. Sensitivity of Atmospheric River Vapor Transport and Precipitation to Uniform Sea Surface Temperature Increases. Journal of Geophysical Research: Atmospheres, 125(21), November 2020. ISSN 2169-897X, 2169-8996. doi: 10.1029/2020JD033421. URL https://onlinelibrary.wiley.com/doi/10.1029/2020JD033421.

Ruth E. McDonald. Understanding the impact of climate change on Northern Hemisphere extra-tropical cyclones. Climate Dynamics, 37(7):1399–1425, October 2011. ISSN 1432-0894. doi: 10.1007/s00382-010-0916-x. URL https://doi.org/10.1007/s00382-010-0916-x.

Brian Medeiros, David L. Williamson, and Jerry G. Olson. Reference aquaplanet climate in the Community Atmosphere Model, Version 5. Journal of Advances in Modeling Earth Systems, 8(1):406–424, 2016. ISSN 19422466. doi: 10.1002/2015MS000593. URL http://doi.wiley.com/10.1002/2015MS000593. Publisher: John Wiley & Sons, Ltd.

Benjamin J. Moore, Paul J. Neiman, F. Martin Ralph, and Faye E. Barthold. Physical Processes Associated with Heavy Flooding Rainfall in Nashville, Tennessee, and Vicinity during 1–2 May 2010: The Role of an Atmospheric River and Mesoscale Convective Systems. Monthly Weather Review, 140(2):358–378, February 2012. ISSN 1520-0493, 0027-0644. doi: 10.1175/MWR-D-11-00126.1. URL https://journals.ametsoc.org/view/journals/mwre/140/2/mwr-d-11-00126.1.xml. Publisher: American Meteorological Society Section: Monthly Weather Review.

Bryan D. Mundhenk, Elizabeth A. Barnes, and Eric D. Maloney. All-Season Climatology and Variability of Atmospheric River Frequencies over the North Pacific. Journal of Climate, 29(13):4885–4903, July 2016. ISSN 0894-8755, 1520-0442. doi: 10.1175/JCLI-D-15-0655.1. URL http://journals.ametsoc.org/doi/10.1175/JCLI-D-15-0655.1.

Grzegorz Muszynski, Karthik Kashinath, Vitaliy Kurlin, Michael Wehner, and Prabhat. Topological data analysis and machine learning for recognizing atmospheric river patterns in large climate datasets. Geoscientific Model Development, 12(2):613–628, February 2019. ISSN 1991-9603. doi: 10.5194/gmd-12-613-2019. URL https://gmd.copernicus.org/articles/12/613/2019/.

R. B. Neale and B. J. Hoskins. A standard test for AGCMs including their physical parametrizations: I: the proposal. Atmospheric Science Letters, 1(2):101–107, 2000.

ISSN 1530-261X. doi: 10.1006/asle.2000.0022. URL https://rmets.onlinelibrary.wiley.com/doi/abs/10.1006/asle.2000.0022.

Richard B Neale, Andrew Gettelman, Sungsu Park, Chih-Chieh Chen, Peter H Lauritzen, David L Williamson, Andrew J Conley, Doug Kinnison, Dan Marsh, Anne K Smith, Francis Vitt, Rolando Garcia, Jean-Francois Lamarque, Mike Mills, Simone Tilmes, Hugh Morrison, Philip Cameron-Smith, William D Collins, Michael J Iacono, Richard C Easter, Xiaohong Liu, Steven J Ghan, Philip J Rasch, and Mark A Taylor. Description of the NCAR Community Atmosphere Model (CAM 5.0). Tech. Rep. TN-486+STR, Natl. Cent. for Atmos. Res., Boulder, Colo., page 289, 2010.

Paul J. Neiman, F. Martin Ralph, A. B. White, D. E. Kingsmill, and P. O. G. Persson. The Statistical Relationship between Upslope Flow and Rainfall in California's Coastal Mountains: Observations during CALJET. Monthly Weather Review, 130(6):1468–1492, 2002. doi: 10.1175/1520-0493(2002)130⟨1468:TSRBUF⟩2.0.CO;2. URL http://journals.ametsoc.org/doi/abs/10.1175/1520-0493%282002%29130%3C1468%3ATSRBUF%3E2.0.CO%3B2.

Paul J. Neiman, F. Martin Ralph, Gary A. Wick, Jessica D. Lundquist, and Michael D. Dettinger. Meteorological Characteristics and Overland Precipitation Impacts of Atmospheric Rivers Affecting the West Coast of North America Based on Eight Years of SSM/I Satellite Observations. Journal of Hydrometeorology, 9(1):22–47, February 2008. ISSN 1525-7541, 1525-755X. doi: 10.1175/2007JHM855.1. URL https://journals.ametsoc.org/view/journals/hydr/9/1/2007jhm855_1.xml. Publisher: American Meteorological Society Section: Journal of Hydrometeorology.

Paul J. Neiman, Benjamin J. Moore, Allen B. White, Gary A. Wick, Joshua Aikins, Darren L. Jackson, J. Ryan Spackman, and F. Martin Ralph. An Airborne and Ground-Based Study of a Long-Lived and Intense Atmospheric River with Mesoscale Frontal Waves Impacting California during CalWater-2014. Monthly Weather Review, 144(3):1115–1144, March 2016. ISSN 0027-0644. doi: 10.

1175/MWR-D-15-0319.1. URL https://journals.ametsoc.org/mwr/article/144/3/1115/72334/An-Airborne-and-Ground-Based-Study-of-a-Long-Lived.

Reginald E. Newell, Nicholas E. Newell, Yong Zhu, and Courtney Scott. Tropospheric rivers? – A pilot study. Geophysical Research Letters, 19(24):2401–2404, 1992. ISSN 1944-8007. doi: https://doi.org/10.1029/92GL02916. URL https://agupubs.onlinelibrary.wiley.com/doi/abs/10.1029/92GL02916.

Travis Allen O'Brien, Michael F. Wehner, Ashley E. Payne, Christine A. Shields, Jonathan J. Rutz, L. Ruby Leung, F. Martin Ralph, Allison B. Marquardt Collow, Bin Guan, Juan Manuel Lora, Elizabeth McClenny, Kyle M. Nardi, Alexandre M. Ramos, Ricardo Tomé, Chandan Sarangi, Eric Jay Shearer, Paul Ullrich, Colin M. Zarzycki, Burlen Loring, Huanping Huang, Héctor Alejandro Inda Díaz, Alan M. Rhoades, and Yang Zhou. Increases in Future AR Count and Size: Overview of the ARTMIP Tier 2 CMIP5/6 Experiment, April 2020. URL http://www.essoar.org/doi/10.1002/essoar.10504170.1. Archive Location: world Publisher: Earth and Space Science Open Archive Section: Climatology (Global Change).

P A O'Gorman and C J Muller. How closely do changes in surface and column water vapor follow Clausius–Clapeyron scaling in climate change simulations? Environmental Research Letters, 5(2):025207, April 2010. ISSN 1748-9326. doi: 10.1088/1748-9326/5/2/025207. URL http://stacks.iop.org/1748-9326/5/i=2/a=025207?key=crossref.e3222bcec4394fc1626baf06b07920c3.

Paul A. O'Gorman. Precipitation Extremes Under Climate Change. Current Climate Change Reports, 1(2):49–59, June 2015. ISSN 2198-6061. doi: 10.1007/s40641-015-0009-3. URL https://doi.org/10.1007/s40641-015-0009-3.

Paul A. O'Gorman and Tapio Schneider. The physical basis for increases in precipitation extremes in simulations of 21st-century climate change. Proceedings of the National Academy of Sciences, 106(35):14773–14777, September 2009a. ISSN 0027-8424, 1091-

6490. doi: 10.1073/pnas.0907610106. URL https://www.pnas.org/content/106/35/14773.

Paul A. O'Gorman and Tapio Schneider. Scaling of Precipitation Extremes over a Wide Range of Climates Simulated with an Idealized GCM. Journal of Climate, 22(21): 5676–5685, 2009b. doi: 10.1175/2009JCLI2701.1. URL http://journals.ametsoc.org/doi/abs/10.1175/2009JCLI2701.1.

Paul A. O'Gorman and Martin S. Singh. Vertical structure of warming consistent with an upward shift in the middle and upper troposphere. Geophysical Research Letters, 40 (9):1838–1842, 2013. ISSN 1944-8007. doi: 10.1002/grl.50328. URL https://agupubs.onlinelibrary.wiley.com/doi/abs/10.1002/grl.50328.

Paul A. O'Gorman, Richard P. Allan, Michael P. Byrne, and Michael Previdi. Energetic Constraints on Precipitation Under Climate Change. Surveys in Geophysics, 33(3): 585–608, July 2012. ISSN 1573-0956. doi: 10.1007/s10712-011-9159-6. URL https://doi.org/10.1007/s10712-011-9159-6.

Travis A. O'Brien, Ashley E. Payne, Christine A. Shields, Jonathan Rutz, Swen Brands, Christopher Castellano, Jiayi Chen, William Cleveland, Michael J. DeFlorio, Naomi Goldenson, Irina V. Gorodetskaya, Héctor Inda Díaz, Karthik Kashinath, Brian Kawzenuk, Sol Kim, Mikhail Krinitskiy, Juan M. Lora, Beth McClenny, Allison Michaelis, John P. O'Brien, Christina M. Patricola, Alexandre M. Ramos, Eric J. Shearer, Wen-Wen Tung, Paul A. Ullrich, Michael F. Wehner, Kevin Yang, Rudong Zhang, Zhenhai Zhang, and Yang Zhou. Detection Uncertainty Matters for Understanding Atmospheric Rivers. Bulletin of the American Meteorological Society, 101(6):E790–E796, 2020. ISSN 0003-0007. doi: 10.1175/BAMS-D-19-0348.1. URL https://journals.ametsoc.org/bams/article/doi/10.1175/BAMS-D-19-0348.1/345615/Detection-Uncertainty-Matters-for-Understanding.

Homero Paltan, Duane Waliser, Wee Ho Lim, Bin Guan, Dai Yamazaki, Raghav Pant, and Simon Dadson. Global Floods and Water Availability Driven by Atmospheric

Rivers. Geophysical Research Letters, 44(20):387–10, 2017. ISSN 00948276. doi: 10.1002/2017GL074882. URL http://doi.wiley.com/10.1002/2017GL074882. Publisher: Wiley-Blackwell.

Ashley E. Payne and Gudrun Magnusdottir. An evaluation of atmospheric rivers over the North Pacific in CMIP5 and their response to warming under RCP 8.5: NORTH PACIFIC ATMOSPHERIC RIVERS IN CMIP5. Journal of Geophysical Research: Atmospheres, 120(21):11,173–11,190, November 2015. ISSN 2169897X. doi: 10.1002/2015JD023586. URL http://doi.wiley.com/10.1002/2015JD023586.

Ashley E. Payne, Marie-Estelle Demory, L. Ruby Leung, Alexandre M. Ramos, Christine A. Shields, Jonathan J. Rutz, Nicholas Siler, Gabriele Villarini, Alex Hall, and F. Martin Ralph. Responses and impacts of atmospheric rivers to climate change. Nature Reviews Earth & Environment, 1(3):143–157, March 2020. ISSN 2662-138X. doi: 10.1038/s43017-020-0030-5. URL https://www.nature.com/articles/s43017-020-0030-5.

F. M. Ralph, T. Coleman, P. J. Neiman, R. J. Zamora, M. D. Dettinger, F. M. Ralph, T. Coleman, P. J. Neiman, R. J. Zamora, and M. D. Dettinger. Observed Impacts of Duration and Seasonality of Atmospheric-River Landfalls on Soil Moisture and Runoff in Coastal Northern California. Journal of Hydrometeorology, 14(2):443–459, 2013. ISSN 1525-755X. doi: 10.1175/JHM-D-12-076.1. URL http://journals.ametsoc.org/doi/abs/10.1175/JHM-D-12-076.1.

F. M. Ralph, S. F. Iacobellis, P. J. Neiman, J. M. Cordeira, J. R. Spackman, D. E. Waliser, G. A. Wick, A. B. White, and C. Fairall. Dropsonde Observations of Total Integrated Water Vapor Transport within North Pacific Atmospheric Rivers. Journal of Hydrometeorology, 18(9):2577–2596, 2017. doi: 10.1175/JHM-D-17-0036.1. URL http://journals.ametsoc.org/doi/10.1175/JHM-D-17-0036.1.

F. Martin Ralph, Paul J. Neiman, and Gary A. Wick. Satellite and CALJET Aircraft Observations of Atmospheric Rivers over the Eastern North Pacific

Ocean during the Winter of 1997/98. Monthly Weather Review, 132(7):1721–1745, 2004a. ISSN 0027-0644. doi: 10.1175/1520-0493(2004)132⟨1721:SACAOO⟩2.0.CO;2. URL http://journals.ametsoc.org/doi/abs/10.1175/1520-0493%282004%29132%3C1721%3ASACAOO%3E2.0.CO%3B2.

F. Martin Ralph, Paul J. Neiman, and Gary A. Wick. Satellite and CALJET Aircraft Observations of Atmospheric Rivers over the Eastern North Pacific Ocean during the Winter of 1997/98. Monthly Weather Review, 132(7):1721–1745, 2004b. doi: 10.1175/1520-0493(2004)132⟨1721:SACAOO⟩2.0.CO;2. URL http://journals.ametsoc.org/doi/abs/10.1175/1520-0493%282004%29132%3C1721%3ASACAOO%3E2.0.CO%3B2.

F. Martin Ralph, Paul J. Neiman, and Richard Rotunno. Dropsonde Observations in Low-Level Jets over the Northeastern Pacific Ocean from CALJET-1998 and PACJET-2001: Mean Vertical-Profile and Atmospheric-River Characteristics. Monthly Weather Review, 133(4):889–910, 2005. ISSN 0027-0644. doi: 10.1175/MWR2896.1. URL http://journals.ametsoc.org/doi/abs/10.1175/MWR2896.1.

F. Martin Ralph, Paul J. Neiman, Gary A. Wick, Seth I. Gutman, Michael D. Dettinger, Daniel R. Cayan, and Allen B. White. Flooding on California's Russian River: Role of atmospheric rivers. Geophysical Research Letters, 33(13):L13801, 2006. ISSN 0094-8276. doi: 10.1029/2006GL026689. URL http://doi.wiley.com/10.1029/2006GL026689.

F. Martin Ralph, Michael D. Dettinger, Mary M. Cairns, Thomas J. Galarneau, and John Eylander. Defining "Atmospheric River": How the Glossary of Meteorology Helped Resolve a Debate. Bulletin of the American Meteorological Society, 99(4):837–839, April 2018. ISSN 0003-0007. doi: 10.1175/BAMS-D-17-0157.1. URL https://journals.ametsoc.org/bams/article/99/4/837/70295/Defining-Atmospheric-River-How-the-Glossary-of.

F. Martin Ralph, Jonathan J. Rutz, Jason M. Cordeira, Michael Dettinger, Michael Anderson, David Reynolds, Lawrence J. Schick, and Chris Smallcomb. A Scale

to Characterize the Strength and Impacts of Atmospheric Rivers. Bulletin of the American Meteorological Society, 100(2):269–289, February 2019. ISSN 0003-0007. doi: 10.1175/BAMS-D-18-0023.1. URL https://journals.ametsoc.org/doi/10.1175/BAMS-D-18-0023.1.

F. Martin Ralph, Michael D. Dettinger, Jonathan J. Rutz, and Duane E. Waliser, editors. Atmospheric Rivers. Springer International Publishing, 1 edition, 2020. ISBN 978-3-030-28906-5. URL https://www.springer.com/gp/book/9783030289058.

Alexandre M. Ramos, Raquel Nieto, Ricardo Tomé, Luis Gimeno, Ricardo M. Trigo, Margarida L. R. Liberato, and David A. Lavers. Atmospheric rivers moisture sources from a Lagrangian perspective. Earth System Dynamics, 7(2):371–384, April 2016. ISSN 2190-4987. doi: 10.5194/esd-7-371-2016. URL https://esd.copernicus.org/articles/7/371/2016/.

Gerard H. Roe, Nicole Feldl, Kyle C. Armour, Yen-Ting Hwang, and Dargan M. W. Frierson. The remote impacts of climate feedbacks on regional climate predictability. Nature Geoscience, 8(2):135–139, February 2015. ISSN 1752-0908. doi: 10.1038/ngeo2346. URL https://www.nature.com/articles/ngeo2346.

Jonathan J. Rutz, W. James Steenburgh, and F. Martin Ralph. Climatological Characteristics of Atmospheric Rivers and Their Inland Penetration over the Western United States. Monthly Weather Review, 142(2):905–921, October 2013. ISSN 0027-0644. doi: 10.1175/MWR-D-13-00168.1. URL https://journals.ametsoc.org/doi/abs/10.1175/MWR-D-13-00168.1.

Jonathan J. Rutz, W. James Steenburgh, and F. Martin Ralph. Climatological Characteristics of Atmospheric Rivers and Their Inland Penetration over the Western United States. Monthly Weather Review, 142(2):905–921, February 2014. ISSN 0027-0644, 1520-0493. doi: 10.1175/MWR-D-13-00168.1. URL http://journals.ametsoc.org/doi/10.1175/MWR-D-13-00168.1.

Jonathan J. Rutz, Christine A. Shields, Juan M. Lora, Ashley E. Payne, Bin Guan,

Paul Ullrich, Travis O'Brien, L. Ruby Leung, F. Martin Ralph, Michael Wehner, Swen Brands, Allison Collow, Naomi Goldenson, Irina Gorodetskaya, Helen Griffith, Karthik Kashinath, Brian Kawzenuk, Harinarayan Krishnan, Vitaliy Kurlin, David Lavers, Gudrun Magnusdottir, Kelly Mahoney, Elizabeth McClenny, Grzegorz Muszynski, Phu Dinh Nguyen, Mr Prabhat, Yun Qian, Alexandre M. Ramos, Chandan Sarangi, Scott Sellars, T. Shulgina, Ricardo Tome, Duane Waliser, Daniel Walton, Gary Wick, Anna M. Wilson, and Maximiliano Viale. The Atmospheric River Tracking Method Intercomparison Project (ARTMIP): Quantifying Uncertainties in Atmospheric River Climatology. Journal of Geophysical Research: Atmospheres, 124(24):13777–13802, 2019. ISSN 2169-8996. doi: 10.1029/2019JD030936. URL https://agupubs.onlinelibrary.wiley.com/doi/abs/10.1029/2019JD030936.

Frederick Sanders and John R. Gyakum. Synoptic-Dynamic Climatology of the "Bomb". Monthly Weather Review, 108(10):1589–1606, October 1980. ISSN 1520-0493, 0027-0644. doi: 10.1175/1520-0493(1980)108⟨1589:SDCOT⟩2.0.CO;2. URL https://journals.ametsoc.org/view/journals/mwre/108/10/1520-0493_1980_108_1589_sdcot_2_0_co_2.xml. Publisher: American Meteorological Society Section: Monthly Weather Review.

A. Saruwatari, K. Fukuhara, and Y. Watanabe. Probabilistic assessment of storm surge potential due to explosive cyclogenesis in the northwest Pacific region. Coastal Engineering Journal, 61(4):520–534, October 2019. ISSN 2166-4250. doi: 10.1080/21664250.2019.1651519. URL https://doi.org/10.1080/21664250.2019.1651519. Publisher: Taylor & Francis _eprint: https://doi.org/10.1080/21664250.2019.1651519.

T. A. Shaw and A. Voigt. Tug of war on summertime circulation between radiative forcing and sea surface warming. Nature Geoscience, 8(7):560–566, July 2015. ISSN 1752-0908. doi: 10.1038/ngeo2449. URL https://www.nature.com/articles/ngeo2449.

Tiffany A. Shaw, Aiko Voigt, Tiffany A. Shaw, and Aiko Voigt. Understanding the Links between Subtropical and Extratropical Circulation Responses to Climate Change Using Aquaplanet Model Simulations. Journal of Climate, 29(18):6637–6657, 2016. ISSN

0894-8755. doi: 10.1175/JCLI-D-16-0049.1. URL http://journals.ametsoc.org/doi/10.1175/JCLI-D-16-0049.1.

Christine A. Shields and Jeffrey T. Kiehl. Atmospheric river landfall-latitude changes in future climate simulations: FUTURE CHANGES TO AR LANDFALL LOCATION. Geophysical Research Letters, 43(16):8775–8782, August 2016. ISSN 00948276. doi: 10.1002/2016GL070470. URL http://doi.wiley.com/10.1002/2016GL070470.

Christine A. Shields, Jonathan J. Rutz, Lai-Yung Leung, F. Martin Ralph, Michael Wehner, Brian Kawzenuk, Juan M. Lora, Elizabeth McClenny, Tashiana Osborne, Ashley E. Payne, Paul Ullrich, Alexander Gershunov, Naomi Goldenson, Bin Guan, Yun Qian, Alexandre M. Ramos, Chandan Sarangi, Scott Sellars, Irina Gorodetskaya, Karthik Kashinath, Vitaliy Kurlin, Kelly Mahoney, Grzegorz Muszynski, Roger Pierce, Aneesh C. Subramanian, Ricardo Tome, Duane Waliser, Daniel Walton, Gary Wick, Anna Wilson, David Lavers, Allison Collow, Harinarayan Krishnan, Gudrun Magnusdottir, and Phu Nguyen. Atmospheric River Tracking Method Intercomparison Project (ARTMIP): project goals and experimental design. Geoscientific Model Development, 11(6):2455–2474, 2018. ISSN 1991-9603. doi: 10.5194/gmd-11-2455-2018. URL https://www.geosci-model-dev.net/11/2455/2018/.

Nicholas Siler and Gerard Roe. How will orographic precipitation respond to surface warming? An idealized thermodynamic perspective. Geophysical Research Letters, 41(7):2606–2613, April 2014. ISSN 0094-8276. doi: 10.1002/2013GL059095. URL https://agupubs.onlinelibrary.wiley.com/doi/full/10.1002/2013GL059095.

Harald Sodemann, Andreas Stohl, Harald Sodemann, and Andreas Stohl. Moisture Origin and Meridional Transport in Atmospheric Rivers and Their Association with Multiple Cyclones*. Monthly Weather Review, 141(8):2850–2868, 2013. ISSN 0027-0644. doi: 10.1175/MWR-D-12-00256.1. URL http://journals.ametsoc.org/doi/abs/10.1175/MWR-D-12-00256.1.

A. Stohl, C. Forster, and H. Sodemann. Remote sources of water vapor forming pre-

cipitation on the Norwegian west coast at 60$ˆ\circ$N-a tale of hurricanes and an atmospheric river. Journal of Geophysical Research: Atmospheres, 113(D5):n/a–n/a, 2008. ISSN 01480227. doi: 10.1029/2007JD009006. URL http://doi.wiley.com/10.1029/2007JD009006.

Erik T. Swenson, Jian Lu, and David M. Straus. Resolution Dependence and Rossby Wave Modulation of Atmospheric Rivers in an Aquaplanet Model. Journal of Geophysical Research: Atmospheres, 2018. ISSN 2169897X. doi: 10.1029/2017JD027899. URL http://doi.wiley.com/10.1029/2017JD027899. Publisher: Wiley-Blackwell.

Neil F. Tandon, Edwin P. Gerber, Adam H. Sobel, and Lorenzo M. Polvani. Understanding Hadley Cell Expansion versus Contraction: Insights from Simplified Models and Implications for Recent Observations. Journal of Climate, 26 (12):4304–4321, June 2013. ISSN 0894-8755. doi: 10.1175/JCLI-D-12-00598.1. URL https://journals.ametsoc.org/jcli/article/26/12/4304/34191/Understanding-Hadley-Cell-Expansion-versus.

Karl E. Taylor, Ronald J. Stouffer, and Gerald A. Meehl. An Overview of CMIP5 and the Experiment Design. Bulletin of the American Meteorological Society, 93(4):485–498, April 2012. ISSN 0003-0007. doi: 10.1175/BAMS-D-11-00094.1. URL https://journals.ametsoc.org/bams/article/93/4/485/60085/An-Overview-of-CMIP5-and-the-Experiment-Design.

Kevin E. Trenberth, Aiguo Dai, Roy M. Rasmussen, and David B. Parsons. The Changing Character of Precipitation. Bulletin of the American Meteorological Society, 84(9): 1205–1218, 2003. doi: 10.1175/BAMS-84-9-1205. URL http://journals.ametsoc.org/doi/10.1175/BAMS-84-9-1205. Publisher: American Meteorological Society.

P. A. Ullrich. Understanding the treatment of waves in atmospheric models. Part 1: The shortest resolved waves of the 1D linearized shallow-water equations. Quarterly Journal of the Royal Meteorological Society, 140(682):1426–1440, 2014. ISSN 1477-870X. doi: https://doi.org/10.1002/qj.2226. URL

https://rmets.onlinelibrary.wiley.com/doi/abs/10.1002/qj.2226. _eprint: https://rmets.onlinelibrary.wiley.com/doi/pdf/10.1002/qj.2226.

Paul A. Ullrich and Mark A. Taylor. Arbitrary-Order Conservative and Consistent Remapping and a Theory of Linear Maps: Part I. Monthly Weather Review, 143 (6):2419–2440, March 2015. ISSN 0027-0644. doi: 10.1175/MWR-D-14-00343.1. URL https://journals.ametsoc.org/doi/full/10.1175/MWR-D-14-00343.1.

Paul A. Ullrich and Colin M. Zarzycki. TempestExtremes: a framework for scale-insensitive pointwise feature tracking on unstructured grids. Geoscientific Model Development, 10(3):1069–1090, March 2017. ISSN 1991-9603. doi: 10.5194/gmd-10-1069-2017. URL https://gmd.copernicus.org/articles/10/1069/2017/.

Paul A. Ullrich, Dharshi Devendran, and Hans Johansen. Arbitrary-Order Conservative and Consistent Remapping and a Theory of Linear Maps: Part II. Monthly Weather Review, 144(4):1529–1549, January 2016. ISSN 0027-0644. doi: 10.1175/MWR-D-15-0301.1. URL https://journals.ametsoc.org/doi/10.1175/MWR-D-15-0301.1.

Paul A. Ullrich, Colin M. Zarzycki, Elizabeth E. McClenny, Marielle C. Pinheiro, Alyssa M. Stansfield, and Kevin A. Reed. TempestExtremes v2.1: A Community Framework for Feature Detection, Tracking and Analysis in Large Datasets. Geoscientific Model Development Discussions, pages 1–37, January 2021. ISSN 1991-959X. doi: https://doi.org/10.5194/gmd-2020-303. URL https://gmd.copernicus.org/preprints/gmd-2020-303/. Publisher: Copernicus GmbH.

Geoffrey K. Vallis, Pablo Zurita-Gotor, Cameron Cairns, and Joseph Kidston. Response of the large-scale structure of the atmosphere to global warming. Quarterly Journal of the Royal Meteorological Society, 141(690):1479–1501, 2015. ISSN 1477-870X. doi: 10.1002/qj.2456. URL https://rmets.onlinelibrary.wiley.com/doi/abs/10.1002/qj.2456.

Maximiliano Viale, Raúl Valenzuela, René D. Garreaud, and F. Martin Ralph. Impacts of Atmospheric Rivers on Precipitation in Southern South America. Journal of Hydrometeorology, 19(10):1671–1687, October 2018. ISSN 1525-755X, 1525-7541. doi: 10.1175/JHM-D-18-0006.1. URL http://journals.ametsoc.org/doi/10.1175/JHM-D-18-0006.1.

Pauli Virtanen, Ralf Gommers, Travis E. Oliphant, Matt Haberland, Tyler Reddy, David Cournapeau, Evgeni Burovski, Pearu Peterson, Warren Weckesser, Jonathan Bright, Stéfan J. van der Walt, Matthew Brett, Joshua Wilson, K. Jarrod Millman, Nikolay Mayorov, Andrew R. J. Nelson, Eric Jones, Robert Kern, Eric Larson, C. J. Carey, İlhan Polat, Yu Feng, Eric W. Moore, Jake VanderPlas, Denis Laxalde, Josef Perktold, Robert Cimrman, Ian Henriksen, E. A. Quintero, Charles R. Harris, Anne M. Archibald, Antônio H. Ribeiro, Fabian Pedregosa, and Paul van Mulbregt. SciPy 1.0: fundamental algorithms for scientific computing in Python. Nature Methods, 17(3):261–272, March 2020. ISSN 1548-7105. doi: 10.1038/s41592-019-0686-2. URL https://www.nature.com/articles/s41592-019-0686-2.

Stéfan van der Walt, Johannes L. Schönberger, Juan Nunez-Iglesias, François Boulogne, Joshua D. Warner, Neil Yager, Emmanuelle Gouillart, and Tony Yu. scikit-image: image processing in Python. PeerJ, 2:e453, June 2014. ISSN 2167-8359. doi: 10.7717/peerj.453. URL https://peerj.com/articles/453.

Michael D. Warner, Clifford F. Mass, and Eric P. Salathe. Changes in Winter Atmospheric Rivers along the North American West Coast in CMIP5 Climate Models. Journal of Hydrometeorology, 16(1):118–128, September 2014. ISSN 1525-755X. doi: 10.1175/JHM-D-14-0080.1. URL https://journals.ametsoc.org/doi/10.1175/JHM-D-14-0080.1.

Gary A. Wick, Paul J. Neiman, and F. Martin Ralph. Description and Validation of an Automated Objective Technique for Identification and Characterization of the Integrated Water Vapor Signature of Atmospheric Rivers. IEEE Transactions on Geoscience and

Remote Sensing, 51(4):2166–2176, April 2013a. ISSN 0196-2892, 1558-0644. doi: 10.1109/TGRS.2012.2211024. URL http://ieeexplore.ieee.org/document/6303904/.

Gary A. Wick, Paul J. Neiman, F. Martin Ralph, Thomas M. Hamill, Gary A. Wick, Paul J. Neiman, F. Martin Ralph, and Thomas M. Hamill. Evaluation of Forecasts of the Water Vapor Signature of Atmospheric Rivers in Operational Numerical Weather Prediction Models. Weather and Forecasting, 28(6):1337–1352, 2013b. ISSN 0882-8156. doi: 10.1175/WAF-D-13-00025.1. URL http://journals.ametsoc.org/doi/abs/10.1175/WAF-D-13-00025.1.

Tim Woollings, Abdel Hannachi, and Brian Hoskins. Variability of the North Atlantic eddy-driven jet stream. Quarterly Journal of the Royal Meteorological Society, 136 (649):856–868, 2010. ISSN 1477-870X. doi: 10.1002/qj.625. URL https://rmets.onlinelibrary.wiley.com/doi/abs/10.1002/qj.625.

Guangzhi Xu, Xiaohui Ma, Ping Chang, and Lin Wang. Image-processing-based atmospheric river tracking method version 1 (IPART-1). Geoscientific Model Development, 13(10):4639–4662, September 2020. ISSN 1991-9603. doi: 10.5194/gmd-13-4639-2020. URL https://gmd.copernicus.org/articles/13/4639/2020/.

Qing Yang, L. Ruby Leung, Sara A. Rauscher, Todd D. Ringler, and Mark A. Taylor. Atmospheric Moisture Budget and Spatial Resolution Dependence of Precipitation Extremes in Aquaplanet Simulations. Journal of Climate, 27(10):3565–3581, December 2013. ISSN 0894-8755. doi: 10.1175/JCLI-D-13-00468.1. URL https://journals.ametsoc.org/doi/10.1175/JCLI-D-13-00468.1.

Jeffrey H. Yin. A consistent poleward shift of the storm tracks in simulations of 21st century climate. Geophysical Research Letters, April 2017. ISSN 0094-8276. doi: 10.1029/2005GL023684@10.1002/(ISSN)1944-8007.ATMOSLINKAGES1. URL https://agupubs.onlinelibrary.wiley.com/doi/full/10.1029/2005GL023684%4010.1002/%28ISSN%291944-8007.ATMOSLINKAGES1.

Colin M. Zarzycki and Paul A. Ullrich. Assessing sensitivities in algorithmic detection of tropical cyclones in climate data. Geophysical Research Letters, 44(2):1141–1149, 2017. ISSN 1944-8007. doi: 10.1002/2016GL071606. URL https://agupubs.onlinelibrary.wiley.com/doi/abs/10.1002/2016GL071606.

Yong Zhu and Reginald E. Newell. A Proposed Algorithm for Moisture Fluxes from Atmospheric Rivers. Monthly Weather Review, 126(3):725–735, 1998. doi: 10.1175/1520-0493(1998)126⟨0725:APAFMF⟩2.0.CO;2. URL http://journals.ametsoc.org/doi/abs/10.1175/1520-0493%281998%29126%3C0725%3AAPAFMF%3E2.0.CO%3B2.